CHAPTER 6
Weights-of-Evidence Modeling of Sedimentary Rock-Hosted Au Deposits, P.R. China

By Chad S. Leonard, Mark J. Mihalasky, and Stephen G. Peters

Open-File Report: 02–131

2002

U.S. DEPARTMENT OF THE INTERIOR
U.S. GEOLOGICAL SURVEY

U.S. Geological Survey, Reno Field Office, Mackay School of Mines, MS-176,
University of Nevada, Reno, Nevada 89557-0047

CONTENTS

第6章　中国沉积岩型金矿床权重模型

查德S. 顿纳德　马克J. 米哈拉斯基　史蒂芬G. 彼得斯

目　录

List of Figures

List of tables

CHAPTER 6
Weights-of-Evidence Modeling of Sedimentary Rock-Hosted Au Deposits, P.R. China

By

Chad S. Leonard, Mark J. Mihalasky, and Stephen G. Peters

Abstract

Distribution of sedimentary rock-hosted Au deposits and occurrences was modeled for the Qinling and Dian-Qian-Gui areas of the P.R. China. Modeling was performed using the weights-of-evidence method, which is based on Bayesian probability, to produce resource favorability maps from various geoscientific data, primarily geology and structure. Maps of favorability revealed numerous regional-scale exploration targets in the two study areas where few, if any, known sedimentary rock-hosted Au deposits or occurrences exist. Modeling also indicated that the most important criterion for predicting sedimentary rock-hosted Au deposits and occurrences in both the Qinling and Dian-Qian-Gui areas, in order of importance, are geologic units, geologic unit-related factors (proximity to unit boundaries and lithodiversity), and structure-related factors (proximity to faults and topographic slope).

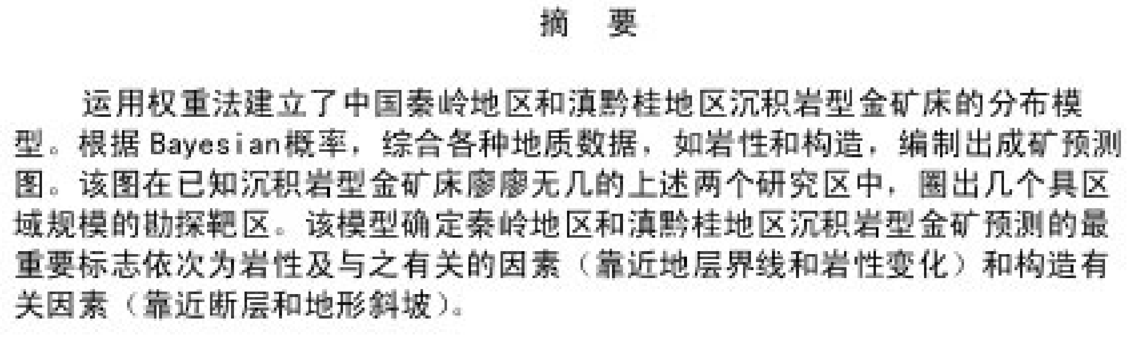

摘　要

运用权重法建立了中国秦岭地区和滇黔桂地区沉积岩型金矿床的分布模型。根据Bayesian概率，综合各种地质数据，如岩性和构造，编制出成矿预测图。该图在已知沉积岩型金矿床廖廖无几的上述两个研究区中，圈出几个具区域规模的勘探靶区。该模型确定秦岭地区和滇黔桂地区沉积岩型金矿预测的最重要标志依次为岩性及与之有关的因素（靠近地层界线和岩性变化）和构造有关因素（靠近断层和地形斜坡）。

INTRODUCTION

The People's Republic of China is one of the top-five Au producing countries in the world today. It produces nearly 180 tonnes of Au per year, of which 5 to 6 percent is extracted from sedimentary rock-hosted Au deposits (Zhou and others, 1999). Au reserves in these deposits are estimated to be at least 450 t, with substantial additional resources believed to exist in approximately 166 known deposits (Zhou and others, 1999). This makes the P.R. China second only to the U.S. in endowment of this deposit type. Li, Z.P. and Peters (1998) have shown that many of these deposits are true Carlin-type, but also include other genetic types hosted in sedimentary rock (see Chapter 1 for a detailed discussion). Interest in sedimentary rock-hosted Au (SRHG) deposits remains high due to their economic significance in the P.R. China and Nevada, USA.

Weights-of-evidence (WofE), a geographical information system (GIS)-based technique for modeling the distribution of mineral resources, was applied to two areas in the P.R. China to produce favorability maps for the occurrence of SRHG "mineral sites". For the purpose of WofE modeling, a mineral site is defined as a location belonging to any class SRHG deposit type, which includes occurrences, mineral deposits, and ore deposits (see Cox and others, 1986, p. 1).

The two study areas are the Qinling and Dian-Qian-Gui regions of north-central and south-central China (fig. 6-1). Both of these areas are located along the margins of the Precambrian Yangtze craton (see Chapters 2 and 3). The northern Qinling area in northwestrn Sichuan, and

Figure 6-1. Peoples Republic of China, showing the study areas of Qinling and Dian-Qian-Gui.

southern Gansu and southwestern Shaanxi Provinces is approximately 415,000 km^2 and contains about 68 known SRHG sites. The area is named from the Qinling fold belt in which it resides. The southern study area, Dian-Qian-Gui, also referred to as the Golden Triangle Region, is approximately 105,000 km^2 and contains about 61 SRHG sites. The area lies in southeastern Yunnan, southwestern Guizhou Provinces and northern Guangxi Autonomous Region (District).

The purpose of this study was to use WofE modeling to identify areas favorable for the occurrence of SRHG sites for the two study areas in the P.R. China. The objectives were: (1) examine and define the spatial associations between known SRHG sites and various geoscientific data; (2) produce resource favorability maps for SRHG sites on the basis of these spatial associations; and (3) interpret the favorability maps and suggest future targets for regional-scale exploration.

The WofE approach has been applied in previous studies and has shown positive results. Graeme F. Bonham-Carter, Fritz P. Agterberg and D. F. Wright have applied the method successfully to areas such as the Meguma terrane of Nova Scotia (see also, Bonham-Carter and others, 1988; Bonham-Carter and others, 1989; Agterberg and others, 1990). Studies conducted in the United States have focused on the Nevada Great Basin. Raines (1999) used the method to produce favorability maps for hot spring-related Au deposit-types. Mihalasky (1999), also working in the Great Basin, produced favorability maps for Au–Ag mineralization for both SRHG and epithermal deposit-types.

There has been little English language-published information of mineral resource analysis in the P.R. China of this kind. This study applies the WofE method to the Qinling and Dian-Qian-Gui areas in the P.R China and demonstrates that the method works well using only data extracted from regional-scale geologic maps. The study also employs some techniques not utilized in previous studies.

METALLOGENY and GEOLOGY

SRHG deposits, as described in Chapters 1 and 2, are found throughout the world in countries such as the USA, P.R. China, Australia, and Russia. They have been referred to in the literature as Carlin-type,

fine impregnation-type, invisible Au, sediment-hosted disseminated Au deposits, and sedimentary rock-hosted Au deposits. These deposits were first recognized as a unique type of deposit following the opening of the Carlin Mine in Nevada, USA in the early 1960s. Since their discovery and recognition as a separate class of deposits, there has been much debate as to their origin. This debate is fueled by a lack of supporting data to establish timing and type of ore-deposition system (Arehart, 1996). The following discussion of SRHG deposits is only a general overview, as the scope of this paper is modeling the distribution of these deposits, not their genesis. Information on SRHG deposits in China comes from studies conducted in the P.R. China, USA by authors Li, Z.P. and Peters (1998), and Wang and Zhang (1999).

General Characteristics of SRHG Deposits

SRHG deposits in the P.R. China and Nevada, USA typically are hosted in Paleozoic and Mesozoic sedimentary rocks. In the Qinling and Dian-Qian-Gui study areas, host ages are primarily Mid-Paleozoic to Mid-Mesozoic (Li, Z.P. and Peters, 1998) and rocks generally consist of mixed carbonates, calcareous siltstone and shale and siliciclastic rocks (Chapters 1 and 2). Minerals commonly associated with Au include pyrite, arsenical pyrite, arsenopyrite, realgar-orpiment, quartz, barite, and calcite. Au usually is disseminated as micron to sub-micron (<1–

mm-size) particles in, or with, As-rich pyrite. This extremely small size of Au particles has led some geologists to refer to it as “invisible Au.” Hydrothermal alteration associated with SRHG deposits includes decalcification, silicification, argillization, and decarbonatization, with the later being much less pronounced in Chinese deposits than those in Nevada, USA (Li, Z.P. and Peters, 1998). The amount and type of each alteration can vary from deposit to deposit.

Lithology and structures are important factors that control the formation and distribution of SRHG deposits in both the P.R. China and Nevada, USA. Common to almost all regions that host SRHG deposits are histories of large-scale compressional and extensional tectonic events (Li, Z.P. and Peters, 1998). Structures such as high-angle normal faults and fold crests commonly are trap sites for ore in these deposits. Faults functioned as regional- and local-scale conduits for ore-bearing fluids, while fold crests may have acted to trap or provide a release point for fluids as they flowed upward along these zones.

Fluid inclusion studies of ore and alteration minerals have been conducted in the P.R. China and Nevada, USA (Lu, H.Z., 1988; Arehart, 1996; Hofstra 1997; Wang and Zhang, 1999) and suggest that Chinese SRHG deposits formed at temperatures ranging from 165 to 290 °C and pressures of 52 to 560 bars. Nevada deposits appear to have formed at similar temperatures (200 to 250 °C), but generally higher pressures (400 to 800 bars).

The age of ore formation of SRHG deposits is perhaps the one characteristic that is the most difficult to determine. Many studies have been conducted in Nevada, USA but most have been inconclusive. Only a few studies have been conducted in the P.R. China and these too have been uncertain and show little agreement in their findings. The difficulties in dating these deposits include:

- They are deposited in sedimentary rocks following transport along high-angle faults cutting through numerous stratigraphic layers, with each layer representing various time intervals. Therefore, age determination by stratigraphic means can be extremely difficult and largely irrelevant.
- Syn-depositional alteration minerals, when present, are fine grained and low-temperature, making dating by radiometric means difficult at best.

Due to these difficulties, studies in the P.R. China and Nevada, USA have resulted in age determinations ranging from late Tertiary to very early Paleozoic. Seedorf (1991), using structural and stratigraphic constraints, reported an age of mineralization of mid-Tertiary. Arehart (1996) suggested a possible age of mineralization based on radiometric data as between 80 to 130 Ma. Radiometric studies conducted in China yield just as large a range, with ages ranging from 12.7 to almost 400 Ma (Li, Z.P. and Peters, 1998).

Regardless of age variances, the model adopted for the formation of the Chinese deposits is generally the same as the Nevada deposits, and it is reasonable to assume that clusters of deposits in the Qinling and Dian-Qian-Gui study areas may have resulted from the same tectono-thermal event. Fluids from several kilometers deep in the crust circulated through the surrounding rocks, scavenging Au and other metals. Regional-scale tectonic or possibly magmatic events resulted in an increase in temperature and pressure. This caused metals such as Au to go into solution. Au could have been carried in solution as a bisulfide complex, $[Au(HS)]^{-2}$ and migrated upwards along deep fractures or “feeder channels” (Wang and Zhang, 1999). As the fluids moved upward along these conduits, temperature and pressure decreased. When the temperature and pressure reached a certain threshold, Au and other minerals were deposited as equilibrium was disrupted. Another possibility is that these fluids rose until they came into contact with meteoric waters in carbonate rocks, once again disrupting equilibrium and resulting in Au deposition.

Geologic Setting

The Precambrian Yangtze craton lies in southeastern China (fig. 6-2) and is composed of a Proterozoic crystalline basement overlain by late Proterozoic to Mesozoic sedimentary and volcanic rocks. The geologic history of the craton is marked by numerous orogenies resulting in subduction and closure of Paleozoic-Mesozoic ocean basins along the craton's margin. As a result, the margin of the craton is characterized by sedimentary basins filled with oceanic sediments. It is within two of these basins that the Qinling and Dian-Qian-Gui study areas are situated. The Qinling area is located on the northwestern margin of the craton, while the Dian-Qian-Gui area is located on the southwestern margin (fig. 6-2). While both of the areas have comparable tectonic histories and features, there are a few differences.

Geologic Summary of the Qinling Area

The Qinling area, also known as the Chuan-Shan-Gan area, is positioned in a large, east-trending sedimentary basin separating the Precambrian Yangtze and Hubei cratons (fig. 6-2). The basin was formed between middle Paleozoic and early Mesozoic time by the deposition of greater than 10,000 m of sedimentary rock, the stratigraphy of which is as follows:

- Devonian – limestone interbedded with calcareous sandstone.
- Carboniferous – limestone, carbonaceous shale and quartz sandstone.
- Permian – limestone interbedded with siltstone and silty shale.

Igneous intrusions are found throughout the Qinling area and mainly consist of Mesozoic granite, granodiorite, and mafic rocks. Volcanic deposits are smaller in size and number and consist of late Paleozoic andesite and basalt. In general, SRHG deposits are not directly associated with volcanic or intrusive rocks.

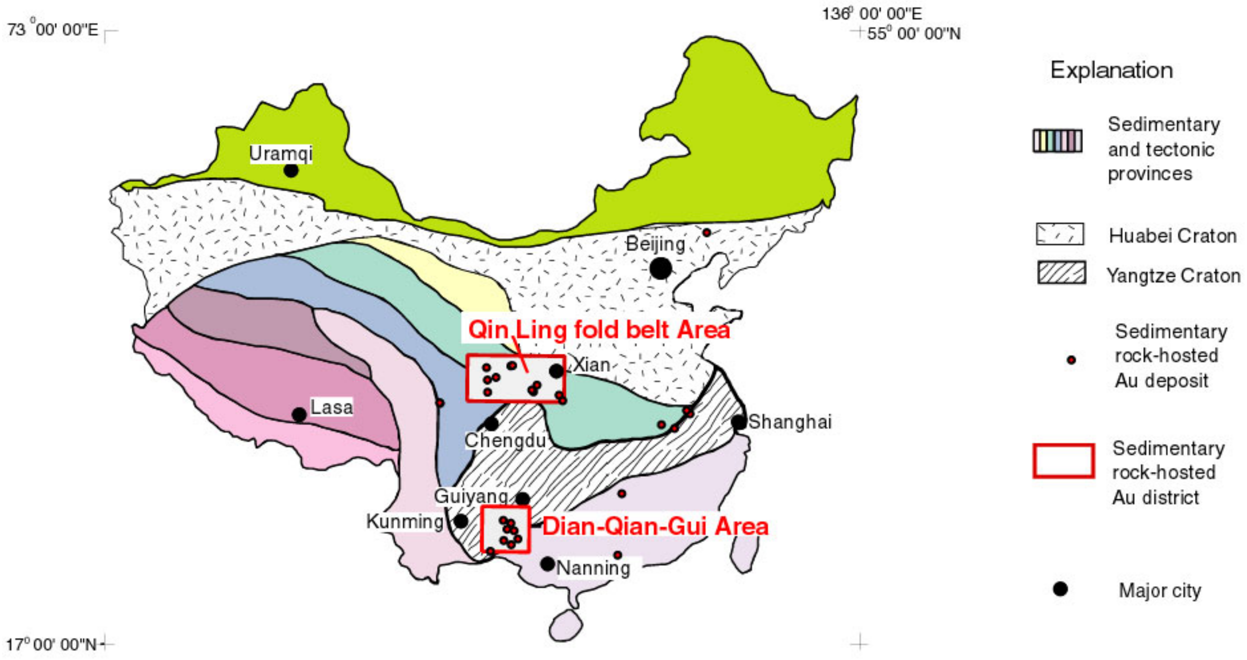

Figure 6-2. Tectonic setting of the Qinling and Dian-Qian-Gui areas. The Dian-Qian-Gui area is located in a sedimentary rock province along the southwestern margin of the Yangtze craton, while the Qinling area is positioned in a sedimentary basin that separates the Hubei and Yangtze cratons. Modified from Li, Z.P and Peters (1998).

The major tectonic feature of the Qinling area is the Lixian-Baiyun-Shanyang fault zone (6-3). This east-west trending fault system has been interpreted as a regional-scale shear zone, which is a remnant of subduction between the Hubei and Yangtze cratons. It is along this zone that SRHG deposits are commonly associated. This has led some to conclude that this zone was the major conduit for ore-forming fluids (Li, Z.P. and Peters, 1998).

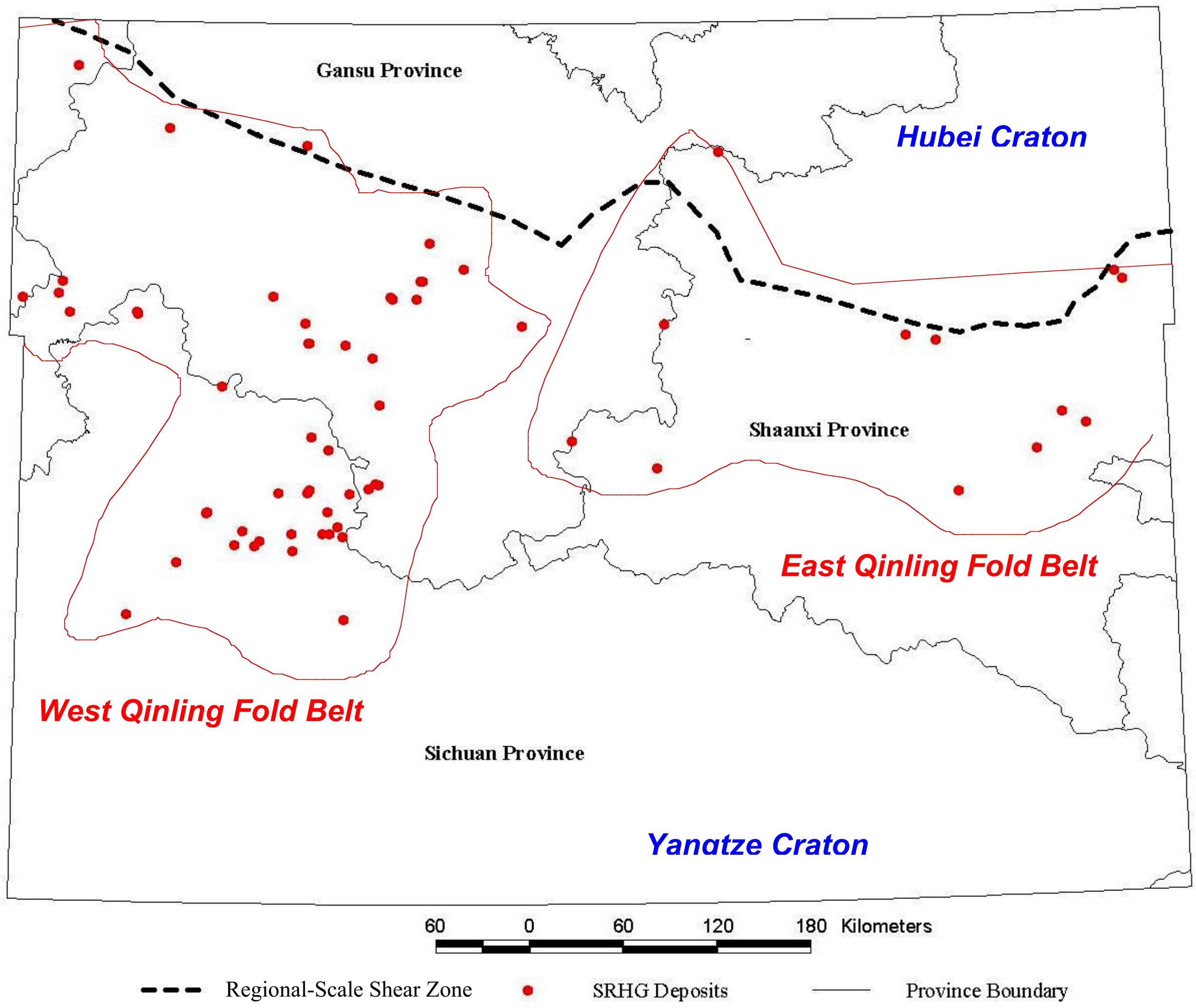

Figure 6-3. Generalized Tectonic Setting of the Qinling area.

Geologic Summary of the Dian-Qian-Gui Area

The Dian-Qian-Gui area has a geologic setting similar to that of the Qinling area where the edge of the Precambrian Yangtze craton is overlain by shallow and deep-water sedimentary and volcanoclastic rocks of Late Paleozoic to early Mesozoic in age. The stratigraphy of the sedimentary rocks is as follows:

- Carboniferous – bioclastic and cherty limestone.
- Permian – bioclastic and cherty limestone and argillite.
- Triassic – limestone, dolomite and argillite.

Igneous activity was far less pronounced in Dian-Qian-Gui than in the Qinling area. Intrusive rocks such as granite, diabase and gabbro are scattered across the north and south of the area, but are not common. Volcanic rocks are located in the northwestern part of the area and mainly consist of Paleozoic and Mesozoic basalt flows.

The Mesozoic Yanshanian Orogeny (210 to 90 Ma) had a major effect on the present day landscape and distribution of SRHG deposits in the Dian-Qian-Gui area. During this time, compression from the subduction of Pacific Basin plates under the eastern edge of the continent resulted in folding of the overlying sedimentary strata. Fold axis trends mainly east-northeast and north-northwest. Commonly, these folds are cut by faults. After folding occurred, major northwest-trending extensional structures formed, most notably the Youjiang

fault zone or fault system (fig. 6-4). This fault zone is thought to have acted as the major conduit for ore-forming fluids in the area (Li, Z.P. and Peters, 1998) (Chapter 3).

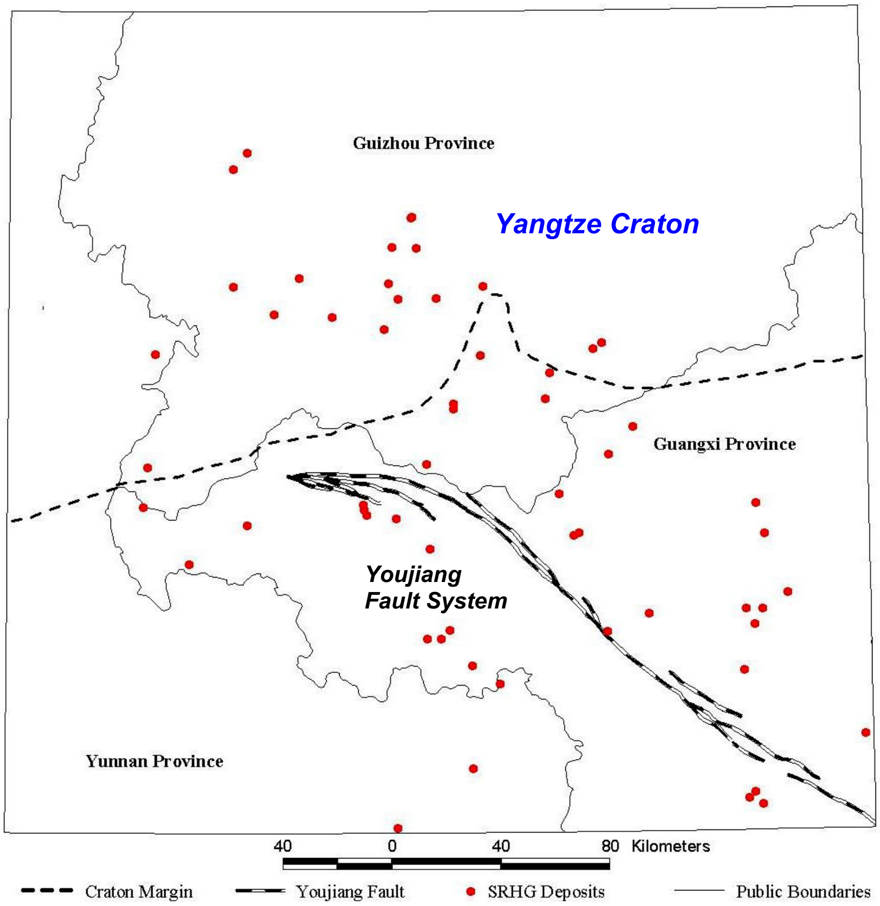

Figure 6-4. Generalized tectonic setting of the Dian-Qian-Gui area.

WEIGHTS-of-EVIDENCE (WofE) MODELING

Weights-of-evidence (WofE) is a GIS-based, data-driven methodology for integrating spatial data patterns and building predictive models. WofE uses (1) conditional probabilities to measure the spatial association between point-objects and patterns, and (2) Bayes' probability'theorem to mathematically integrate the patterns to predict the distribution of the point-objects. As applied in this study, the patterns represent geoscientific phenomena that are likely to be useful mineral predictors, and are referred to as *"evidence maps"*. The point-objects represent known mineral sites, and are referred to as *"training sites"*."

Evidence maps are typically multi-class and include representations of geological map units, structure, geochemical, and geophysical anomalies (as well as remotely sensed images and other earth observation data). In order to facilitate combination, the evidence maps are usually reduced to *"predictor maps"* of a few discrete states, typically binary- or ternary-class, where the spatial association between the training sites and an evidence map is optimized. The predictor maps collectively constitute *"layers of evidence"*.

Training sites are used to identify and weight the importance of predictor patterns on the evidence maps. Training sites collectively possess characteristics that are common to a particular deposit type (SRHG, for example). It is presumed that their location and presence enable prediction of the particular deposit type represented. Training sites are regarded as binary, either present or absent. There is no provision for modeling training site size, grade, or tonnage in WofE, as the training sites are not themselves classified or weighted, and each point is treated as equally important.

A WofE model consists of integrated predictor patterns and is expressed in the form of a single *"favorability map"*. The favorability map represents the spatial distribution of training sites in terms of the spatial distribution of predictor patterns, as well as the predicted distribution of yet unidentified sites.

The WofE method is based on a technique originally developed in a non-spatial context for medical diagnosis (Spiegelhalter and Knill-Jones, 1984) and has been modified by Bonham-Carter and others (1989) to deal with spatial prediction—"diagnosing" mineral occurrences using the "symptoms" of various geoscientific phenomena. The technique is discussed in detail in Bonham-Carter and others (1988, 1989) and Agterberg and others (1990). Wright and Bonham-Carter (1996) applied WofE in a mineral resource exploration context and yielded positive results when a new discovery was made in a favorable zone predicted by the model. In a mineral resource assessment context, Mihalasky (1999) and Raines (1999) demonstrated that WofE yields assessment tracts that are comparable to expert-delineated tracts (Cox and others, 1996).

Weights-of-evidence modeling was carried out in a geographical information system (GIS) environment using the ArcView® GIS extension *"Arc-SDM""*(Spatial Data Modeler), developed by the U.S. Geological Survey and the Geological Survey of Canada (Kemp, 2001). The analysis was performed within the confines of a user-defined geographic region, and is referred to as the *"study area"* (in this case, two study areas: Qinling and Dian-Qian-Gui; see figure 6-1).

Modeling Procedures

Weights-of-evidence modeling can be subdivided into three main procedures: (1) measurement of spatial association between the training sites and the evidence maps, (2) optimization of the evidence maps for prediction, and (3) combination of the predictor maps to create favorability maps (fig. 6-5). An overview of WofE modeling concepts, terminology, and techniques is given below. For a more thorough discussion of the modeling equations, and their derivations and applications, consult Bonham-Carter (1989), Agterberg (1990) and Bonham-Carter (1994).

In the first procedure, conditional probabilities that involve area proportions are used to determine the spatial association between the training sites and an evidence map. Each evidence map unit is treated individually as a binary pattern (evidence map unit present or absent), and is

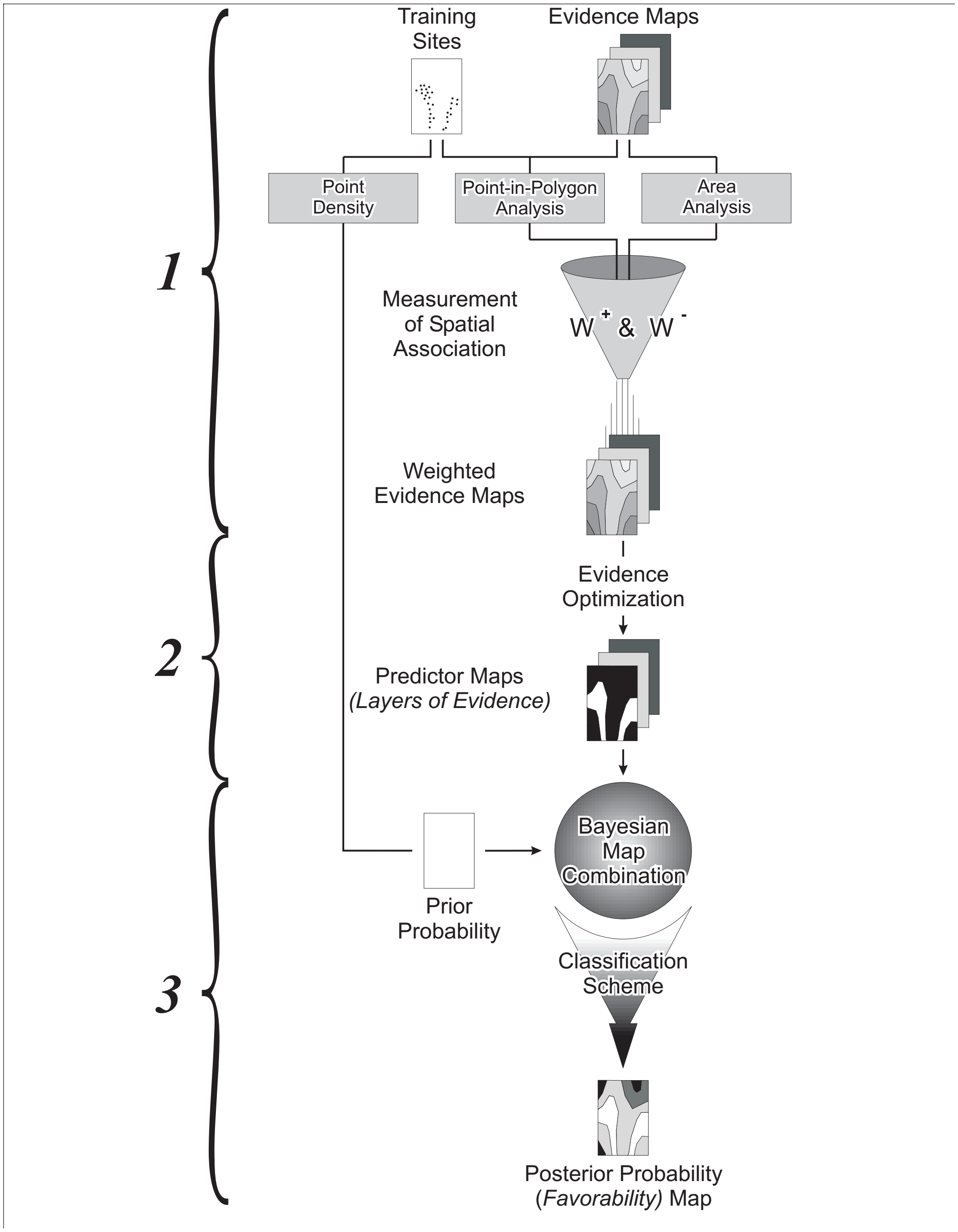

Figure 6-5. Flow chart illustrating the weights-of-evidence modeling method. The method is subdivided into 3 main procedures, as indicated by the numbered brackets on the left. See text for discussion.

composed of the area of the particular evidence map unit being evaluated and the combined total area of the remaining evidence map units. A training site likewise is regarded as a present or absent. For the purposes of analysis, a training site is assumed to occupy a small unit-cell area, which for this study is 1 km^2.

Two weights are calculated with respect to the training sites: W^+ for a particular evidence map unit present, W^- for absent. The value of the weights depend on the ratio of training sites that fall on a particular evidence map unit to the total number of training sites, versus, the ratio of the particular evidence map unit area to the total evidence map area. Where no spatial association exists (*i.e.*, the two ratios are equal), the weights are both zero; where there are more training sites in a particular evidence map unit than would be expected due to chance (*i.e.*, the ratio of training sites to map unit area is larger), W^+ is positive and W^- is negative. Where data is unknown or missing (incomplete evidence map coverage), the weights are assigned the value zero. The weights can be combined into a single coefficient called the contrast (C), where $C = W^+ - W^-$. Contrast provides a useful measure of the strength of the spatial association between the training sites and the individual evidence map units. Contrast is zero when the training sites and an individual evidence map unit overlap by the expected amount due to chance. It is greater than zero for positive spatial associations and less than zero for negative associations. Significance of C is estimated by calculating its Student-*t* value, or *"Studentized C"*, which is the ratio of C to its standard deviation.

In the second procedure, the evidence maps are reclassified to predictor maps of two units (predictor pattern present; predictor pattern absent), where the spatial association between the training sites and an evidence map is optimized. While reclassification to more than two or three units is possible, predictor maps of just a few units yield more stable and meaningful weights of spatial association and facilitate interpretation of the favorability map.

The reclassification of the evidence maps involves both objective and subjective methods. For each evidence map, an individual evidence map unit that is highly correlated (spatially) with the training sites may be selected as a predictor pattern, or multiple evidence map units may be grouped in such a way as to maximize the spatial association between the training sites and the evidence map. The weight estimates, the value of C, the variances of the weights and C, and the significance of C, are fundamental to identifying evidence map units that are optimal for prediction. A significance level of 1.282 (90 percent confidence, tabled Student-*t* value) was used for selecting predictor patterns in this study.

Nominal (or categorical) scale evidence maps, such as geological maps, are reclassified by grouping individual units that show strong spatial associations with the training sites (guided by what is both geologically reasonable and numerically advantageous). A bar graph is used to illustrate the weights of spatial association for each evidence map unit.

Ordinal (or ranked), interval, and ratio scale evidence maps, such as geophysical or geochemical anomaly maps, or distance buffer maps, can be reclassified by grouping successive cumulative evidence map unit areas, or by subjectively identifying anomalies. The optimum threshold is determined by the number of successively combined units that collectively demonstrate the strongest spatial association. In practice, a line graph is constructed which plots area-cumulative C along the *y*-axis and distance buffers or anomaly intensities along the *x*-axis, as shown in Figure 6-6. In this simple example, the area-cumulative C peaks at the 3rd interval on the *x*-axis. Reclassifying it into two units, 0-3 and 3-10, is one way to optimize the evidence map.

To facilitate the selection of a suitable threshold, Studentized C, W^+, W^-, and the inverse of W^- (Mihalasky and Raines, 2001) were also plotted. Studentized C assists in the selection of a statistically significant C-peak (the optimum threshold). W^+ and W^- provide additional information on the make up of C, such as whether it is composed predominantly of positive or negative weight, or equal proportions of both. The inverse of W^- provides a convenient, graphical means by which to illustrate the make up C. Where the W^+ and the inverse of W^- curves crossover, the relative influence of W^+ and W^- on C is roughly equal. That is, the magnitude of W^- is equal to the magnitude of W^+. Where the value for the inverse of W^- is less than W^+ (left of the crossover on the graph), C is composed of a greater proportion of W^+ than W^-.

Predictor patterns that are delineated using an optimum threshold to the left of the crossover serve to *include* areas likely to host the deposit-type(s) represented by the training sites. These predictor patterns are referred to as *"inclusive evidence"* and are characterized by narrowly-defined patterns with W^+ magnitudes that are significantly larger than W^-. Conversely, where the inverse of W^- is greater than W^+ (right of the crossover on the graph), C is composed of a greater proportion of W^- than W^+. Predictor patterns that are delineated using an optimum threshold to the

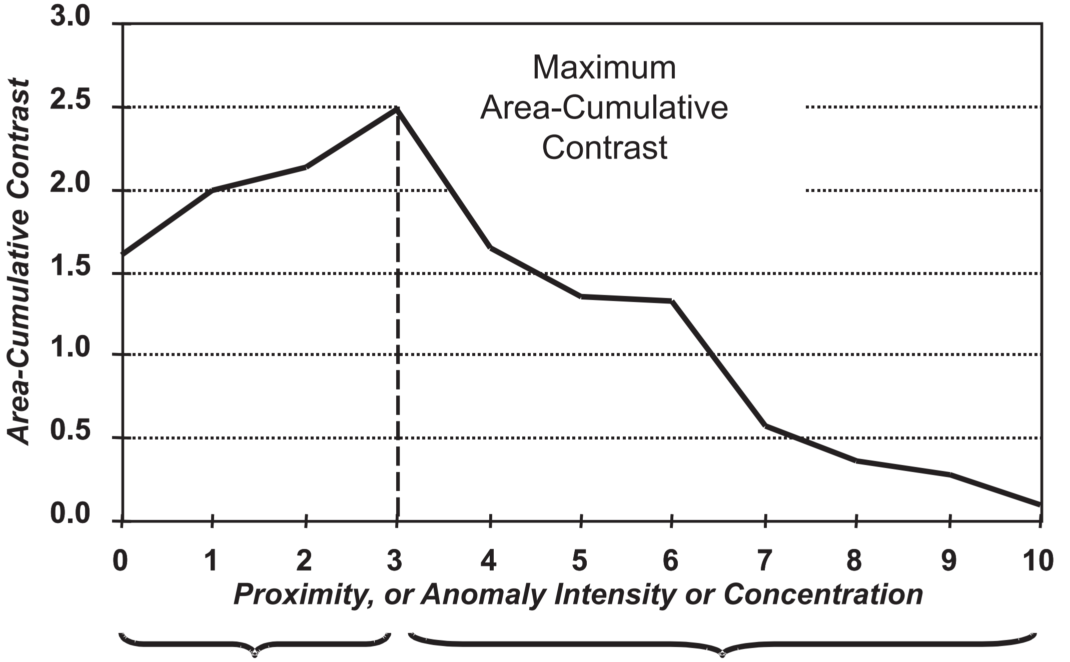

Map Unit Grouping	**0 - 3**	**3 - 10**
Proximity:	Pattern Present (W^+)	Pattern Absent (W^-)
Intensity:	Pattern Absent (W^-)	Pattern Present (W^+)
Concetration:	Pattern Absent (W^-)	Pattern Present (W^+)

Figure XX. Area-cumulative contrast curve for an evidence map that has 10 classes. This curve is used to help determine the optimum threshold between absence and presence of a predictor pattern for ordinal (or ranked), interval, or ratio scaled data. The table in the lower portion of the figure shows how the classes would be grouped into predictor pattern present or absent for measurements of proximity (0 = close; 10 = far), intensity (0 = low; 10 = high), and concentration (0 = low; 10 = high).

Figure 6-6. Area-cumulative contrast curve for an evidence map that has 10 classes. This curve is used to help determine the optimum threshold between absence and presence of a predictor pattern for ordinal (or ranked), interval, or ratio scaled data. The table in the lower portion of the figure shows how the classes would be grouped into predictor pattern present or absent for the measurements of proximity (0 = close; 10 = far), intensity (0 = low; 10 = high), and concentration (0 = low; 10 = high).

right of the crossover serve to *exclude* areas unlikely to host the deposit-type(s) represented by the training sites. These predictor patterns are referred to as *"exclusive evidence"* and are characterized by broadly-defined patterns with W^- magnitudes that are significantly larger than W^+. For this study, inclusive evidence was used where possible. The predictor patterns were delineated using an optimum threshold corresponding to the highest C-peak to the left of the W^+ and inverse of W^- crossover. This process will become clearer as the graphs for each model are presented.

In the third procedure, the predictor maps are combined using a log-linear formulation of Bayes' Rule to produce the favorability map. Central to Bayes' Rule is the concept of posterior and prior probabilities: the prior probability is the probability of the occurrence of a training site before evidence is considered; the posterior probability is the probability after the evidence is considered. In summary, the prior probability that a unit-cell area (1 km^2 in this case) contains a training site is successively updated by the addition of each new piece of evidence to produce a posterior probability. The prior probability is equal to the probability that the unit-cell (1 km^2 for this study) contains a training site, given no further information, and is equal to the density of known training sites in the study area.

Bayes' Rule effectively revises the prior probability by incorporating the new evidence into the model (Mendenhall and Reinmuth, 1974, p. 84). The posterior probability reflects both the prior and the new evidence, and with each subsequent addition of new evidence, the posterior is treated as the prior, thus providing a more efficient model for prediction (Bonham-Carter, 1994; Mendenhall and Reinmuth, 1974). The posterior probability calculated after the addition of new evidence may be larger or smaller than the prior probability, depending on the overlap combination of evidence maps and their weights (i.e., if evidence for the occurrence of a training site is added, the posterior probability rises, and vice versa) (Agterberg, 1989; Bonham-Carter et al, 1989). The degree to which a particular evidence map affects the posterior probability is dependent upon the strength of its spatial association with the training sites.

The favorability map is produced by applying a user-defined classification scheme to the posterior probabilities. A quantile approach to creating a classification scheme is often used. This is an area-based scheme where the posterior probability class intervals (the breakpoints) are determined so that each of the posterior probability classes is roughly equal in area. For this study, an alternative approach using natural breakpoints (which is the software default) was used, where the posterior probabilities were grouped into seven classes. The final classified map shows favorability of SRHG mineral site occurrence, expressed as the posterior probability that a unit cell contains a training site.

Conditional Independence

An important assumption made in WofE modeling is that the predictor maps be conditionally independent (CI) of one another with respect to the training sites (see Bonham-Carter, 1994a). The favorability values may be adversely affected if, at the locations of the training sites, the presence of a predictor pattern in one evidence map is dependent on the presence of a predictor pattern in another evidence map. Violation of CI results in either the over-estimation or under-estimation of posterior probabilities, and the predicted training site frequencies either notably exceed or fall short of the observed frequencies in the most and least favorable areas of the favorability map (Agterberg and others, 1990). In essence, the areas of highest and lowest posterior probability may be an artifact of pattern redundancy (overlap) among the predictor maps, and the amount of over-estimation or under-estimation is commonly non-linear.

The assumption of CI is necessary because calculation of the spatial weights of association is carried out independently between the training sites and each predictor map. The weights are then combined using a single equation, resulting in posterior probabilities that are not exactly the same as those calculated directly from the data (Agterberg, 1989b; Bonham-Carter, 1994a). Independent calculation allows for in-depth data exploration, providing the opportunity to examine bivariate relationships and yielding useful insights into the relative contributions of each predictor map.

In the earth sciences, complete CI is difficult to achieve because geoscientific data (hence the evidence maps) are commonly interrelated. Consider, for example, stream sediment geochemistry and bedrock lithology. There will obviously be some dependency because chemistry reflects the source rock type. Intuitively, the assumption of CI is almost always violated to some degree, generally more so as the number of evidence maps increases (Bonham-Carter, 1994). It is important to understand how serious the violation is so that the appropriate action can be taken to minimize the problem and so that proper judgments can be made when evaluating areas of high favorability.

The degree to which the CI assumption is satisfied can be tested for, and the purpose of such a test is to determine the magnitude of any predictor map pattern dependencies and to identify the map(s) responsible for the dependency. If a map is found to be in serious violation of CI, it can then be (1) rejected from the model, (2) spatially combined with another map in order to minimize the dependency, or (3) modified in some way as to reduce the problem (for more information, see Agterberg and others, 1990; Bonham-Carter, 1994a).

Two tests are applied to determine whether the assumption of CI is satisfied: a *pairwise* and an *overall* goodness-of-fit test, both of which make use of the observed versus the predicted number of observations (training sites).

The pairwise test measures CI between all possible pairings of predictor maps (with respect to the training sites) by calculating the χ^2 (chi-square) statistic for each map pair. This value is compared to a tabled «^{2} value, assuming one degree of freedom, for a given level of significance. For this study, a significance cutoff of 98 percent ($\chi^2 = 5.4$) was selected. Values higher than the selected cutoff were rejected, indicating that the assumption of CI between two predictor maps had been violated, therefore measures were taken to mitigate the dependency. Conditional independence may be present due to three-way or multi-way interactions, and testing for these cases is also possible, but for practical purposes, chi-square testing reveals the most serious CI violations (Bonham-Carter, 1994a).

The overall test is a measure of the CI between all of the predictor maps in a model as a whole. The overall test is very simple, consisting of a comparison of the predicted number of training sites to the observed number (observed/predicted, referred to as the "CI ratio"). A 10 percent to 15 percent difference in the number of predicted training sites from the number of observed (CI ratio of 0.9 to 0.85) indicates that some degree of redundancy exists among the predictor maps, suggesting that CI is being violated, and may warrant a check of the chi-square tests and some sort of remedial action (Bonham-Carter, 1994a). Unlike the chi-square, the overall test is not a formal test, and in practice, the predicted number of training sites is usually higher than the observed (Bonham-Carter, 1994a).

In many instances, a model will pass one, but not both, goodness-of-fit tests. The goal is to establish a model that contains the least amount of conditional dependency, which may involve eliminating or combining a number of predictor maps until this occurs. In the event that the assumption of CI is not fully satisfied, a model is still useful, but true probability estimates cannot be made nor are expected. In this instance, the calculated posterior probabilities, which are ratio-scale data, can be treated as ordinal-scale ranks and referred to as "favorabilities" (in the analysis and modeling sections of this paper below, the term "favorability" is used in place of probability). Interpretations as to which areas on the favorability map are more likely to host training sites can nonetheless be made. Since this study was concerned only with modeling the distribution of SRHG sites, not with estimating their number or size, achieving CI was not an important consideration.

Error and Uncertainty

An important aspect to interpreting a favorability map is recognizing and quantifying the uncertainty inherent to the posterior probabilities. The two primary sources of uncertainty are: (1) the uncertainty due to variances in weight estimates (W^+ and W^-); and (2) the uncertainty due to one or more of the predictor maps having incomplete coverage (i.e., missing data) (Bonham-Carter and others, 1989).

The uncertainty due to the weights, which includes the uncertainty of the prior probability, is in general correlated to the posterior probability (Bonham-Carter and others, 1989). Uncertainty due to missing data, where one or more of the predictor map patterns is unknown or incomplete in a given region, results in posterior probability estimates that are less certain than those based on more, or all, of the predictor map patterns (Agterberg and others, 1990; Bonham-Carter and others, 1989). The uncertainties due to weights and due to missing data may be examined separately, or may be combined to examine total uncertainty.

In addition to the uncertainties due to weights variances and missing data, a *relative certainty* (variance) of the posterior probability can be calculated by dividing the posterior probability by its standard deviation, which in effect applies an informal Student *t*-test to determine whether the posterior probability is greater than zero for a given level of statistical significance (i.e., compared to a tabled *t*-value) (Bonham-Carter and others, 1989; Agterberg and others, 1993). The larger the *t*-value over the critical tabled *t*-value cutoff, the greater the certainty of the posterior probability (i.e., the larger the posterior probability compared to its standard deviation). The relative certainty is often more useful than the weights variances or missing data uncertainties because it indicates the degree of confidence to which the posterior probabilities are meaningful, as opposed to being an artifact of chance effects or interactions. Care should be taken when interpreting the relative certainty because it is based on a normal distribution and sensitive to CI violations.

The four uncertainty factors (weight variances, missing data, total, and relative) may be used to create uncertainty maps for comparison to the favorability map, or the uncertainty factors may be combined in various ways and reclassified to a binary-class map which can be used to mask-out areas of the favorability map that are deemed to be too uncertain (Bonham-Carter and others, 1989; Bonham-Carter, 1994a).

DATASETS and ANALYSIS

Evidence maps used in WofE modeling of SRHG sites are primarily variations of host units and structure derived from digital geologic maps, although other databases also were consulted. The following presentation discusses both study areas in turn from raw data, to evidence maps, to analysis of spatial associations with training sites, and finally, to the generation of predictor maps. The analyses and results are presented in figures and tables. Model validation is then discussed along with overall CI.

The standard projection used for all GIS dataset processing and display is as follows:

Projection: ***Albers Equal Area Conic***
Central Meridian: ***105°E***
Origin: ***0°***
1st Standard Parallel: ***25°N***
2nd Standard Parallel: ***47°N***
Datum: ***WGS84***

All base datasets have a scale of 1:1,000,000. At this scale, resolution or error is +/-1000 m. In order to account for this error, all buffering of linear features was done at 2 km intervals from 0 to 50 km.

Training Set

The training set was modified from the database of Li, Z.P. and Peters [v1.2] (1998) by adding more accurate longitude and latitudes to the existing 113 sites. This revision was carried out as part of an on-going collaboration and compilation by Tianjin Geologic Academy and the U.S. Geological Survey. In addition, new sites were added to the database, for a combined total of over 160 sites. Of these, 68 and 61 are located in the Qinling and Dian-Qian-Gui areas respectively (tables 6-1 and 6-2). The classification and characteristics of these sites are detailed in Chapters 1 through 5., and final corrections to this database—not included in this analysis and this Chapter—are contained in Appendix IV.

ID	DEPOSIT	PROVINCE	LATITUDE	LONGITUDE
1	Amangshaji	Gansu	35.4000	102.3333
2	Anjiacha	Gansu	33.9453	105.4994
3	Badu	Gansu	33.5000	104.5000
5	Badun	Shaanxi	34.9200	106.9000
14	Ceyang	Gansu	34.1100	103.7500
20	Damingshan	Gansu	34.0833	101.9833
21	Daoqiejia	Sichuan	32.8958	104.1444
23	Dayakou	Sichuan	32.3000	102.7600
24	Dazhai	Sichuan	32.6992	103.6417
25	Dongbeizhai	Sichuan	32.7844	103.5564
26	Erdaqiao	Sichuan	33.3175	104.0269
35	Greatwall	Gansu	34.1000	104.7583
37	Guojiapo	Gansu	33.0494	104.4958
39	Heduosi	Sichuan	33.5000	104.5000
41	Heye	Sichuan	33.2444	104.1489
42	Huachanggou	Shaanxi	33.2953	105.8422
43	Huameinao	Sichuan	33.0000	103.8000
44	Huanglong	Sichuan	32.7708	103.8917
47	Huangtupo	Sichuan	32.9958	104.2950
49	Hujiamo	Sichuan	32.8100	104.2156
50	Jiangjuncha	Shaanxi	34.1817	109.6756
52	Jiawuchi	Gansu	34.2000	104.7833
54	Jiguanzui	Gansu	34.0139	102.7917
55	Jilongshan	Gansu	33.8500	104.0000
57	Jindonggou	Gansu	34.0067	102.3200
58	Jinlongshan	Gansu	35.0544	103.0000
63	Jiuyuan	Gansu	33.8361	104.2608
64	Kama	Gansu	34.1000	104.5900
69	Laodou	Gansu	35.0544	103.0000
71	Lazikuo	Gansu	34.9636	103.9783
74	Lijiagou	Shaanxi	33.1361	106.4342
76	Longdishui	Sichuan	32.7708	104.1069
77	Longhue	Sichuan	33.6000	103.4000
80	Longquan	Gansu	34.2000	104.8000
85	Lubuge	Gansu	34.4181	104.8478
86	Luoba	Gansu	34.2725	105.0867
87	LuoDa	Gansu	33.9636	103.9783
91	Mahuanggou	Gansu	34.0017	102.8000
94	Maoling	Sichuan	32.7000	103.5000
95	Maquan	Sichuan	33.0167	104.0167
97	Maxuong	Shaanxi	33.2000	109.0806
98	Miaolong	Gansu	33.8500	104.0028
100	Mingzhushan	Gansu	34.4181	104.8478
107	Pangjiahe	Gansu	34.1139	104.5750
110	Pingding	Gansu	33.7636	104.4478
117	Puzilong	Sichuan	32.6700	103.9000
118	Qiaoqiaoshang	Sichuan	32.7250	103.6750
120	Qilixia	Sichuan	33.0000	104.0000
126	Quongme	Shaanxi	34.1361	109.7297
129	Sanrengou	Gansu	34.1800	102.2600
133	Shijiba	Gansu	33.0544	104.4783
136	Shuiniujia	Sichuan	32.7528	104.2500
137	Shuishengou	Sichuan	32.6000	103.1000
139	Songpan	Gansu	34.1089	102.2389
140	Songpnagou	Sichuan	32.7681	104.1567
147	Tuongkangling	Shaanxi	32.9700	108.5300
150	Woxi	Shaanxi	33.8300	108.4000
152	Xiangzicha	Shaanxi	34.1361	109.7297
155	Xidayu	Shaanxi	33.4000	109.2700
156	Xinguan	Gansu	33.0278	104.4278
159	Yaerma	Shaanxi	33.3300	109.4300
160	Yangjishan	Shaanxi	33.8600	108.1900
163	Yata	Shaanxi	34.0800	106.5300
166	Yinchanggou	Sichuan	32.2850	104.2583
167	Zheboshan	Sichuan	32.8853	103.3072
169	Zhepeshan	Sichuan	32.6700	103.9000
172	Zhongqu	Gansu	34.1089	102.2389
173	Zhuongqu	Sichuan	32.8800	103.3000

TABLE 6-1. Names and coordinates of SRHG training sites in the Qinling area.

ID	DEPOSIT	PROVINCE	LATITUDE	LONGITUDE	□ID	DEPOSIT	PROVINCE	LATITUDE	LONGITUDE
4	Badu	Guangxi	24.2500	105.7300	□84	Loudong	Guangxi	24.3633	106.9500
6	Baguamiao	Guizhou	25.0000	105.7500	□88	Luolou	Guizhou	24.3100	106.8000
7	Baidi	Guizhou	24.7000	106.1300	□89	Maanqiao	Guangxi	24.6333	105.4328
9	Bannian	Guizhou	24.8000	105.6500	□93	Manaoke	Guangxi	25.6167	105.6000
12	Baxi	Guizhou	25.6200	105.6028	□99	Mingshan	Guangxi	24.2600	106.8300
13	Beiyinpe	Guizhou	24.9833	105.7500	□103	Nabi	Gansu	24.0700	105.9100
18	Dachang	Guizhou	25.0167	106.0833	□105	Nibao	Guizhou	25.5167	105.6167
19	Daguan	Guangxi	24.3000	106.4500	□108	Pegao	Guizhou	25.7800	104.9500
22	Dashui	Guizhou	25.3000	105.1000	□11	Pingshan	Gansu	24.5600	106.1800
29	Gaojiaao	Guangxi	24.2200	105.7000	□12	Pingtang	Hunan	24.5200	105.6600
30	Gaolong	Yunnan	24.2200	105.6500	□13	Pingwang	Shaanxi	24.2400	106.3000
31	Gedang	Yunnan	23.5900	105.5400	□15	Posang	Guangxi	23.8900	107.2200
33	Gengxin	Guangxi	24.6600	106.8400	□16	Pouyajing	Guizhou	25.2000	106.2900
34	Getang	Yunnan	25.2900	105.3100	□19	Qilicun	Guangxi	24.6592	104.6250
51	Jiaoquan	Guizhou	25.3900	105.8600	□122	Qingping	Guizhou	25.1000	106.1000
53	Jidoman	Guangxi	23.7000	106.8200	□123	Qiuling	Guizhou	25.4000	105.5167
56	Jinba	Yunnan	23.7800	105.8200	□131	Shaziling	Guizhou	25.2500	105.5000
59	Jinshan	Guizhou	25.3500	105.6900	□138	Sixiangchang	Guangxi	24.6667	105.4200
60	Jinya	Guangxi	24.5600	106.8700	□141	Tangshang	Guangxi	24.4700	104.7900
62	Jinzhudong	Gansu	24.9200	106.4000	□142	Tangxinzhai	Guizhou	25.4200	105.1900
66	Laerma	Guangxi	24.6000	105.0000	□143	Tianwan	Guangxi	24.6592	104.6250
67	Langquan	Guangxi	24.8300	106.3100	□144	Tieshengou	Guangxi	24.6600	106.8400
68	Lannigou	Guangxi	25.1600	105.8500	□148	Wangme	Guizhou	25.3900	105.8600
72	Lianhecun	Guizhou	25.3500	105.5500	□149	Weihuai	Guangxi	23.6600	106.8500
73	Liba	Guizhou	25.1667	104.6667	□158	Xuongwu	Guangxi	24.3100	106.8600
75	Longchuan	Sichuan	24.1100	106.8000	□161	Yangyou	Guangxi	24.1300	105.8100
78	Longhuo	Guangxi	24.6200	105.5400	□162	Yaojian	Guizhou	25.3900	104.9500
79	Longna	Liaoning	24.7900	104.6400	□164	Yiaxiang	Guangxi	24.5700	106.2000
81	Longshan	Guangxi	24.6500	105.4233	□168	Zhen'an	Guizhou	25.1800	106.2600
82	Longwanggou	Guizhou	25.8333	105.0000	□174	Zimudang	Shaanxi	25.5200	105.5300
83	Longzhen	Guangxi	23.6800	106.8000					

TABLE 6-2. Names and coordinates of SRHG training sites in the Dian-Qian-Gui area.

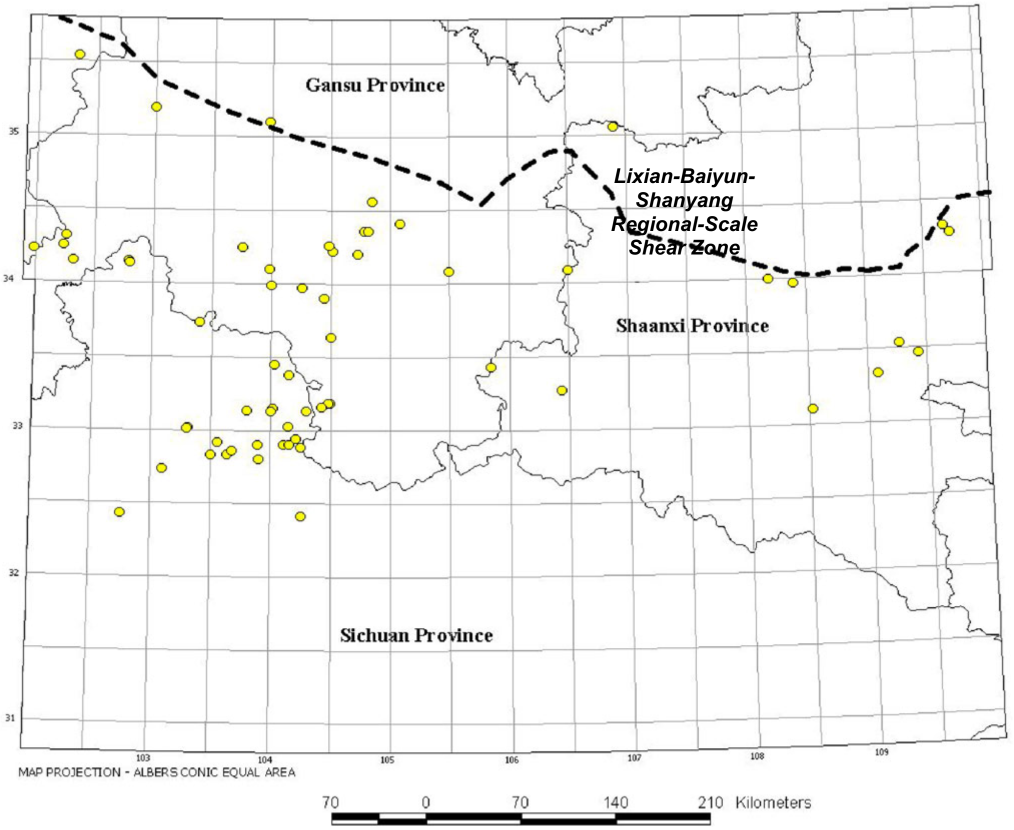

Figure 6-7. SRHG training sites in the Qinling study area. Names and locations of deposits are listed in Table 6-1.

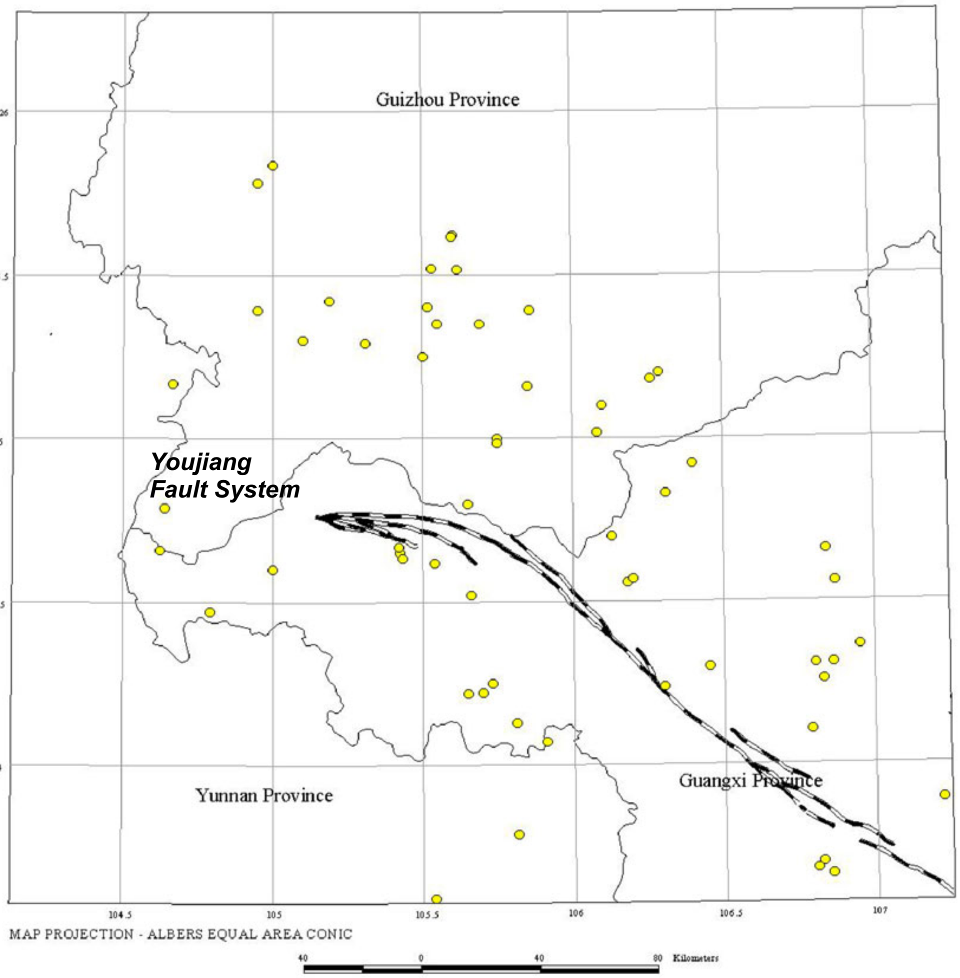

Figure 6-8. SRHG training sites in the Dian-Qian-Gui study area. Names and locations of deposits are listed in Table 6-2.

The distribution of the 68 SRHG sites in the Qinling area are shown in figure 6-7 (names and coordinates are listed in table 6-1). The sites lie in an approximately east-west trending, 25–km-wide zone. It is also of interest that while SRHG sites are present across this area, the majority lie in the northern and southern regions of the Gansu and Sichuan provinces, respectively. Note the location of the Precambrian Yangtze craton, approximately 300 km from the large cluster of sites (figs. 6-7 and 6-8).

Distribution of the 61 SRHG sites in the Dian-Qian-Gui area are shown in figure 6-8. Their names and coordinates are included in table 6-2. The sites are primarily located in the Guizhou and Guangxi Provinces. Note that they appear to be distributed northwest-southeast, at varying distances (<100 km) along the Youjiang fault zone.

Layers of Evidence

The main evidence data used in this analysis were geological map unit, Paleozoic-Mesozoic geological map unit contacts, lithodiversity, fault proximity, topographic slope, and anticline hinge proximity. Experience and expert-based knowledge was used to select and evaluate the suitability of these datasets for WofE modeling.

Geologic Map Units

Geologic maps used as evidence layers were obtained from *Geologic Data Systems, Inc.* (GDS), Denver, CO and from unpublished data sources in the USGS. This data was compiled from geologic province maps ranging in scale from 1:500,000 to 1:2,500,000. The maps were reconciled to a scale of 1:1,000,000 and merged together. The use of these multiple province maps resulted in some areas of the evidence maps containing more detail than others, and in some instances, there is little uniformity in labeling of units. This posed problems, specifically with units converging at province borders. In many instances, several units in one province were grouped together as one unit in an adjacent province. In such cases, the single unit was used for naming purposes. Map colors and legends used for the resulting geologic maps are based on several published geologic maps of the P.R. China.

The geological map used for analysis of spatial associations in the Qinling study area, after modifications, is presented in figure 6-9. The corresponding legend is provided in figure 6-10. The Qinling fold belt is clearly delineated by the strong folding of geologic units in the central and southern regions of the map. The units of interest to this analysis are the sedimentary carbonate units of Devonian to Cretaceous age (refer to legend, fig. 6-10). Igneous units also are present throughout this region, most notably intrusive granites (dark red) in the center of the map.

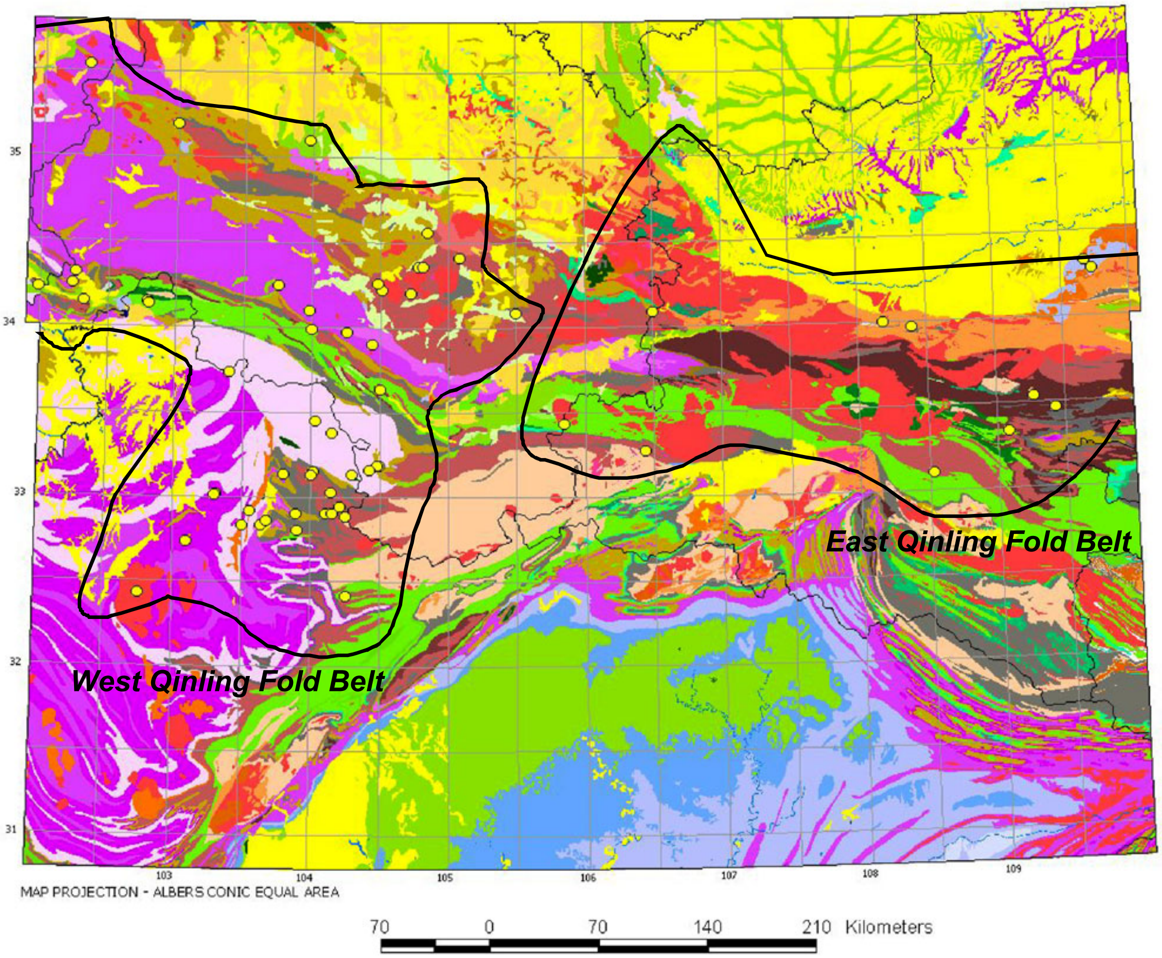

Figure 6-9. Geologic map of the Qinling area (legend is found in Figure 6-10).

EXPLANATION

STRATIGRAPHY

	Quaternary
Q	Alluvium, mud, silt, loess; pebble beds in west Qinling area
	Neogene
N	Mainly continental clastics, volcanics in Jinghong area
	Eogene
E	Clastic rocks with volcanics in eastern Yunnan
	Cretaceous
K K2 K1	Mainly continental and marine clastics with minor volcanics in western Qinling area
	Jurassic
J J3 J2 J1	Continental clastic rocks with intrusives in western Qinling area
T-J	Incorporated beds; undivided
	Triassic
T T3 T2 T1	Carbonates interbedded with sandstone and shale, volcanics in Zhongdian and Baoshan areas
P-T	Incorporated beds; undivided
	Permian
P P2 P1	Continental clastic rocks interbedded with coal in Qinling area, volcanics in north Yunnan
MP-P	Incorporated beds; undivided
	Mississipian-Pennsylvanian
MP MP3 MP2 MP1	Continental clastics; limestone interbedded with volcanics in Weixi area
D-MP	Incorporated beds; undivided
	Devonian
D D3 D2 D1	Marine and continental clastics, volcanics in Jinghong area
S-D	Incorporated beds; undivided
	Silurian
S S3 S2 S1	Marine clastics & mixed carbonate rocks in Yangtze region, vocanic rocks in west Qinling area
O-S	Incorporated beds; undivided
	Ordovician
O O3 O2 O1	Continental carbonate and clastic rocks, shallow marine volcanics west Qinling
	Cambrian
C	Clastic and carbonate rocks in Yangtze region
	Precambrian
pC pC3 pC2 pC1	Undivided

INTRUSIVE ROCKS

	1. Granitoids
gd	granodiorite
g	granite
xo	quartz-syenite (porphyry)
eo	quartz-monzonite (porphyry)
do	quartz-diorite (porphyry)
	2. Diorites
d	diorite
	3. Mafic rocks
n	gabbro
bm	diabase
	4. Ultramafic rocks
s	peridotite
pi	pyroxenite (porphyrite)
	5. Alkanline rocks
k	alkaline rocks
b	Basalts
x	syenite (porphyry)

VOLCANIC ROCKS

a	Andesites

AGE SUBDIVISIONS

Age subdivisions appear as suffixes to formation alphanumeric codes:

5 = Yanshanian
5-3 = Late Yanshanian
5-2 = Early Yanshanian
5-1 = Indosinian
4 = Variscan
3 = Caledonian
3-2 = Late Caledonian
3-1 = Early Caledonian

Figure 6-10. Legend for the geological map of the Qinling and Dian-Qian-Gui area (see Figures 9 and 12, respectively). Legend layout, style, and geological map unit classification scheme is adopted from the Geological Map of China (Cheng, 1990). See Cheng (1990) and Wang (199) for additional details.

The spatial associations between the training sites and the geological map units are presented in table 6-3. The table shows only those units that contain sites and is sorted in descending order by Studentized contrast to aid in interpretation. Five units have a Studentized contrast greater than the desired 1.282, as well as positive W^+ values. These units, S_1, D_1, D_2, P_1 and T_3, correspond to marine carbonates of Silurian (S), Devonian (D), Permian (P) and Triassic (T) age, respectively. The very high contrasts of the D_1, D_2 and P_1 units combined with their large W^+ values make them well suited as predictors. The remaining two units, T_3 and S_1, also were selected as predictors due to their W^+ values. After analysis of the spatial association between training sites and geological map units, the geological evidence map was reduced to a predictor map, which is illustrated in Figure 6-11.

In the Dian-Qian-Gui study area, similar problems to those found in the geological map of the Qinling study area were encountered. The map was modified in much the same way as it was for the Qinling area, and is presented in figure 6-12. The same legend is used for both the Qinling and Dian-Qian-Gui geological maps, therefore for an

explanation of the units in figure 6-12, refer to figure 6-10. The major geological map unit, T_1 (purple), a Triassic carbonate unit, occupies over 50,000 km^2 of the Dian-Qian-Gui area and contains more than half (31) of the training sites. The other noticeable features on the geological map are the circular structures in the middle of the map area. These are domes that act as structural windows to the underlying Paleozoic carbonate lithologies beneath the Triassic sedimentary rocks.

The spatial associations between the training sites and geological map units in the Dian-Qian-Gui area are presented in table 6-4. The table is sorted in descending order by Studentized contrast. Inspection of the table reveals that there are only two units, P and P_2, which have Student-*t* values greater than 1.282. The legend indicates that these are both Permian continental clastic units. These units were selected as predictors on the basis of high W^+ values. The geological predictor map for the Dian-Qian-Gui area is presented in Figure 6-13, and detailed in Appendix 6-1 of this report.

UNIT	AREA (Km^2)	No. of Deposits	W+	W-	Contrast	Studentized Contrast
D2	23058.2900	15	1.3821	-0.1922	1.5744	5.3817
D1	1341.2000	2	2.2125	-0.0266	2.2392	3.1175
P1	12879.3200	6	1.0481	-0.0609	1.1090	2.5933
T3	18879.3600	7	0.8197	-0.0622	0.8819	2.2095
g5-1	16705.4200	6	0.7878	-0.0514	0.8393	1.9626
S1	23552.7900	7	0.5984	-0.0504	0.6488	1.6256
pC2	9589.3100	2	0.2442	-0.0065	0.2507	0.3493
T1	37958.7200	6	-0.0331	0.0033	-0.0364	-0.0851
D	6683.2500	1	-0.0880	0.0014	-0.0894	-0.0887
J2	21012.1200	3	-0.1349	0.0067	-0.1416	-0.2397
T	25780.6200	3	-0.3394	0.0188	-0.3583	-0.6067
pC3	19308.2000	2	-0.4558	0.0177	-0.4735	-0.6596
K	34527.1900	4	-0.3439	0.0260	-0.3699	-0.7176
Q	76250.5400	4	-1.1362	0.1418	-1.2780	-2.4796

TABLE 6-3. Weights of spatial association calculated for geological map units in the Qinling area. Note that weights with Studentized contrast values greater the desired 1.282 cutoff are shaded in light gray. Unit codes correspond to those shown in Figure 6-10.

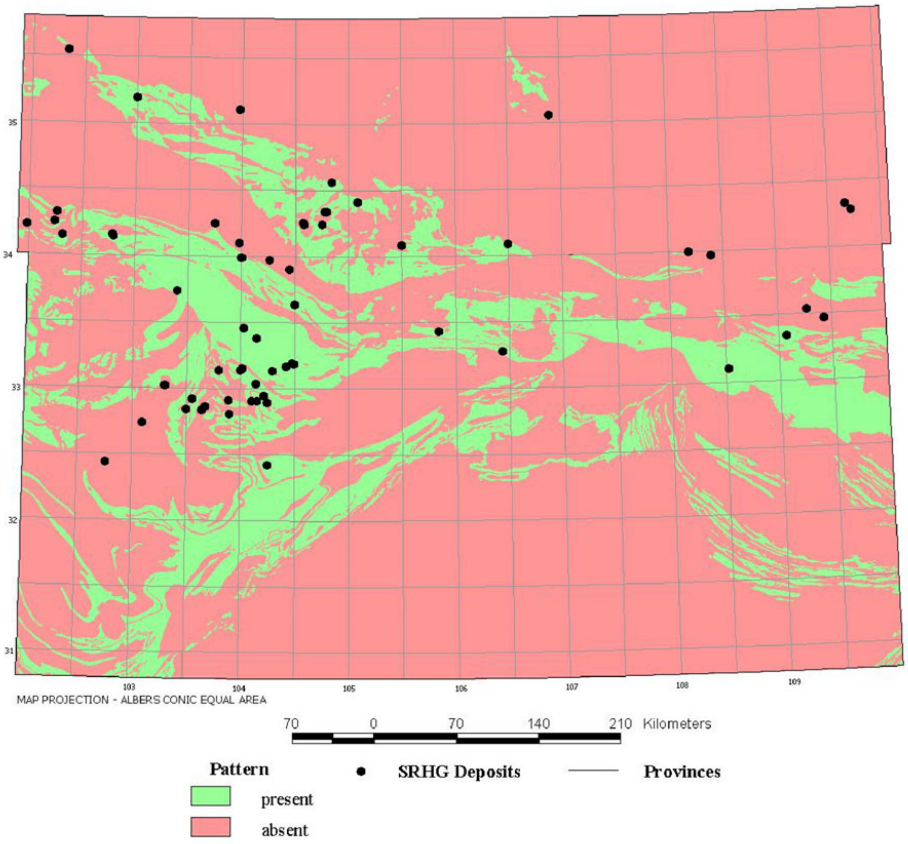

Figure 6-11. Predictor map of geological map units, Qinling area.

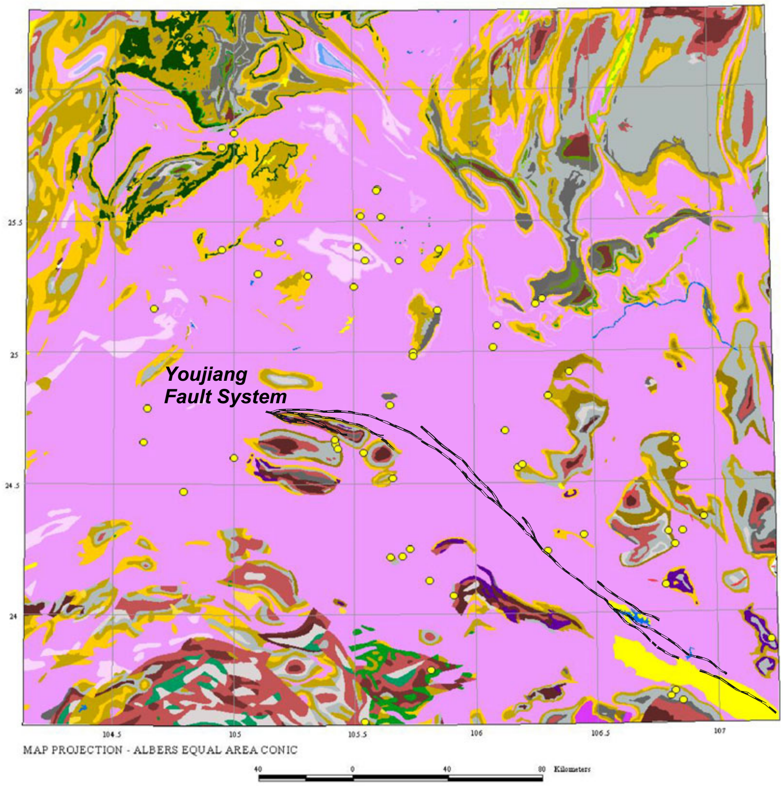

Figure 6-12. Geological map of Dian-Qian-Gui area (legend is found in Figure 6-10).

Unit	Area (Km²)	No. of Deposits	W+	W-	Contrast	Studentized Contrast
P1	8005.3300	5	0.0294	-0.0027	-0.0321	3.1007
P2	6891.2500	11	0.9099	-0.1235	1.0333	2.9032
T1	55253.8400	31	-0.1368	0.1642	-0.3010	0.8215
D2	3613.3200	1	-0.8437	0.0223	-0.8661	0.3096
MP1	995.9500	0				0.2128
b	1196.1900	0				0.2008
T2	1309.8700	1	0.1715	-0.0026	0.1741	0.1726
MP2	8267.0900	6	0.1208	-0.0123	0.1332	-0.0688
K	121.2700	0				-0.8588
D1	1044.6200	0				-1.1749

TABLE 6-4. Weights of spatial association calculated for geological map units in the Dian-Qian-Gui area. Note that weights with Studentized contrast values greater the desired 1.282 cutoff are shaded in light gray. Unit codes correspond to those shown in Figure 10.

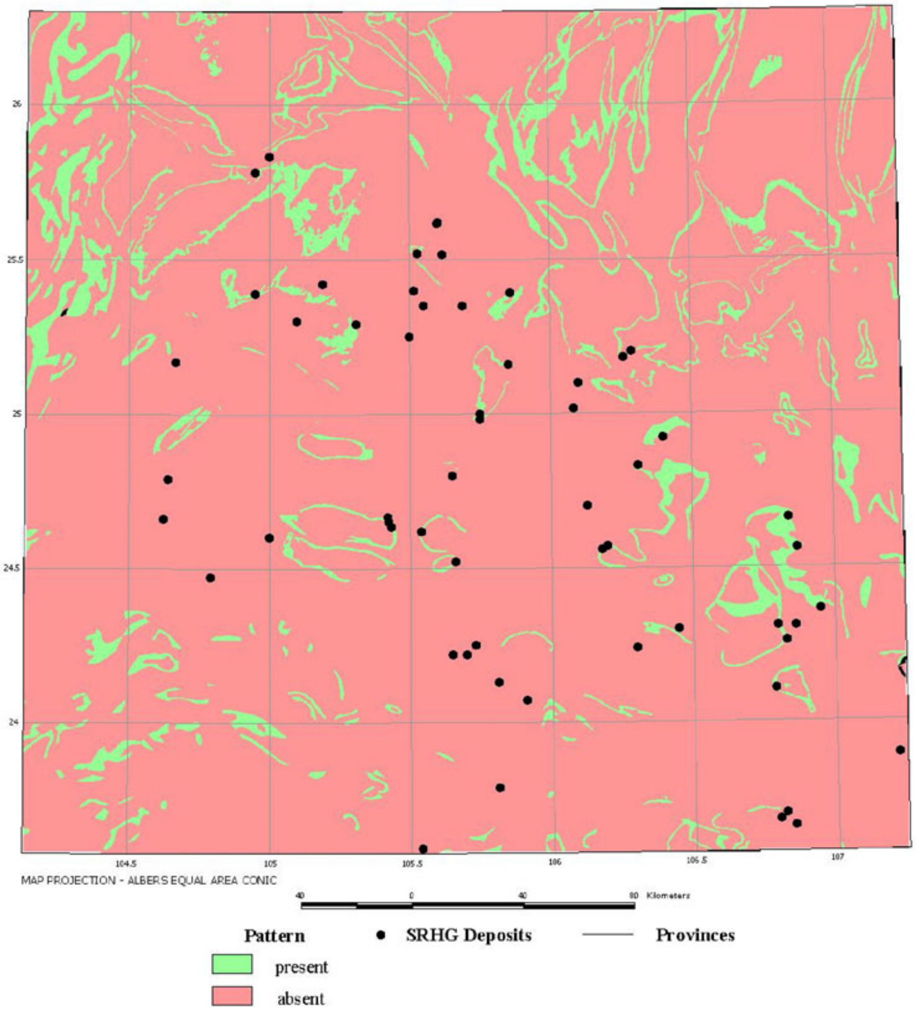

Figure 6-13. Predictor map of geological map units, Dian-Qian-Gui Area.

Lithodiversity

Maps of lithodiversity were constructed for use as evidence maps. This technique, developed by Mihalasky and Bonham-Carter (1999, 2001), involves calculating the number of geological map units in a square-shaped, sampling neighborhood. Their research indicates that the spatial association between mineral sites and lithodiversity increases with increasing lithodiversity. Lithodiversity is thought to represent complex structure and stratigraphy, which is requisite for the formation of mineral deposits. With this in mind, the technique involves breaking the region down into square-shaped sample neighborhoods, in this case 10 by 10 km neighborhoods, and calculating the lithodiversity for each. A 10 by 10 km neighborhood was chosen because it is the most suitable dimension for a 1:1,000,000 scale geological map (see Mihalasky and Bonham-Carter, 2001) and the 10 km lithodiversity map has a greater spatial association with the training sites than either 5 km or larger sample neighborhood maps.

The 10 km lithodiversity map for the Qinling area is shown in figure 6-14. A maximum of 13 geological map units was determined for a 10 by 10 km neighborhood size. Warmer colors indicate high lithodiversity, whereas cooler colors indicate lower values. The trend of the Qinling fold belt is reflected very well by high lithodiversity values, as illustrated by the general east-west pattern of warmer colors. The spatial association between lithodiversity and the training sites is shown using a bar graph in figure 15. Reading the graph from left to right, W^+ and Studentized contrast values remain negative until a lithodiversity of 3 is reached. This

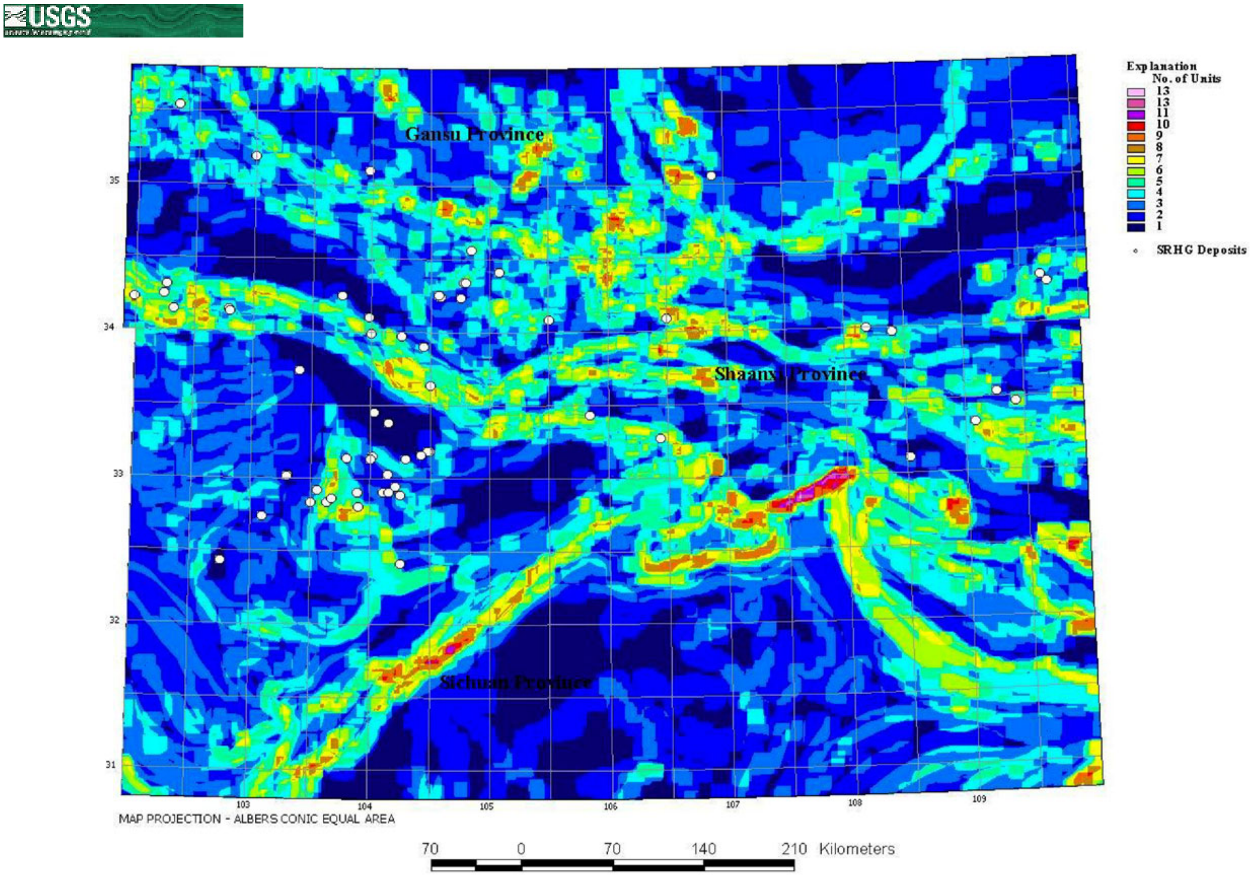

Figure 6-14. Map of lithodiversity, Qinling area. See explanation in text.

indicates that areas containing 3 or more geological units within the 10 by 10 km sample neighborhood have a positive spatial association with training sites. Therefore, lithodiversity values of 1 and 2 were classified as predictor map pattern absent, and values of 3 or more as predictor map pattern present. The lithodiversity predictor map is presented in figure 6-16.

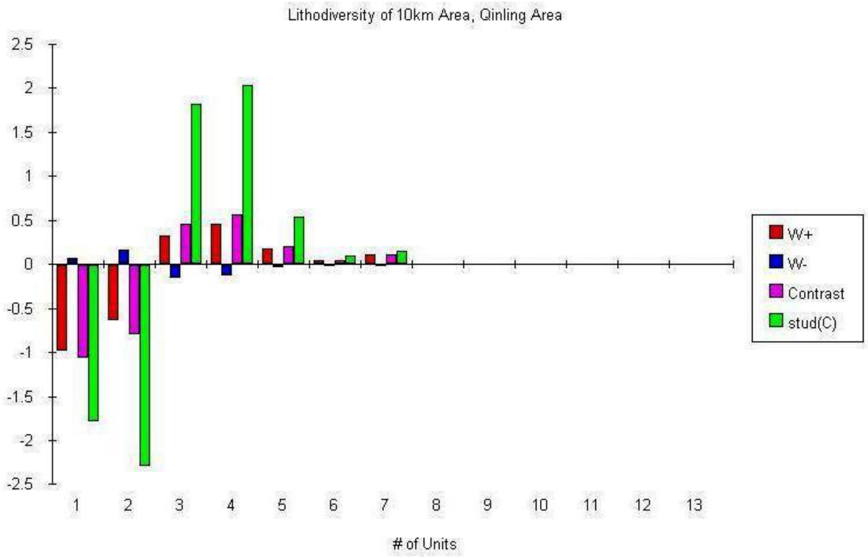

Figure 6-15. Spatial association between lithodiversity and training sites, Qinling area.

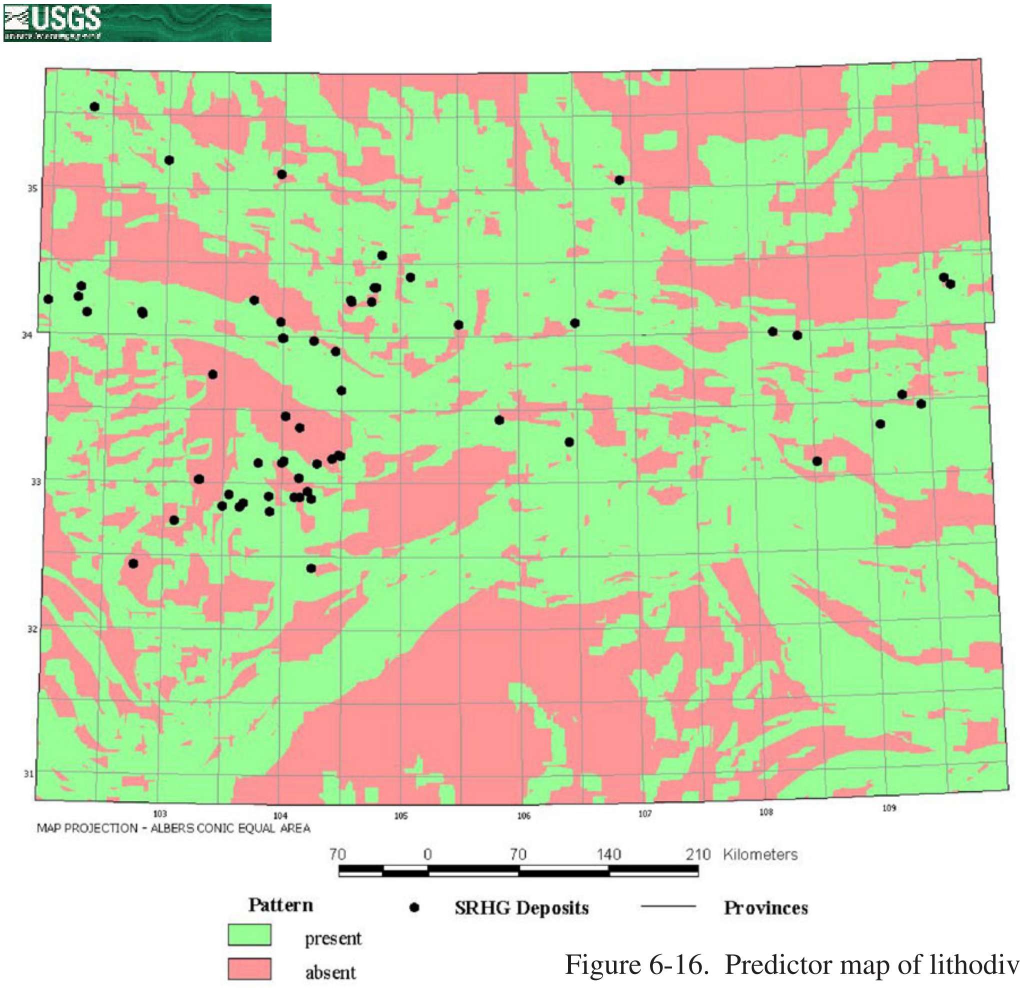

Figure 6-16. Predictor map of lithodiversity, Qinling area.

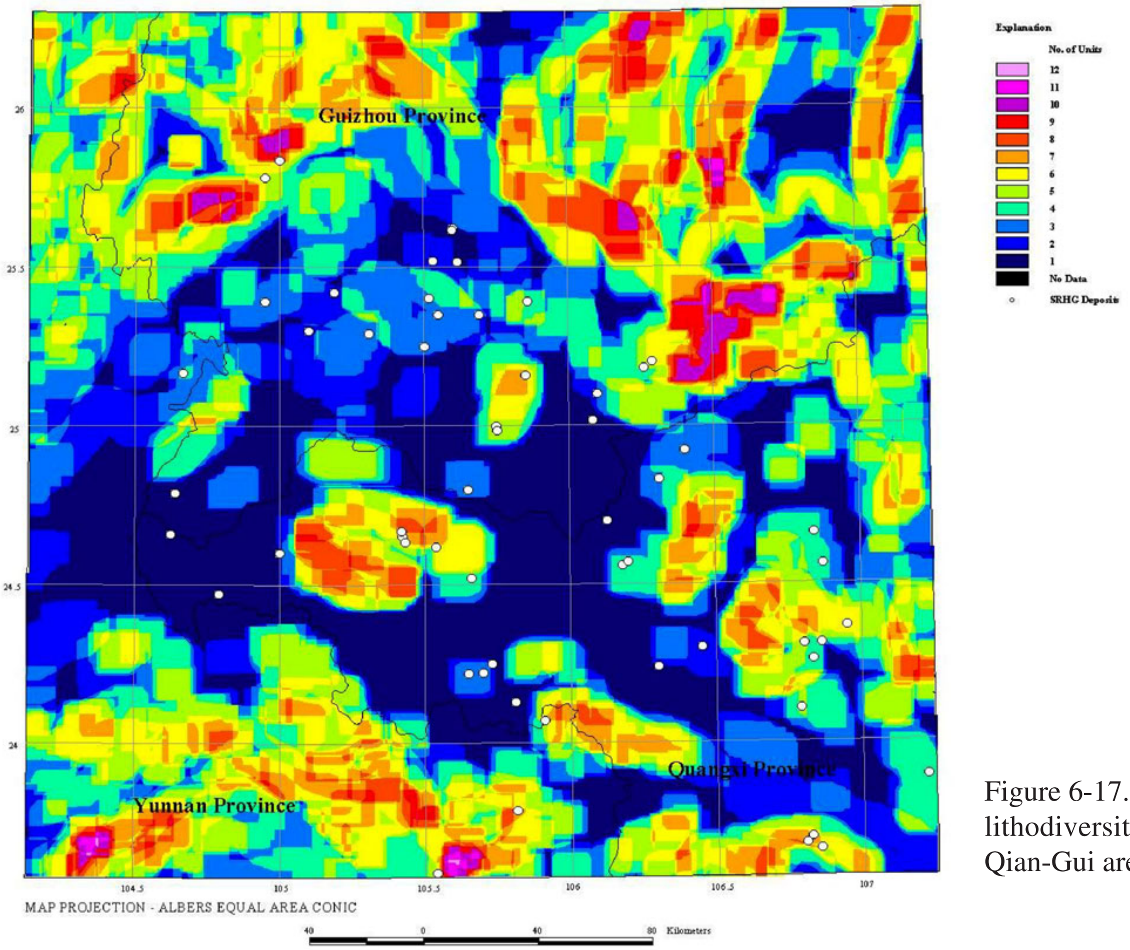

Figure 6-17. Map of lithodiversity, Dian-Qian-Gui area.

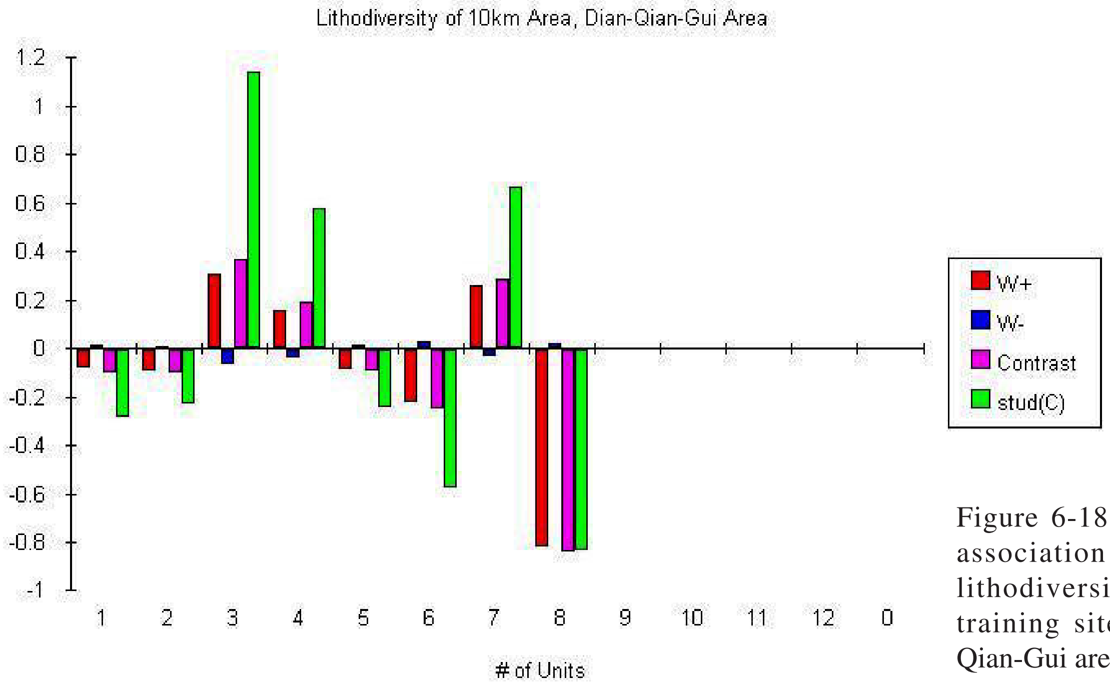

Figure 6-18: Spatial association between lithodiversity and training sites, Dian-Qian-Gui area.

The 10 km lithodiversity map for the Dian-Qian-Gui area is shown in figure 6-17. Except for the marked high in the middle of the area, there appears to be a strong trend of larger lithodiversity values toward the edges of the study area. Visual inspection of the map makes it difficult to determine if a positive spatial association between lithodiversity and training sites exists. The spatial association between the training sites and lithodiversity is shown in figure 6-18. As before, areas with a lithodiversity of 3 or more were classified as predictor map pattern present, and areas with a lithodiversity of 1-2 were classified as predictor map pattern absent. The lithodiversity predictor map constructed using these criteria is shown in figure 6-19.

Proximity to Geologic Contacts

The location of three important age boundaries were extracted from the geological map dataset and analyzed for spatial association with the training sites. These are the Devonian–Carboniferous (D-MP), Carboniferous–Permian (MP-P) and the Permian–Triassic (P-T). Li, Z.P. and Peters (1998) have documented that numerous SRHG deposits occur at the Permian–Triassic contact. Stratigraphic contacts represent sharp permeability, rock strength, and chemical gradients that provide controls on orebody location and shape (Li, Z.P. and Peters, 1998). After inspecting the geological maps, it was decided to extract and analyze the D-MP and MP-P contacts as well. Once extracted, the contacts were buffered at 2 km intervals.

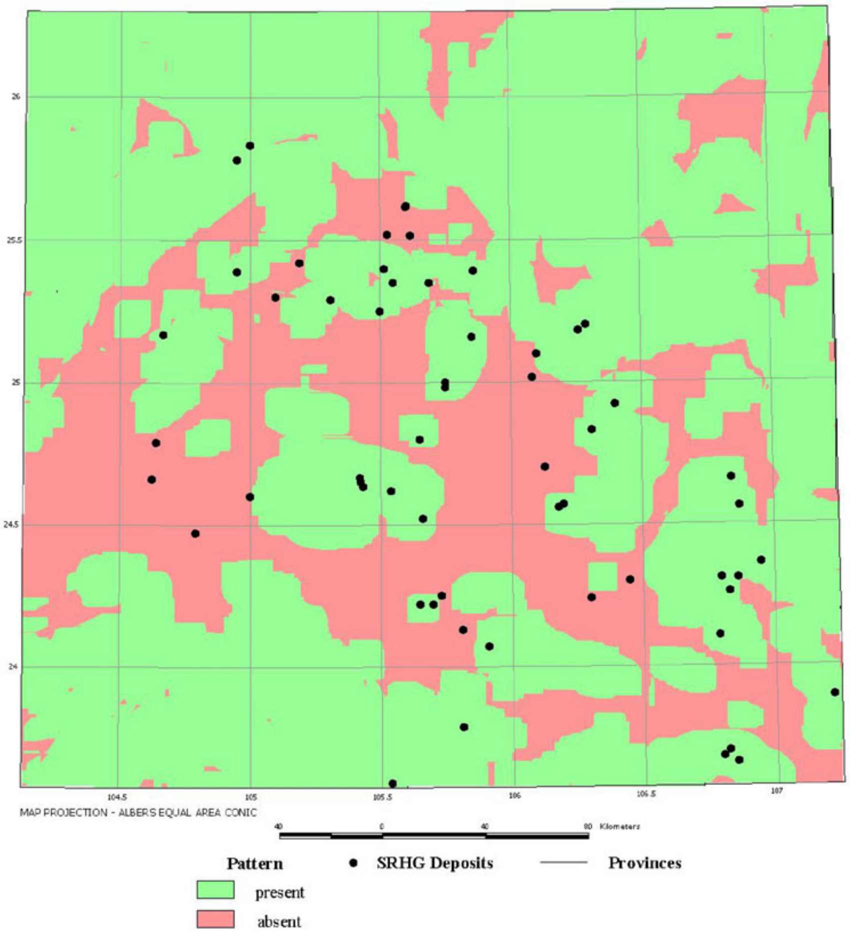

Figure 6-19. Predictor map of lithodiversity, Dian-Qian-Gui area.

In the Qinling study area, the Devonian–Carboniferous and the Permian–Triassic contacts showed a positive spatial association with training sites. The contacts were combined into a single Paleozoic–Mesozoic contact, and one map of proximity to the contact was created (fig. 6-20). Visual inspection of the contact proximity map shows a strong spatial association between the training sites and the contact, especially in the western part of the area. Weights for proximity to the contact is presented in figure 6-21. A proximity of 0 to 6 km was selected as the predictor map pattern, and was derived using a threshold defined by the highest W^+ value to the left of where W^+ and the inverse of W^- intersect. Note that for distances greater than 6 km, W^+ and the Studentized contrast begin to decline. The predictor map of proximity to the Paleozoic–Mesozoic contact is presented in figure 6-22.

Inspection of the three extracted contacts and training sites in the Dian-Qian-Gui study area revealed that only the Permian-Triassic contact had a positive spatial association with the training sites. The proximity map to this contact is shown in figure 23. Inspection of the map reveals the association between the P-T contact and training sites is indeed high. The graph of weights for contact proximity (fig. 6-24) reflects this in the steady decrease of W^+ as distance from the contact increases. A proximity of 0 to 2 km to the P-T contact was selected as the predictor map pattern (fig. 6-25).

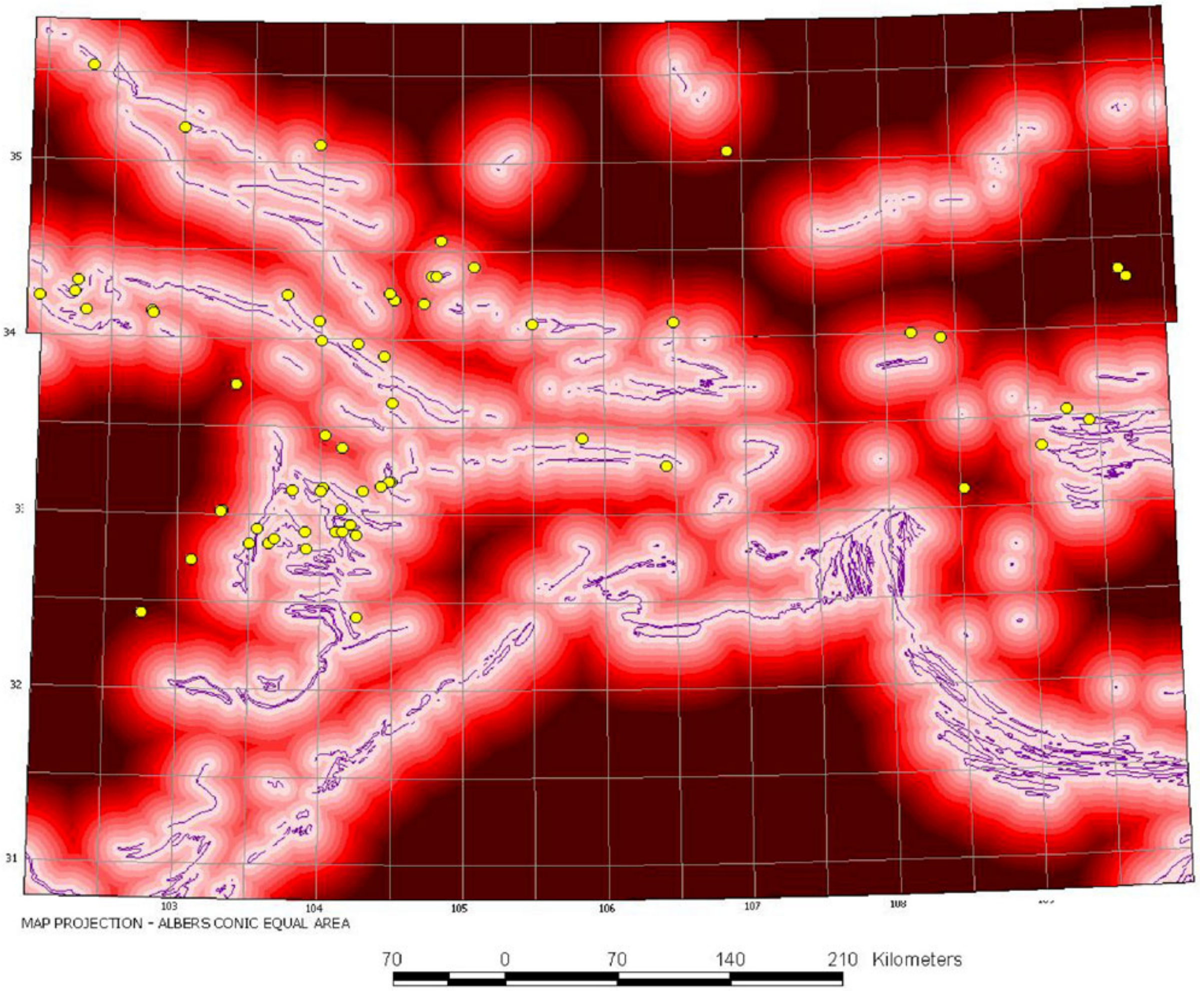

Figure 6-20. Proximity to Paleozoic-Mesozoic geologic unit contacts, Qinling area.

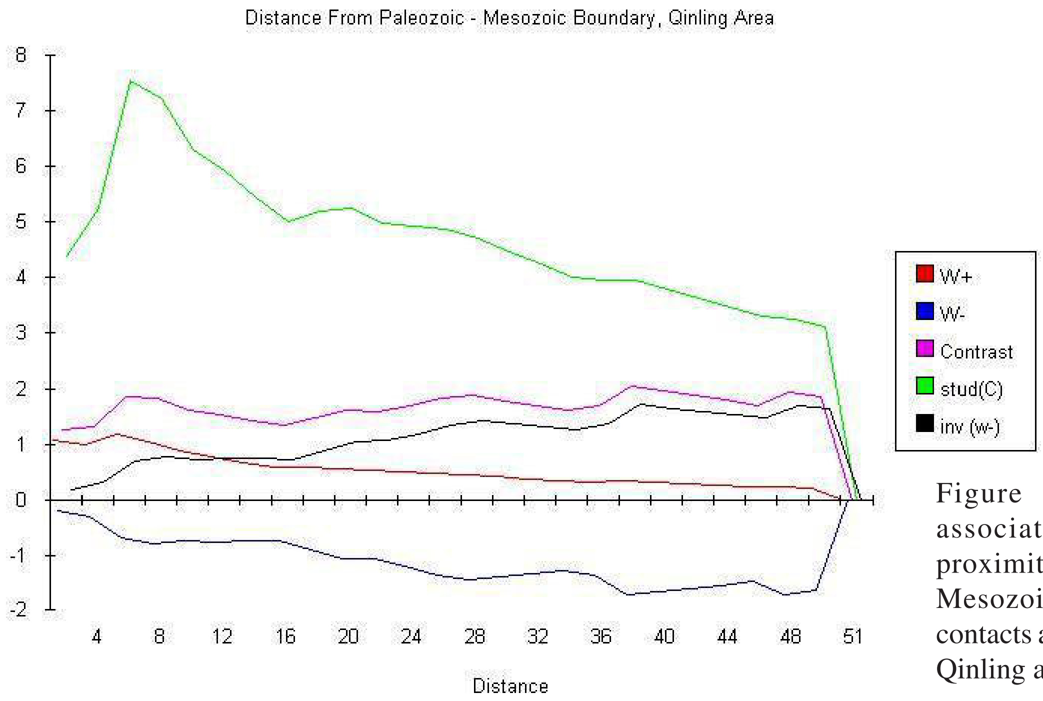

Figure 6-21. Spatial association between proximity to Paleozoic-Mesozoic geologic unit contacts and training sites, Qinling area.

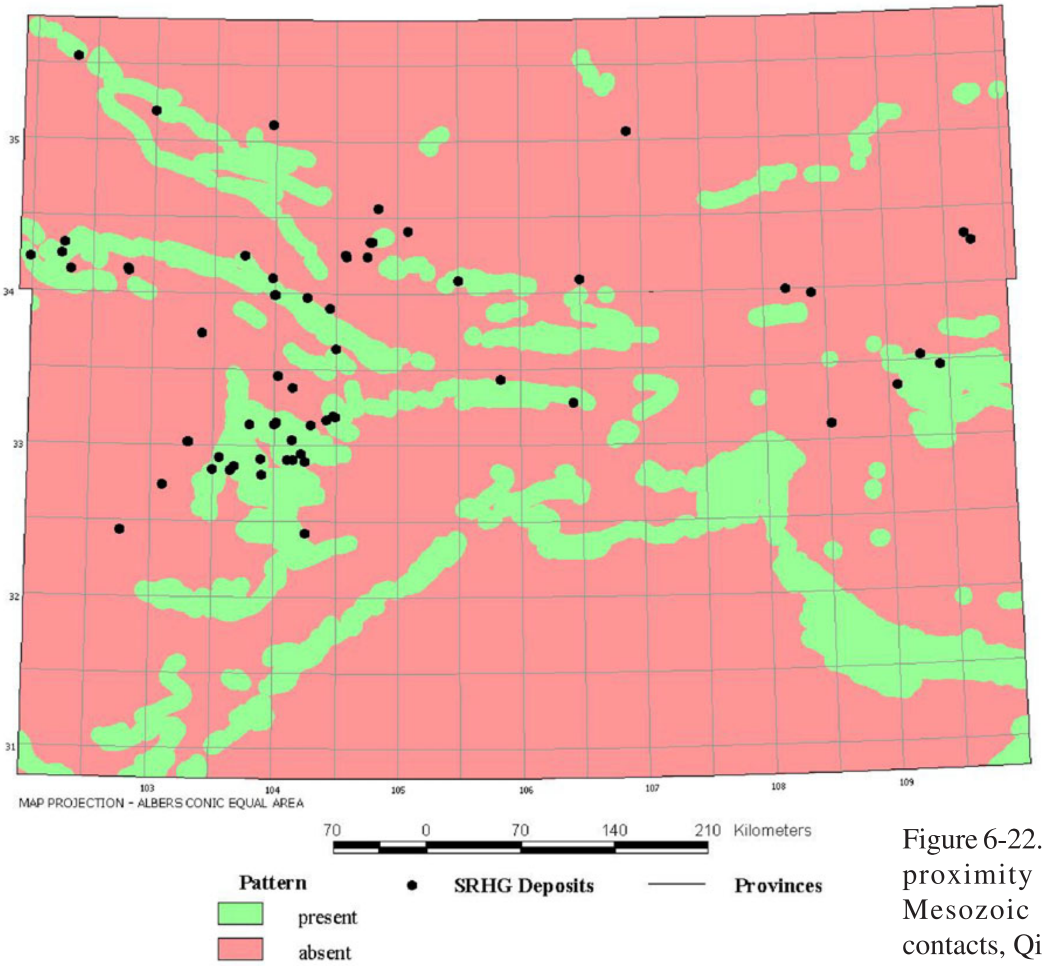

Figure 6-22. Predictor map for proximity to Paleozoic-Mesozoic geologic unit contacts, Qinling area.

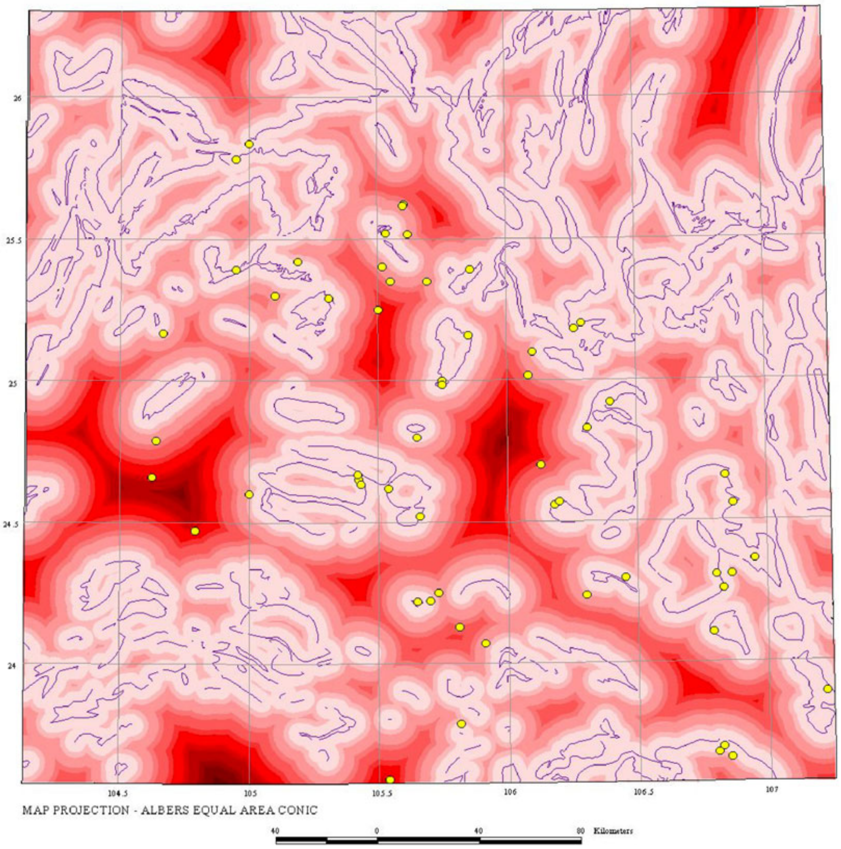

Figure 6-23. Proximity to Permian-Triassic geologic unit contacts, Dian-Qian-Gui area.

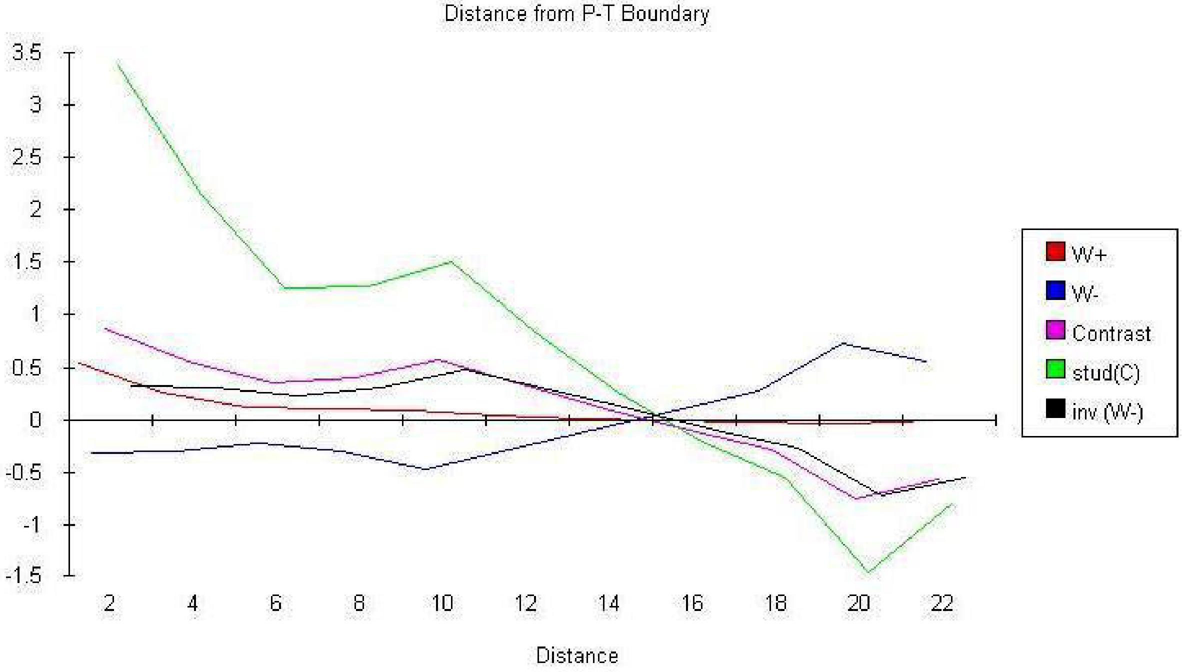

Figure 6-24. Spatial association between proximity to Permian-Triassic geologic unit contacts and training sites, Dian-Qian-Gui area.

Proximity to Faults

Fault traces accompanied both the GDS and USGS geologic map datasets. The GDS data were used as the primary data source, while the USGS data were used to augment the GDS data and fill in any gaps in coverage. Faults in Qinling and Dian-Qian-Gui are discussed in detail in Chapters 3 and 4. Recent fault scarps are portrayed in the processed topographic data (figs. 6-35 and 6-38).

Inspection of faults in the Qinling study area revealed that there was no particular fault orientation that was more correlated with the training sites than another. Therefore, all fault orientations were used in the analysis. The fault proximity evidence map is shown in figure 6-26. Visual inspection reveals that, in general, individual training sites and clusters of sites, particularly in the west, appear in close proximity to faults. The spatial association between training sites and proximity to faults is shown in figure 6-27. Positive spatial association is at a maximum within 2 km of the faults. This is reflected by the steady decrease of W^+ away from faults. The predictor map of fault proximity for the Qinling area is presented in figure 6-28.

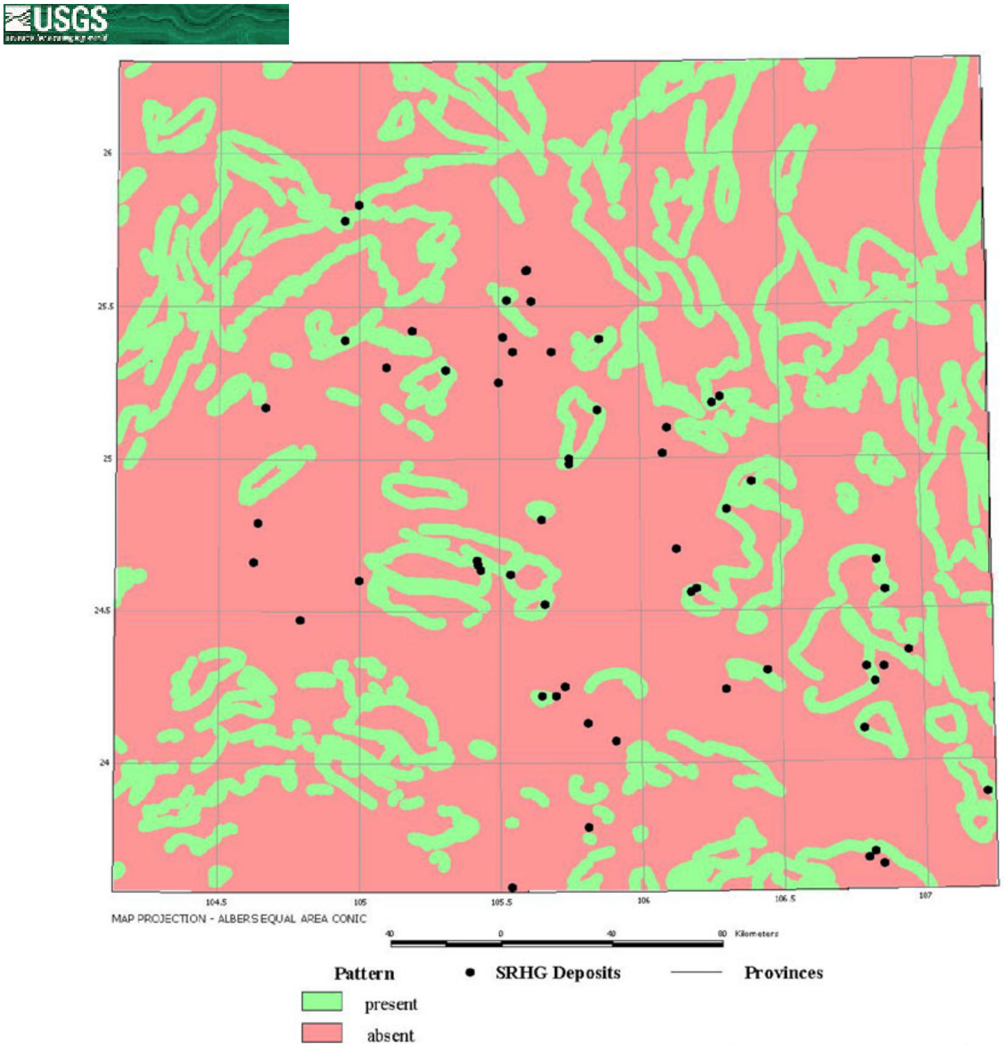

Figure 6-25. Predictor map for proximity to Permian-Triassic geologic unit contacts, Dian-Qian-Gui area.

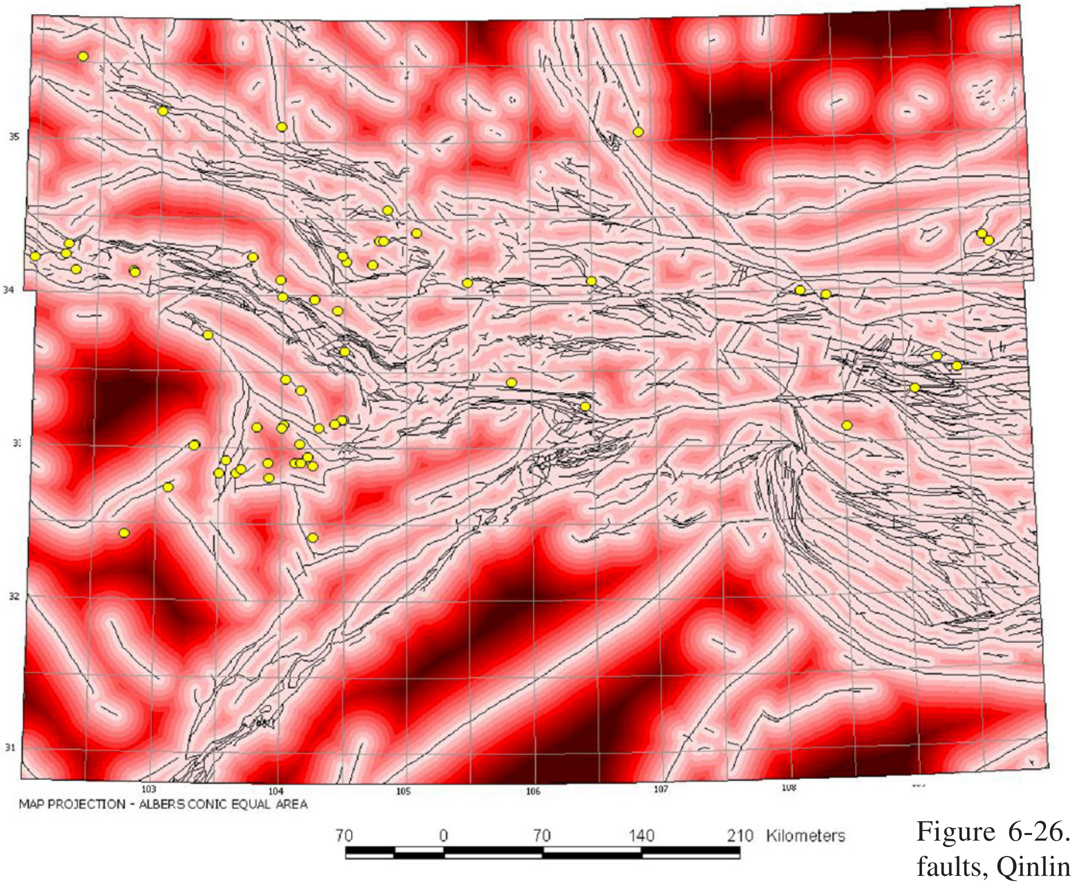

Figure 6-26. Proximity to faults, Qinling area.

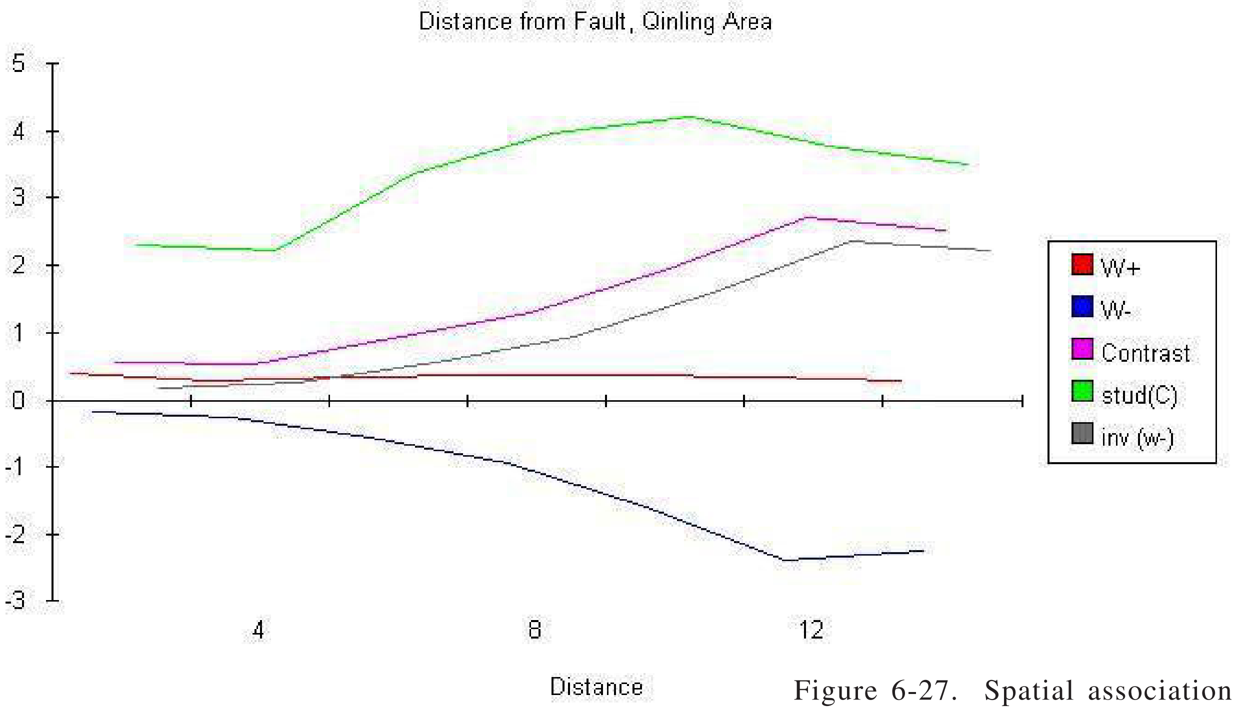

Figure 6-27. Spatial association between proximity to faults and training sites, Qinling area.

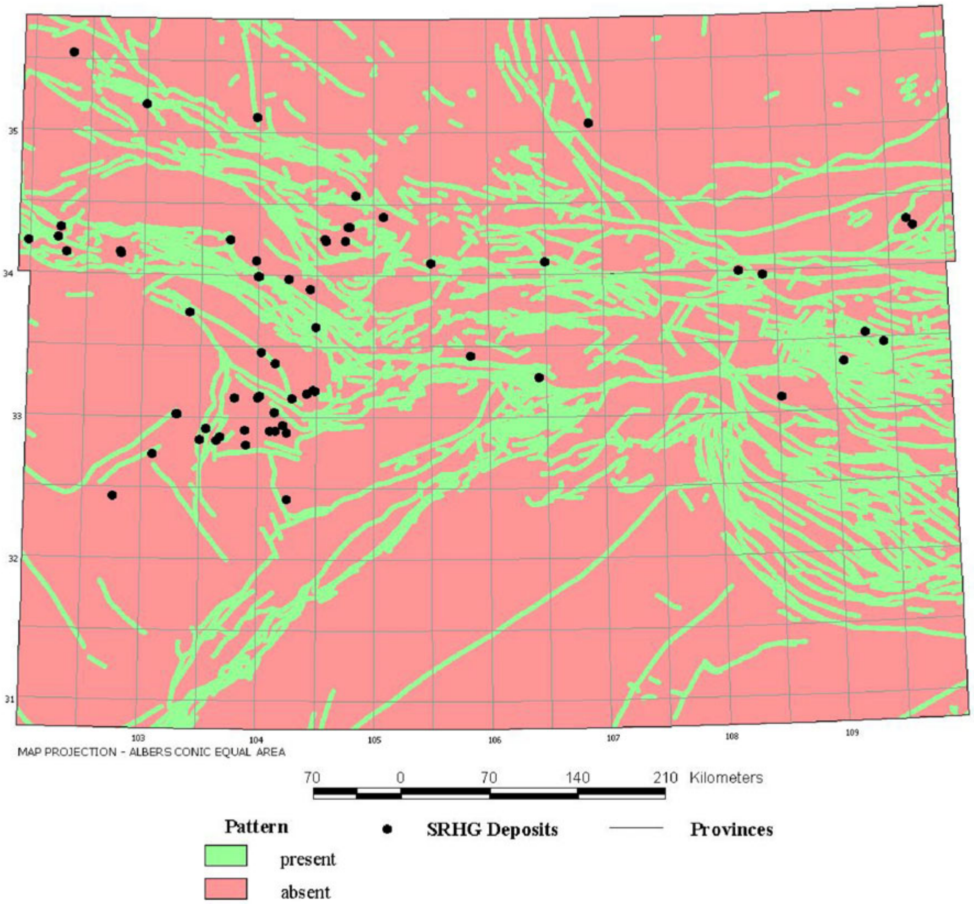

Figure 6-28. Predictor map for proximity to faults, Qinling area.

In the Dian-Qian-Gui area, a high correlation was found to exist between the training sites and faults with an east-northeast-orientation. This was determined by filtering the fault orientations by azimuth into six sets of 30^{o} each and performing WofE proximity analyses to determine which had the strongest spatial association with the training points. The fault proximity evidence map for these faults is shown in figure 6-29. The spatial association between the training sites and proximity to faults is presented in figure 6-30. Again, the value of W^+ is at a maximum within 2 km of the faults and decreases as distance away from the faults increases. The fault proximity predictor map is shown in Figure 6-31.

The Youjiang fault system also was used as evidence in the Dian-Qian-Gui study area. A spatial correlation between the distribution of SRHG deposits and this fault system has previously been suggested by Li, Z.P. and Peters (1998). Visual inspection reveals that more than half of the training sites occur within 50 km of the system. With this in mind, the fault system was buffered at the 2 km interval, but was carried out to 100 km instead of usual 50 km. The proximity to fault system evidence map is shown in figure 6-32. The spatial association between the training sites and proximity to the fault system is presented in figure 6-33. Inspection of the graph reveals that W^+ and the inverse of W^- cross at approximately 60 km. At a distance of 54 km, just prior to this crossover, W^+ reaches a maximum. The contrast and Studentized contrast support the interval of 0-54 km as a suitable predictor map pattern. The predictor map constructed from these criteria is shown in figure 6-34.

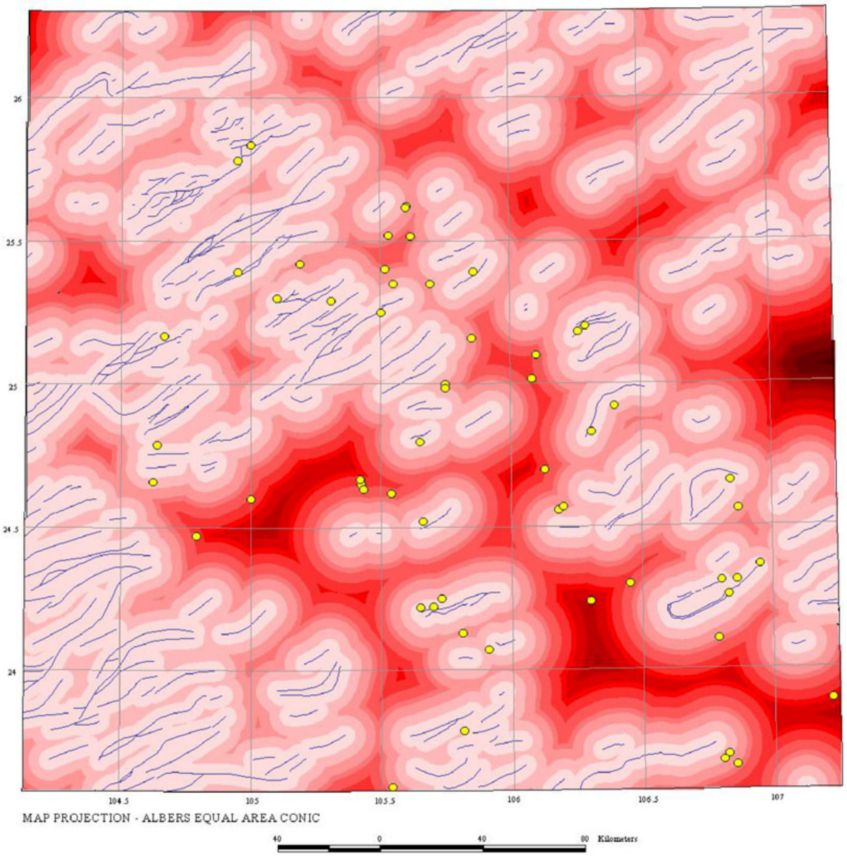

Figure 6-29. Proximity to ENE-trending faults, Dian-Qian-Gui area.

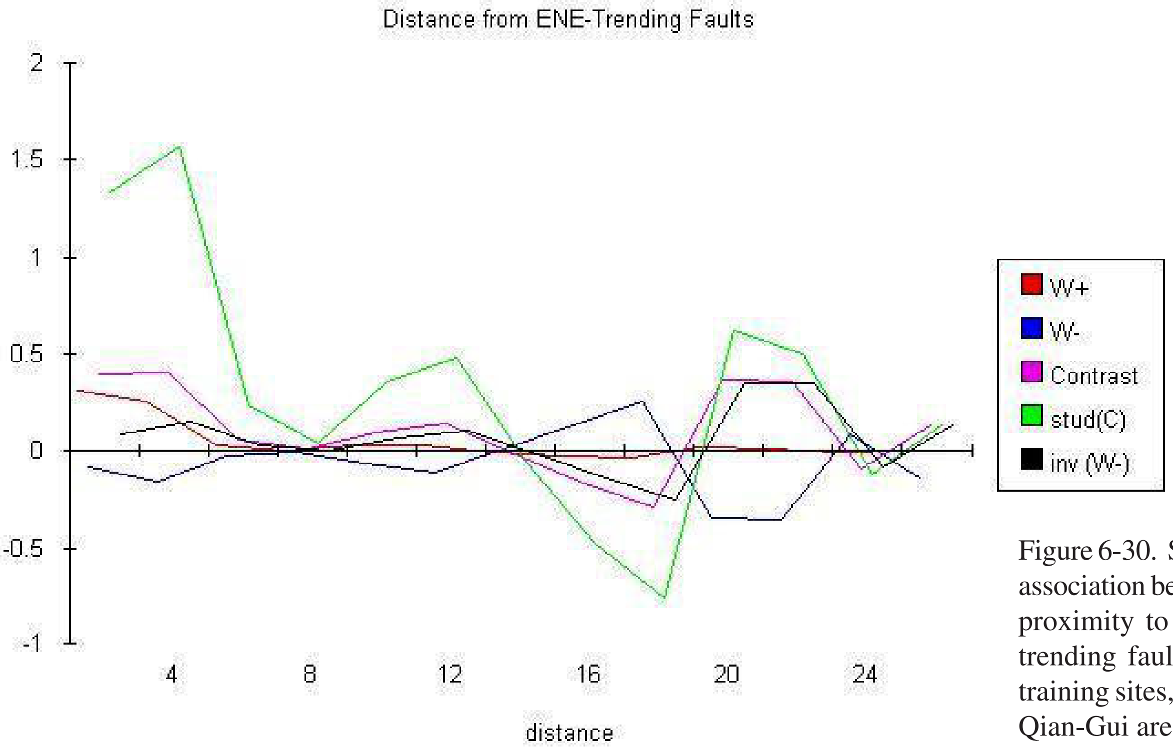

Figure 6-30. Spatial association between proximity to ENE-trending faults and training sites, Dian-Qian-Gui area.

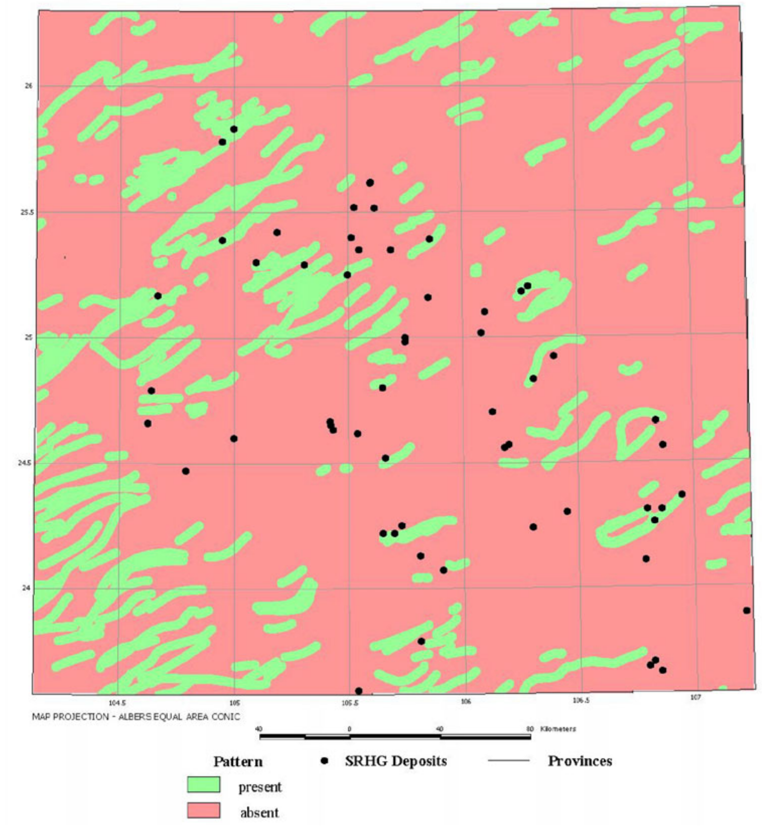

Figure 6-31. Predictor map of proximity to ENE-trending faults and training sites, Dian-Qian-Gui area.

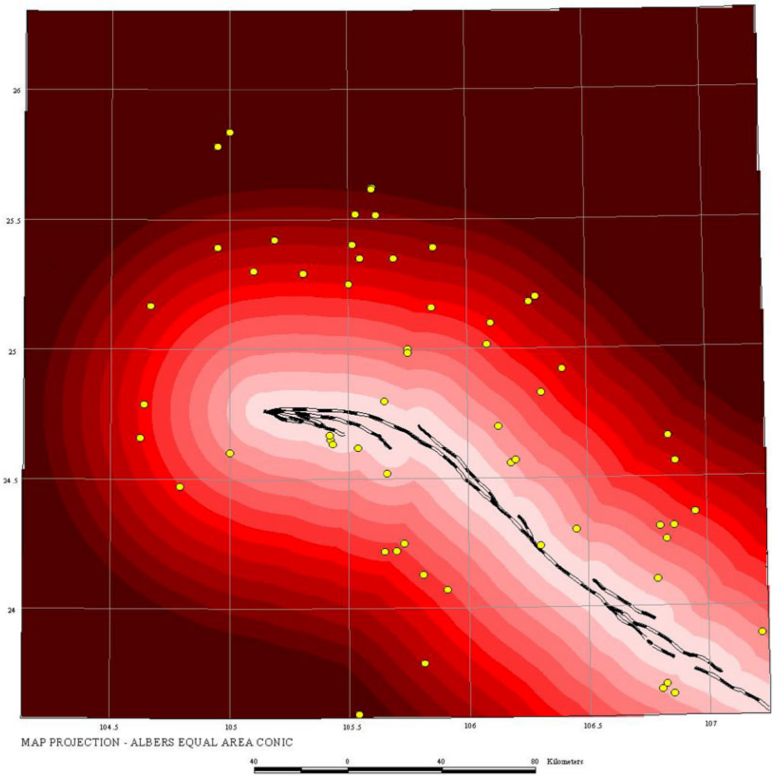

Figure 6-32. Proximity to the Youjiang Fault System, Dian-Qian-Gui.

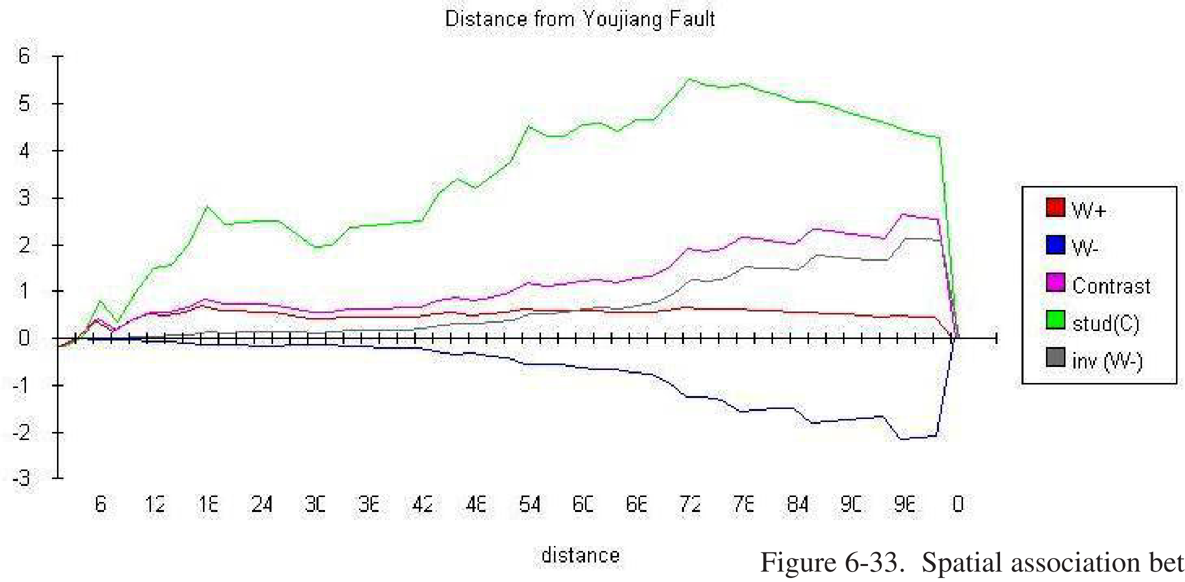

Figure 6-33. Spatial association between proximity to the Youjiang Fault System and training sites, Dian-Qian-Gui.

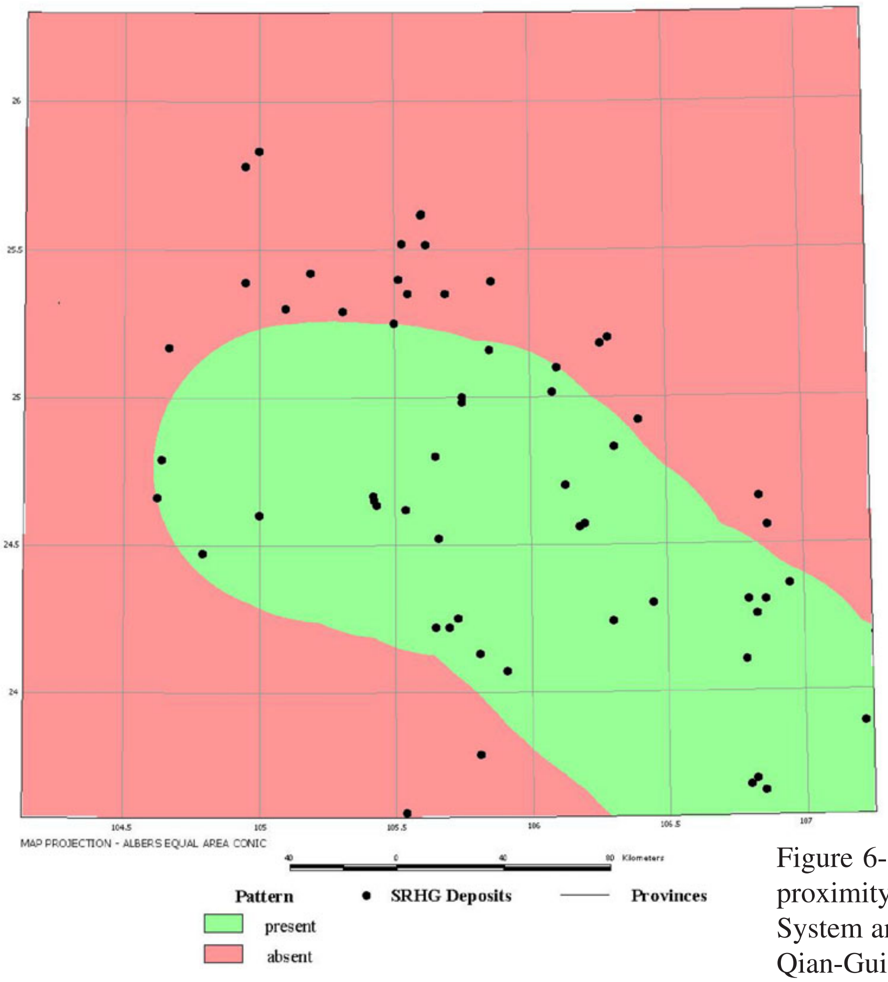

Figure 6-34. Predictor map for proximity to the Youjiang Fault System and training sites, Dian-Qian-Gui.

Topographic Slope

Maps of topographic slope were used as evidence in both the Qinling and Dian-Qian-Gui study areas. The rational for using slope as evidence is that abrupt breaks in slope may reflect the presence of unrecognized faults, or faults that are too small to be represented at the scales of the GDS and USGS geological maps. Slope maps were created from 30 arc-second digital elevation models (DEM) obtained from the USGS's EROS Data Center. The resolution of this data for the Qinling and Dian-Qian-Gui study areas is approximately 1 km. The preparation of this dataset for use in a GIS is detailed by Barto (2000). Once in the proper format, the slope was calculated using the ArcView function

"*derive slope*". This identifies the maximum rate of change in elevation, from each cell to its neighbors.

The slope evidence map for the Qinling area is shown in figure 6-35. Areas with the greatest change in slope appear in the southwestern and southeastern portions of Qinling. The spatial association between the training sites and slope is presented in figure 36. A slope of greater than 8˚ was selected as the predictor pattern. From inspection of the graph, values of 8˚ or higher have a positive W^+ and a high contrast and Studentized contrast. The predictor map of slope is shown in figure 6-37.

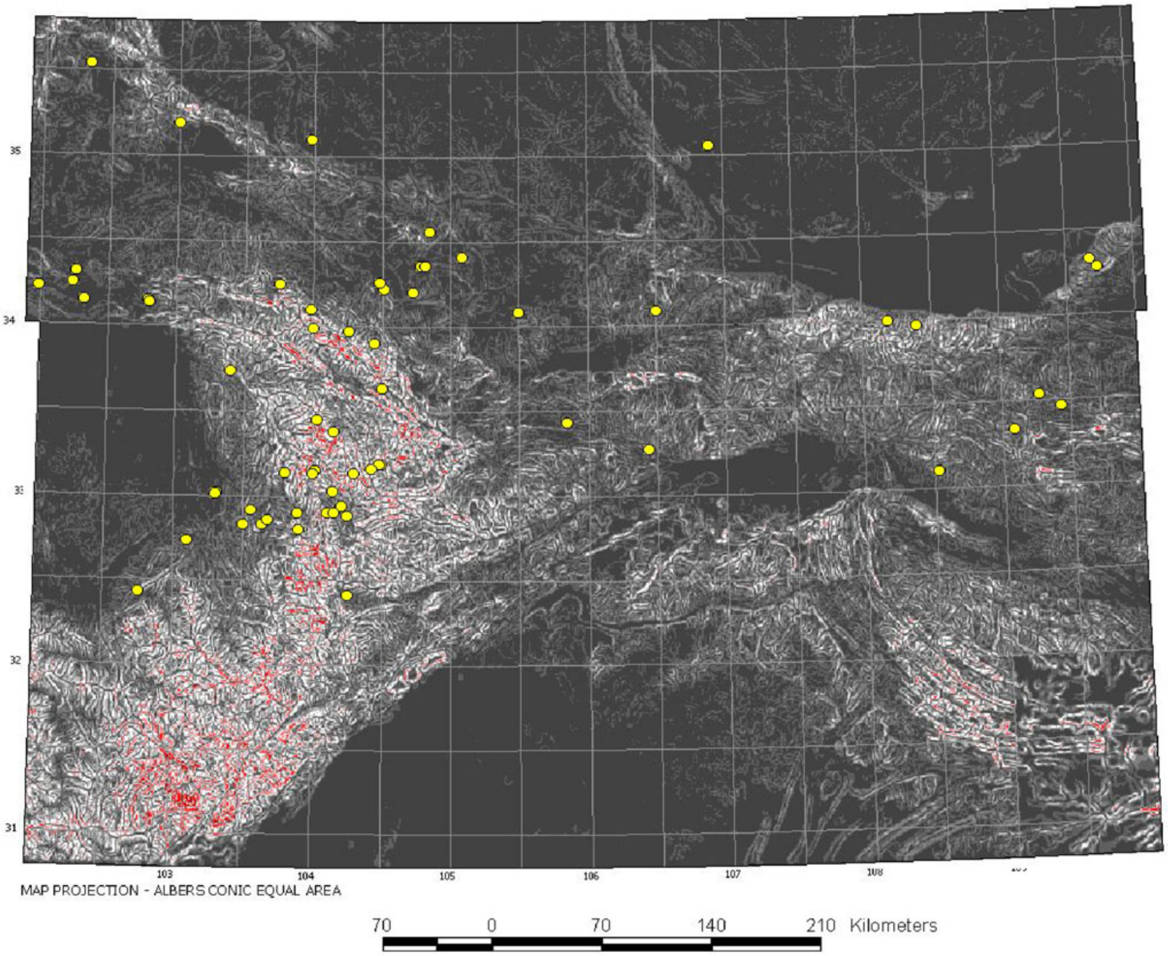

Figure 6-35. Topographic slope map, Qinling area.

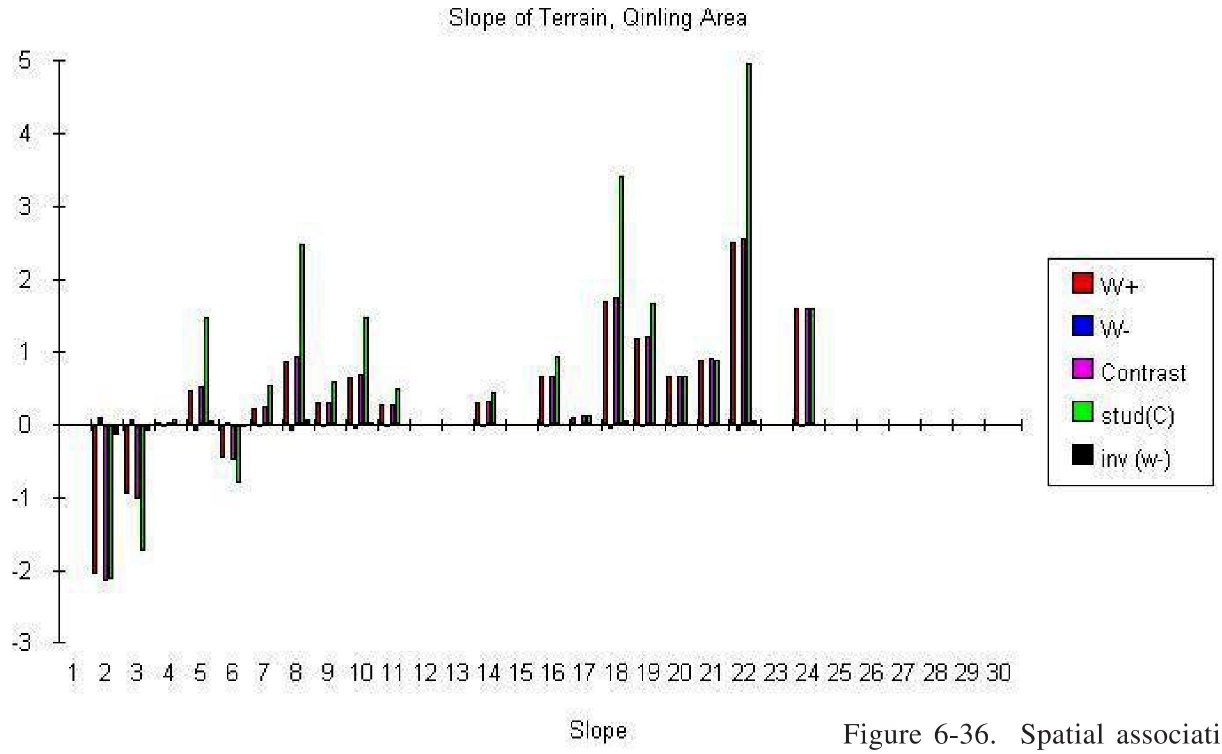

Figure 6-36. Spatial association between topographic slope and training sites, Qinling area.

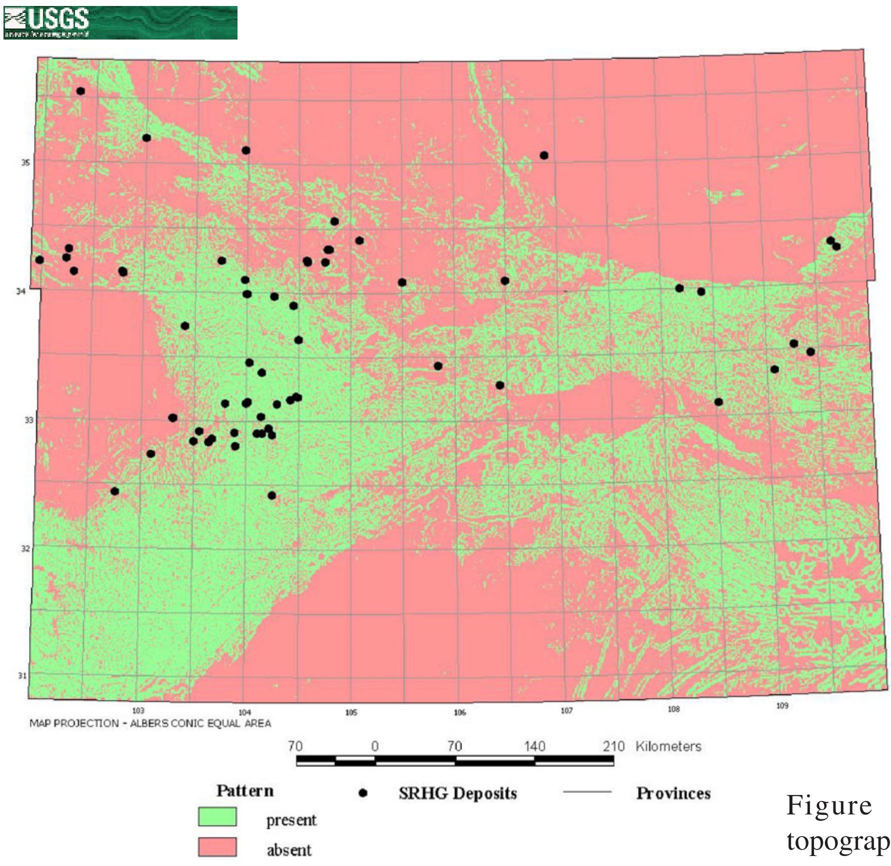

Figure 6-37. Predictor map of topographic slope, Qinling area.

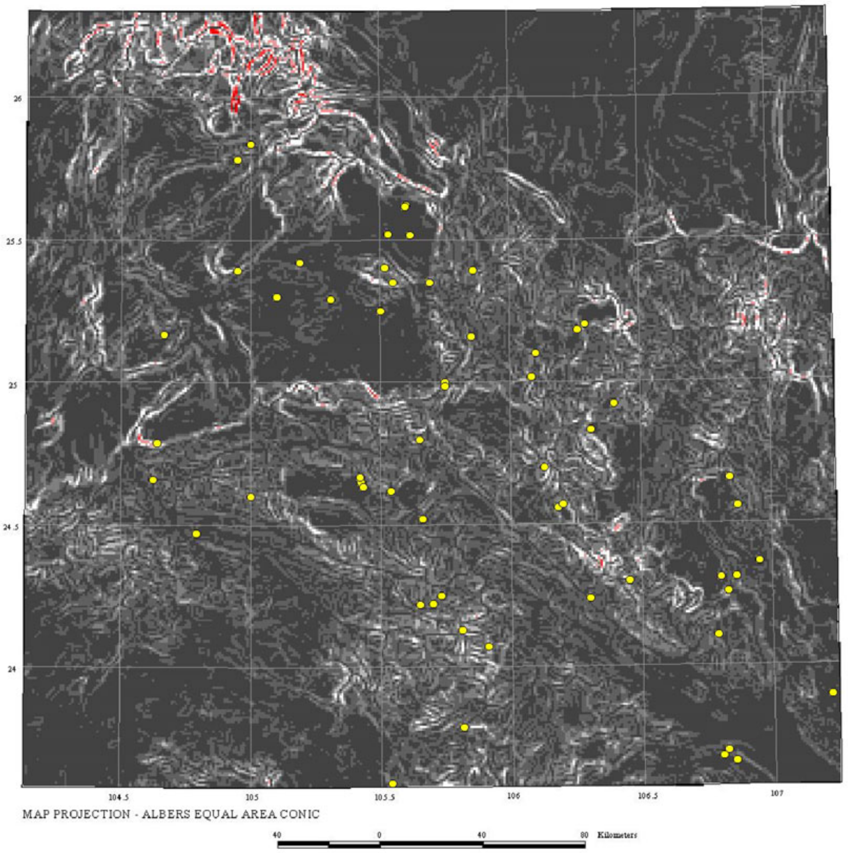

Figure 6-38. Topographic slope map, Dian-Qian-Gui area.

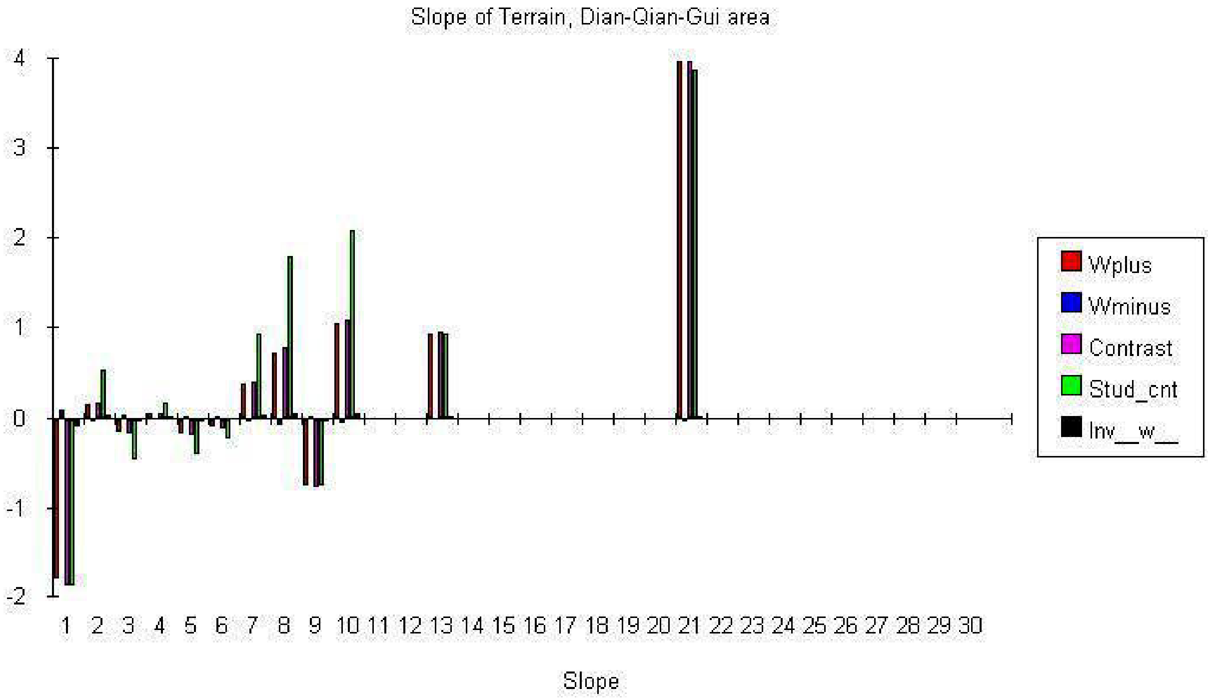

Figure 6-39. Spatial association between topographic slope and training sites, Dian-Qian-Gui area.

The slope evidence map for the Dian-Qian-Gui study area is shown in figure 6-38. The largest slope values appear in the northwestern portion of the study area. The spatial association between the training sites and slope is presented in figure 6-39. A slope of 7° or greater was selected as the predictor pattern. The reason for this is that the graph illustrates that at 7° and 8°, the values for W^+, contrast and Studentized contrast are all very good. At 9°, the spatial association drops, but this interval was overlooked in favor of including all values above 7° in the predictor pattern. The predictor map of slope is shown in figure 6-40.

Proximity to Anticlines

Anticline axial plane traces accompanied both the GDS and USGS geological map datasets. The datasets were used to augment each other and fill in any gaps in coverage. After visual inspection, it was determined that a correlation with training sites exists only in the Dian-Qian-Gui study area. Domal anticlines of Paleozoic rocks in the Dian-Qian-Gui area appear more significant in the WofE analysis because they contrast more sharply with surrounding and overlying Mesozoic rocks than do the more highly eroded complex folds in the Qinling fold belt.

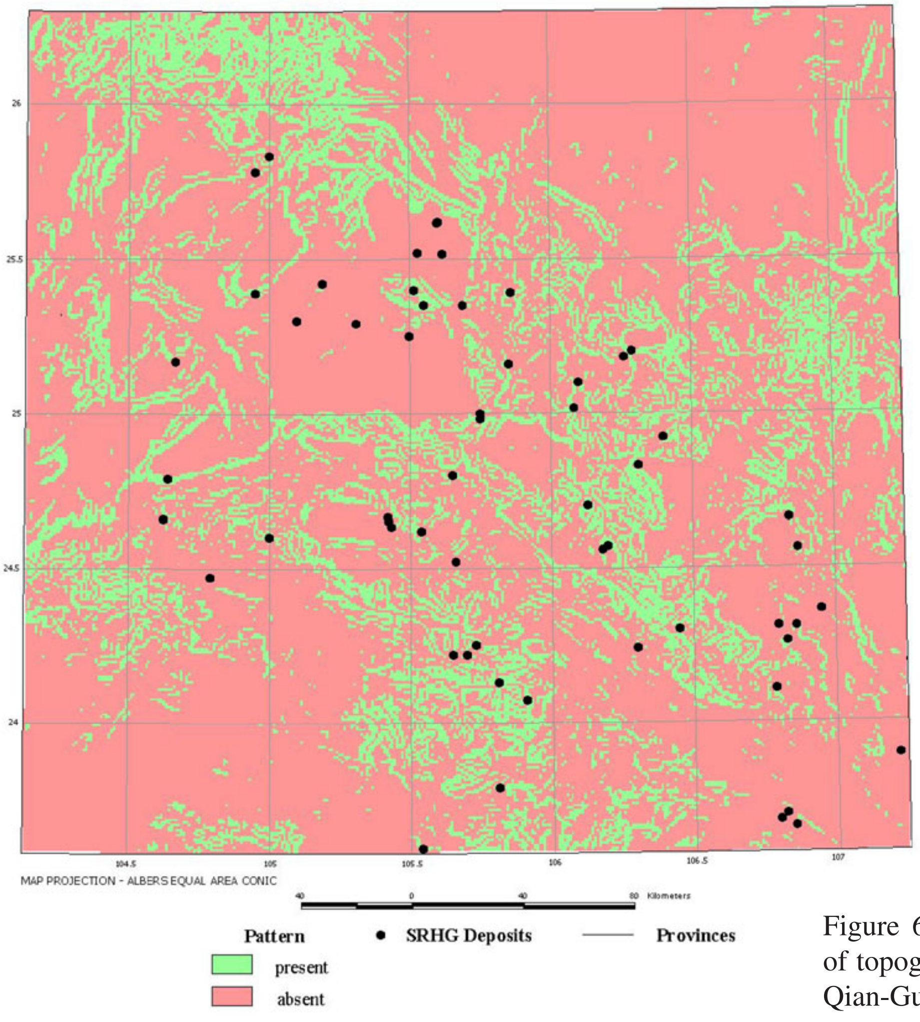

Figure 6-40. Predictor map of topographic slope, Dian-Qian-Gui area.

The evidence map of proximity to anticlines is shown in figure 6-41. Visual inspection reveals that many training sites are close to anticlines, whereas those that are not are located several kilometers away. The spatial association between the training sites and proximity to anticlines is presented in figure 6-42. Inspection of the graph reveals that spatial association declines rapidly as distance from anticlines increases. The highest spatial association exists at a distance of 0 to 2 km. The proximity to anticlines predictor map created from this spatial association is shown in figure 6-43.

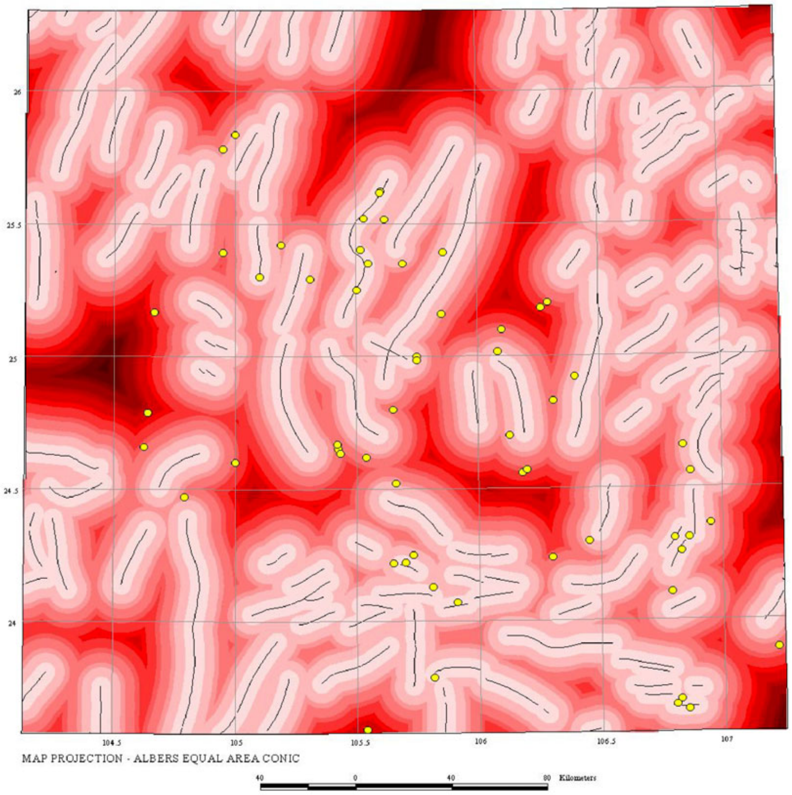

Figure 6-41. Proximity to anticline axes, Dian-Qian-Gui area.

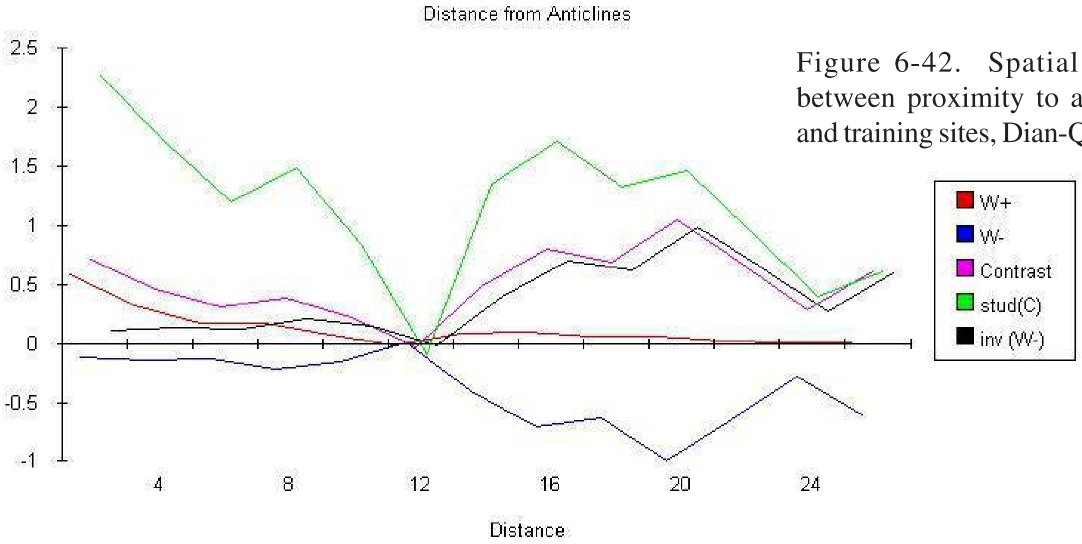

Figure 6-42. Spatial association between proximity to anticline axes and training sites, Dian-Qian-Gui area.

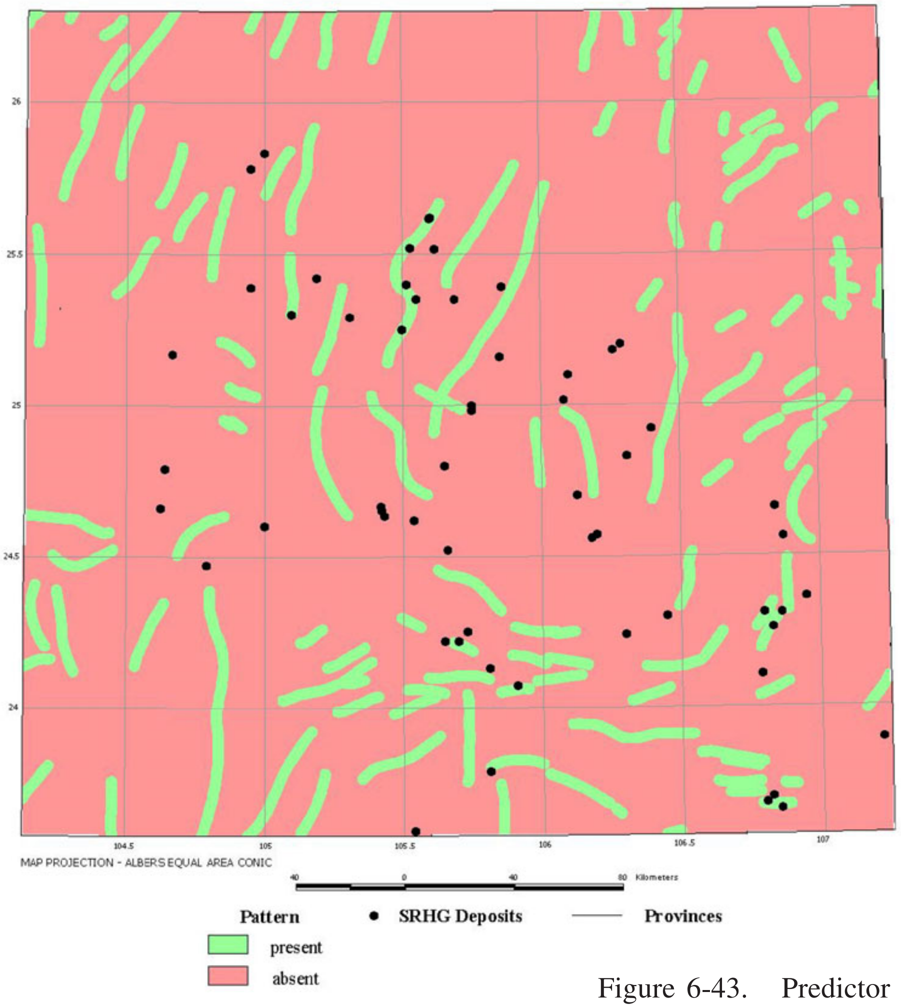

Figure 6-43. Predictor map of proximity to anticline axes, Dian-Qian-Gui area.

FAVORABILITY MAP GENERATION and ANALYSIS

The next step in modeling the distribution of SRHG sites is to combine the predictor maps to produce favorability maps. This is the third step of the modeling process (fig. 6-5). The Qinling and Dian-Qian-Gui study areas are discussed separately below, with an overall analysis and interpretation for each area following the selection of the "most acceptable" posterior probability model. In these applications, "most acceptable" refers to the model that exhibits the least amount of conditional dependency, thus allowing interpretations to be made with more assurance. The stepwise process is presented by illustrating several posterior"probability models for each study area in order to arrive at this "most acceptable" model.

Qinling Study Area

The prior favorability for the Qinling area is 0.0002. Five predictor maps were used for modeling:

- Geological Map Units
- Proximity to Paleozoic-Mesozoic Unit Contact
- Lithodiversity
- Proximity to Faults
- Topographic Slope

Model QA

The QA favorability map, created by combining all five predictor maps, is shown in Figure 6-44. Higher favorabilities are indicated by warmer colors, whereas lower values are represented by cooler tones. The weights of spatial association for each predictor map are presented in table 6-5. As indicated in the table, all predictor maps have confidence (Student-*t*) values above the desired 1.282. Further inspection shows that the lithodiversity and the Paleozoic-Mesozoic contact predictors have the greatest influence, as reflected by their high contrast values.

Predictor Layer	W+	W-	CONTRAST	CONFIDENCE
Geological Map Units	1.1712	-0.7489	1.9201	7.6937
P-M Contact	1.1721	-0.6862	1.8583	7.5407
Slope	0.4536	-1.2210	1.6747	4.6795
10 km Lithodiversity	0.2804	-0.7103	0.9907	3.2122
Fault Traces	0.4660	-0.2317	0.6977	2.8314

TABLE 6-5. Weights of spatial association for Model QA, Qinling area.

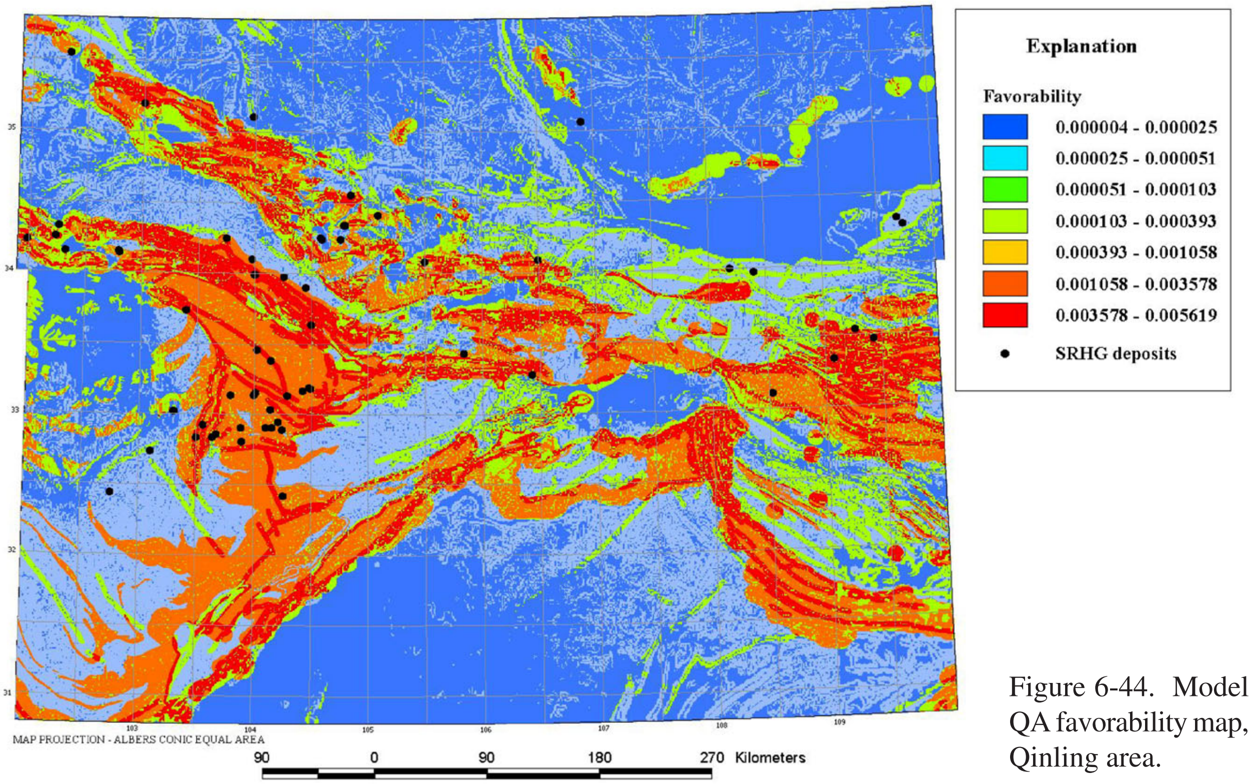

Figure 6-44. Model QA favorability map, Qinling area.

The overall test for CI yields a ratio of 0.43. This means that the model predicts 57 percent more training sites than observed. The CI ratio is below the desired range of <10 to 15 percent, which implies that there is a high degree of conditional dependency among the predictor maps. Chi-square testing of CI does not yield a similar result (table 6-6). Examination of the test results indicates that while conditional dependency exists between pairs, all are within the acceptable range of <5.4. The conclusion made as to the failure of the model in the overall test and passing of the chi-square test is that conditional independency is being violated due to multi-way combinations of predictor maps.

Predictor Layer	Geological Map Units	P-M Contact	Slope	10 km Lithodiversity
Fault Traces	0.01	0.06	0.05	0.05
Geological Map Units		2.01	2.30	0.11
P-M Contact			1.70	3.89
Slope				0.50

TABLE 6-6. Chi-square values for pairwise conditional independence testing of Model QA, Qinling area.

Model QB

After examining the predictor map weights and conditional dependencies for model QA (tables 6-5 and 6-6), the decision was made to eliminate the lithodiversity predictor map from the model due to its relatively low contrast and high χ^2 values with the proximity to Paleozoic–Mesozoic contact predictor map. The QB favorability map is shown in figure 6-45. Visual inspection reveals that the overall pattern is very similar to that of the QA favorability map (fig. 6-44), but the favorability values are not as high as those for the QA favorability map. The predictor map weights of spatial association (table 6-7) are the same as for model QA (table 6-5), except for the absence of the lithodiversity predictor.

Overall CI is 0.52, still well below the desired range. Chi-square testing (table 6-8) shows that conditional dependency does exist, but is still within acceptable limits.

Model QC

Upon inspection of the predictor map weights and conditional dependencies for model QB (tables 6-7 and 6-8), the decision was made to run the model after eliminating the slope predictor map due to its low contrast and large χ^2 value with the lithodiversity predictor map, the result of which is shown in figure 6-46. The QC favorability map is similar to the QA and QB favorability maps. Note, however, the lower favorabilities surrounding the faults, which is due to a decrease in contrast. The predictor map weights of spatial association are presented in table 6-9. The overall test for CI is 0.67. While much better than models QA, QB, and QC, it is still well below the desired range. The results of chi-square testing are presented in table 6-10. Once again, chi-square values are within the acceptable range.

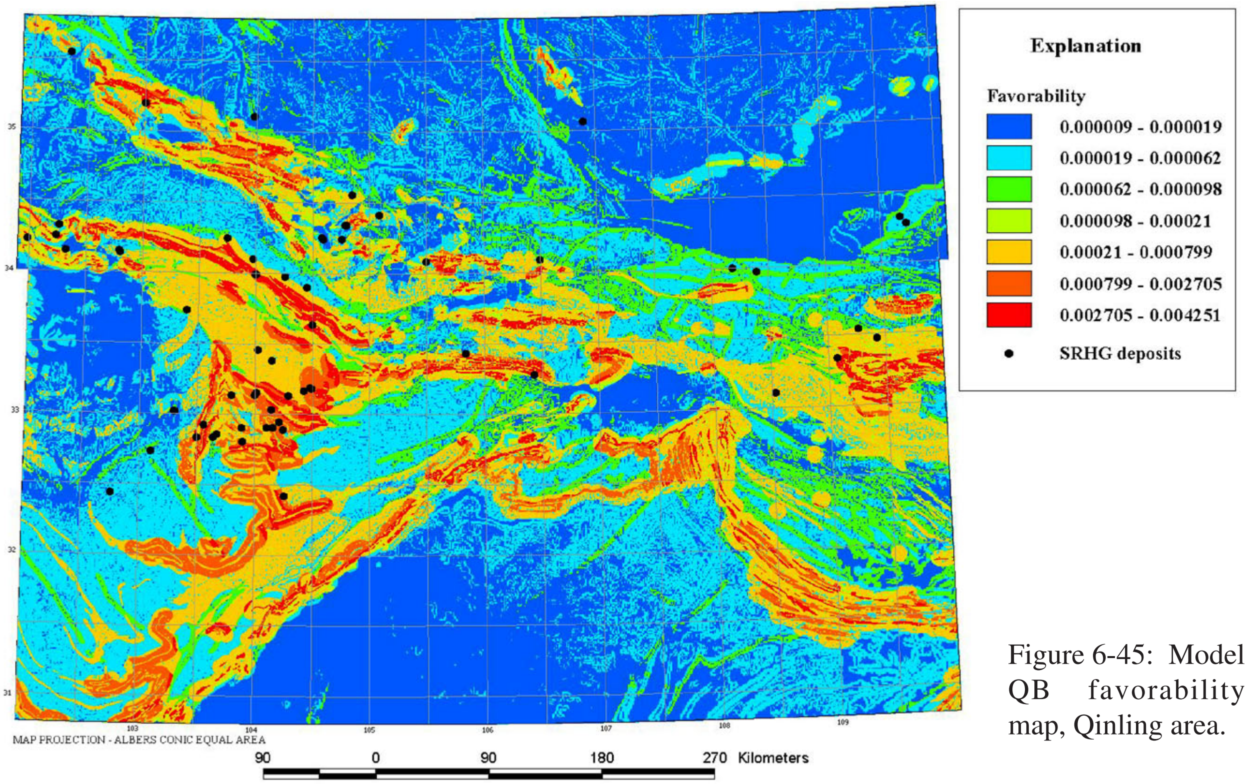

Figure 6-45: Model QB favorability map, Qinling area.

Predictor Layer	W+	W-	CONTRAST	CONFIDENCE
Geological Map Units	1.1712	-0.7489	1.9201	7.6937
P-M Contact	1.1721	-0.6862	1.8583	7.5407
Slope	0.4536	-1.2210	1.6747	4.6795
Fault Traces	0.4660	-0.2317	0.6977	2.8314

TABLE 6-7. Weights of spatial association for Model QB, Qinling area.

Predictor Layer	P-M contact	Geological Map Units	Fault Traces
Slope	1.70	2.30	0.05
P-M Contact		2.01	0.06
Geological Map Units			0.01

TABLE 6-8. Chi-square values for pairwise conditional independence testing of Model QB, Qinling area.

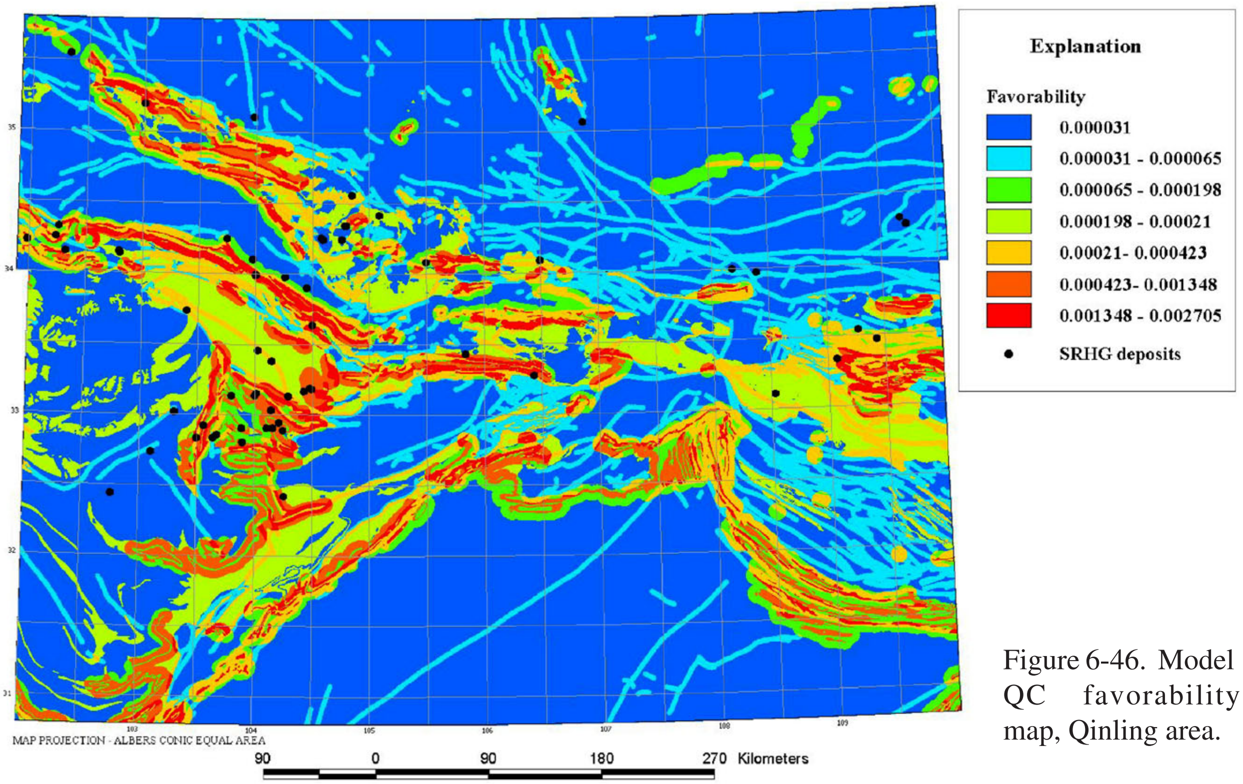

Figure 6-46. Model QC favorability map, Qinling area.

Predictor Layer	W+	W-	CONTRAST	CONFIDENCE
Geological Map Units	1.1712	-0.7489	1.9201	7.6937
P-M Contact	1.1721	-0.6862	1.8583	7.5407
Fault Traces	0.4660	-0.2317	0.6977	2.8314

TABLE 6-9. Weights of spatial association for Model QC, Qinling area.

Predictor Layer	Geological Map Units	P-M Contact
Fault Traces	0.01	0.06
Geological Map Units		2.01

TABLE 6-10. Chi-square values for pairwise conditional independence testing of Model QC, Qinling area.

Model QD

After consulting the predictor map weights and conditional dependencies for model QC (tables 6-9 and 6-10), the decision was made to combine the lithodiversity and proximity to Paleozoic-Mesozoic contact predictor patterns (fig. 6-47). Even though their chi-square value was below 5.4, it was the highest of all the predictor map pairs. The QD favorability map is shown in figure 6-48. The predictor map weights of spatial association are shown in table 6-11. The confidence and Studentized contrast values are very good, as are the weights. The overall CI is 0.75. While still below the desired amount, this is by far the most acceptable of the four Qinling study area models. Results of the chi-square test are presented in table 6-12. Despite combining the lithodiversity and proximity to Paleozoic-Mesozoic contact predictor patterns, it still failed the Chi-square test with topographic slope. They have a χ^2 value of 5.49, above the cut-off of 5.4.

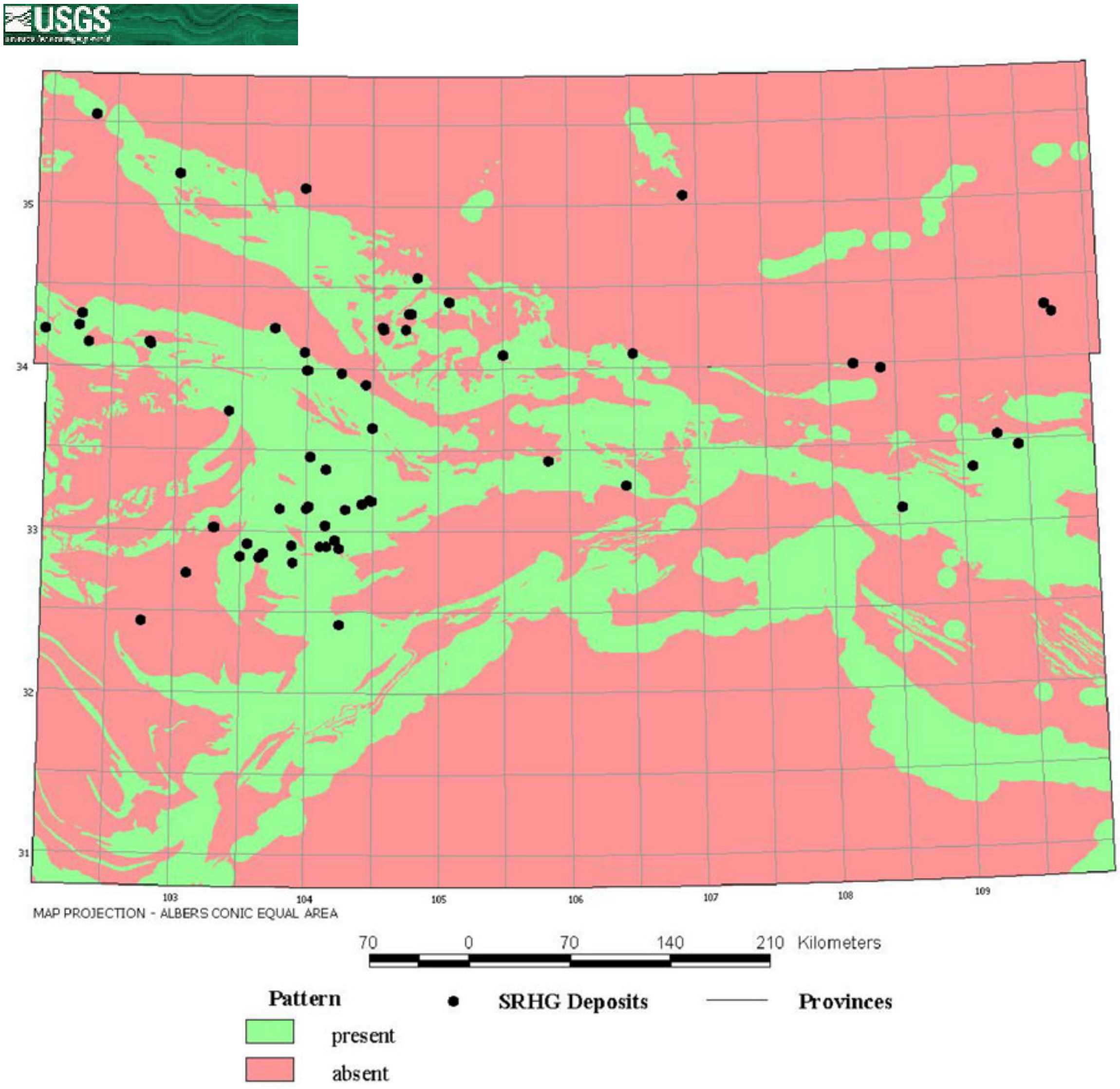

Figure 6-47. Predictor map of merged geological map units and proximity to Paleozoic-Mesozoic geologic unit contacts, Qinling area.

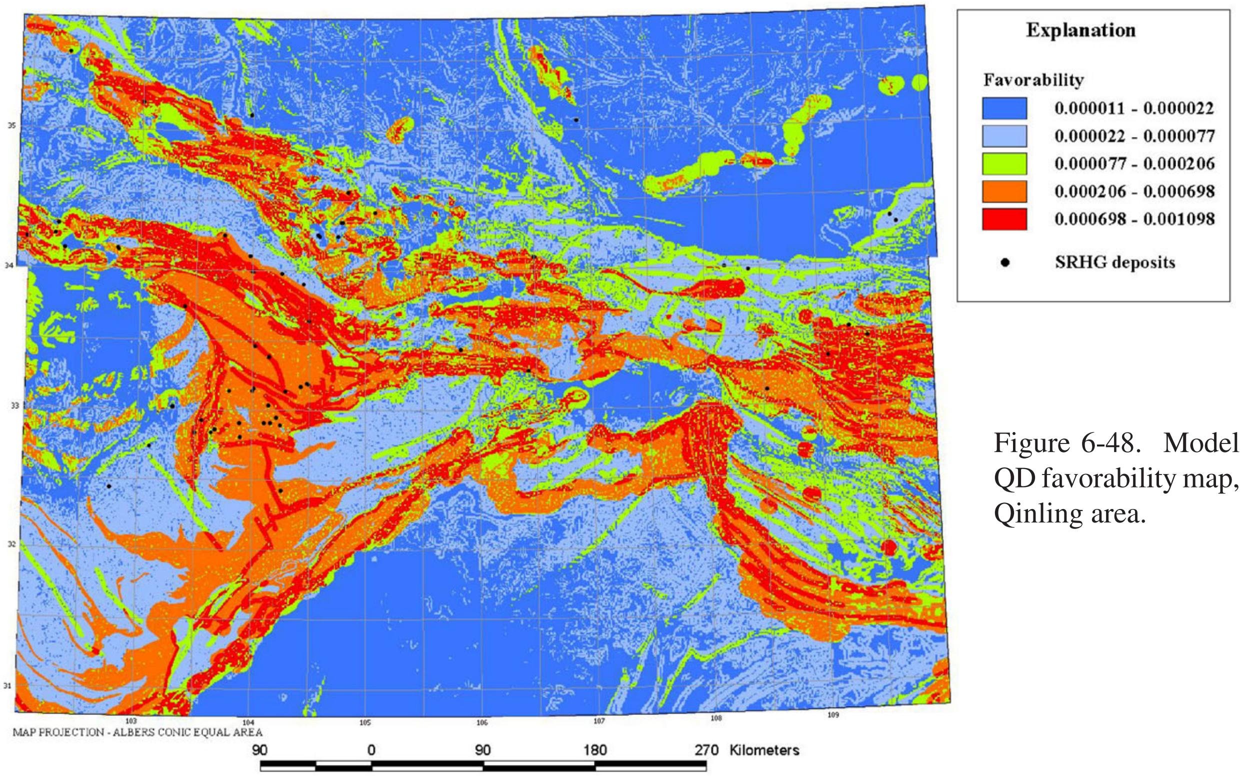

Figure 6-48. Model QD favorability map, Qinling area.

Predictor Layer	W+	W-	CONTRAST	CONFIDENCE
Geological Map Units/P-M Contact	0.9866	-1.2294	2.2160	7.3884
Slope	0.4536	-1.2210	1.6747	4.6795
Fault Traces	0.4660	-0.2317	0.6977	2.8314

TABLE 6-11. Weights of spatial association for Model QD, Qinling area.

Predictor Layer	Fault Traces	Geological Map Units/P-M contact
Slope	0.05	5.49
Fault Traces		0.59

TABLE 6-12. Chi-square values for pairwise conditional independence testing of Model QD, Qinling area.

Analysis of Qinling Study Area Models

Model QC (fig. 6-46) is considered most suitable for performing analysis and interpretation. Although its overall CI value was below the desired value of >0.85, chi-square testing, as well as its predictor map weights, Model QC represents the most acceptable compromise of the four models. Due to the fact that CI does exist among the predictor maps, the probabilities should be viewed only as favorabilities. This is due to the fact that it is not possible to determine the exact difference between a probability of, say, 0.0004 and 0.0006, but only that one (0.0006) is greater than the other (0.0004).

The map of total uncertainty for the QC favorability map is shown in Figure 6-49. The pattern of total uncertainty is similar to that of the favorability map due to the fact that data coverage for each map was complete across the region, therefore, most of the uncertainty is due to variances in weight estimates. The relative certainty to which the favorabilities can be interpreted is a reflection of their t-values. From table 6-9, it is seen that the confidence of the predictor maps is relatively high; consequently, the favorabilities can be evaluated with relatively high degree of confidence.

Interpretation of Qinling Study Area Models

Although the QC favorability map failed the overall test for CI, it is still very useful for delineating regional-scale exploration targets. The relative influence of the predictor maps for model QC, in order from most to least important, is as follows: geological map units, proximity to Paleozoic-Mesozoic contact, and proximity to faults.

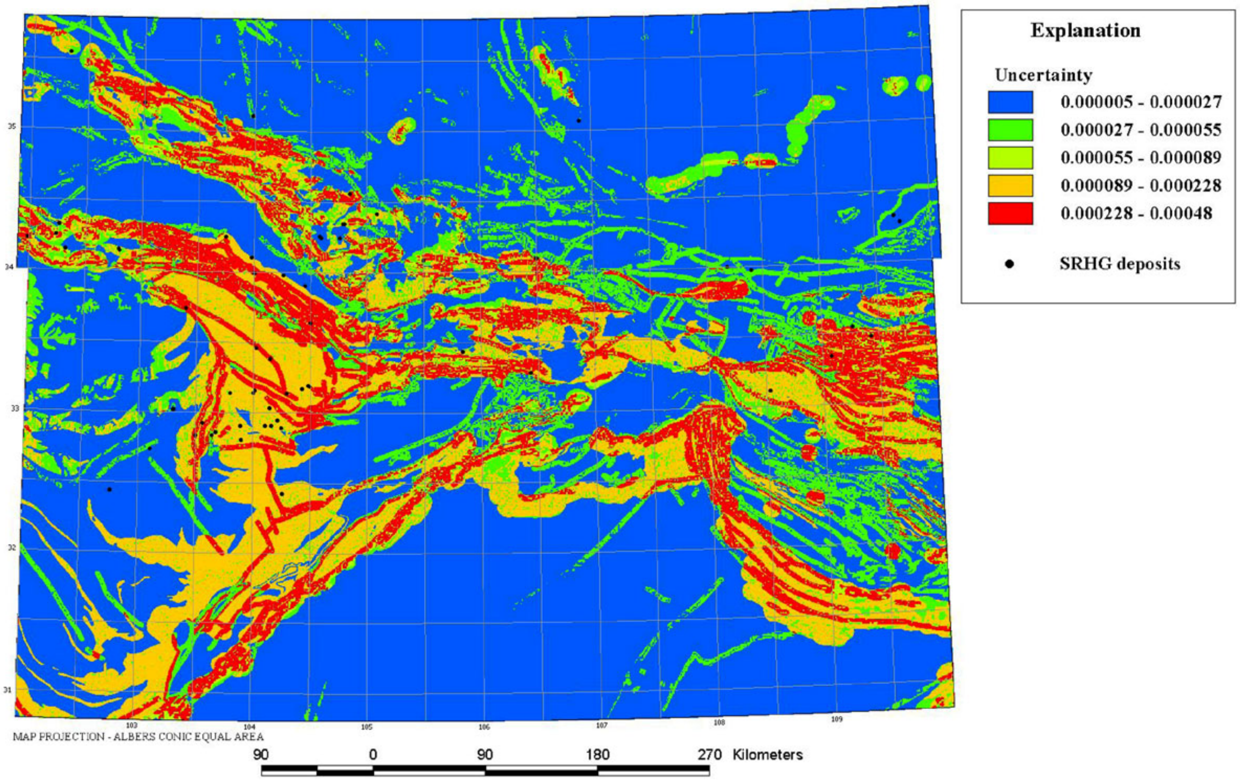

Figure 6-49. Model QC total uncertainty map, Qinling area.

To aid in interpreting the QC favorability map, areas with favorabilities less than or equal to the prior were masked out. To further aid in the analysis, a 5 km distance buffer was placed around the training sites with the assumption that these areas have been previously explored (fig. 6-50).

With these areas masked out, numerous exploration targets are apparent throughout the region (fig. 6-50). Three areas are of particular interest. The first area of interest is the southern extent of the Qinling fold belt (fig. 6-48). No known mineral sites are located in this area, yet the favorability is very high, stretching nearly 700 km from east to west. The second area of interest occurs in the east-central portion of the study area, and is marked by the large cluster of high favorabilities with only 3 training sites. This area of high probabilities is nearly 4,800 km^2. The third, but certainly not final, area of interest lies approximately between 103°-105° N longitudes and 34.5° to 33.5° E latitude. Though more than half a dozen training sites occur in this area, its large size and extent, along with very high favorabilities, makes it a worthwhile exploration target.

The models for the Qinling study area suggest that the regional-scale distribution of the SRHG mineral sites is primarily influenced by lithology, specifically carbonate rock units of Permian age.

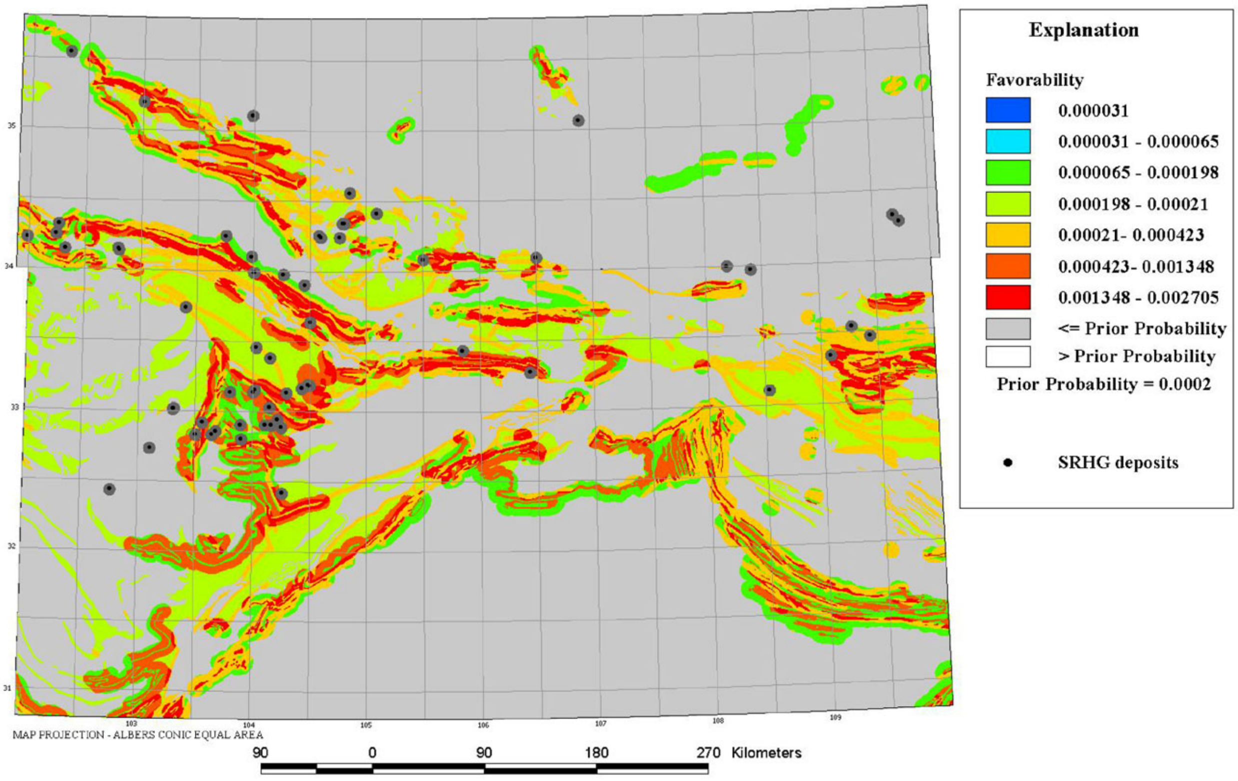

Figure 6-50. Favorability map of Model QC used for interpretation, Qinling area. Note that areas with favorabilities less than or equal to the prior have been masked out (light gray). Five km buffers have been placed around all training sites (dark gray around sites).

Dian-Qian-Gui Study Area

The prior favorability for the Dian-Qian-Gui study area is 0.0006, slightly higher than that of the Qinling area, mainly due to its smaller size compared to the number of training sites. Seven predictor maps were used for modeling:

- Geological Map Units
- Proximity to Permian-Triassic Unit Contact
- Lithodiversity
- Proximity to ENE-Trending Faults
- Proximity to the Youjiang Fault System
- Proximity to Anticlines
- Topographic Slope

Model DA

The DA favorability map, created by combining all seven predictor maps, is shown in figure 6-51. Warmer tones reflect higher favorabilities, while cooler tones reflect lower. The strong influence of the proximity to Youjiang fault system predictor map is visually apparent in the favorability map as an oblong shape, extending from the southeast to the central portion of the region. Note how areas within this region have elevated favorabilities compared to those outside. The weights of spatial association for each predictor map are presented in table 6-13. Visual inspection reveals that all of the predictor maps have relatively good values, except for lithodiversity. This predictor map has a confidence below the cut-off of 1.282. Therefore, this map should be omitted from the model. Overall CI is 0.99, well above the desired 0.85. However, the results of chi-square testing (table 6-14) are not as good. A very large χ^2 value of 17.41 is observed for the geological and the proximity to Permian-Triassic unit contact predictor maps. The conditional dependency was mitigated by combining the geological and Permian-Triassic contact predictor maps, referred to as the “lithoPT” predictor map (fig. 6-52).

Model DB

For the DB favorability map, the lithodiversity predictor map was eliminated from the model, and the geological and the proximity to Permian-Triassic unit contact predictor maps were combined and treated as a single predictor pattern (fig. 6-53). The weights of spatial association for each predictor map are presented in table 6-15. The predictor maps have confidence values above 1.282 and high contrast values. Overall CI for the model is 1.03, reflecting an *under prediction* of training sites by 3 percent. Inspection of the chi-square table (table 6-16) reveals that all values are below the desired 5.4.

Model DC

Although Model DB passes all tests for CI, and the predictor maps have high weights values, a third favorability maps was created where the proximity to Youjiang fault system was eliminated (fig. 6-54). This is done to better understand the impact that proximity to the Youjiang fault system has on modeling. The effect of eliminating the proximity to the Youjiang fault system predictor map from the model is that there is more of a balance of high values throughout the favorability map. Areas that fell within the Youjiang fault system are no longer slightly higher than those outside. The predictor map weights for model DC (table 6-17) show high W^+ and contrast values. The overall CI is 0.99, reflecting only a 1 percent under estimation of training sites. The test of chi-square CI (table 6-18) indicates that none of the predictor map combinations fall outside of the acceptable cut-off of 5.4.

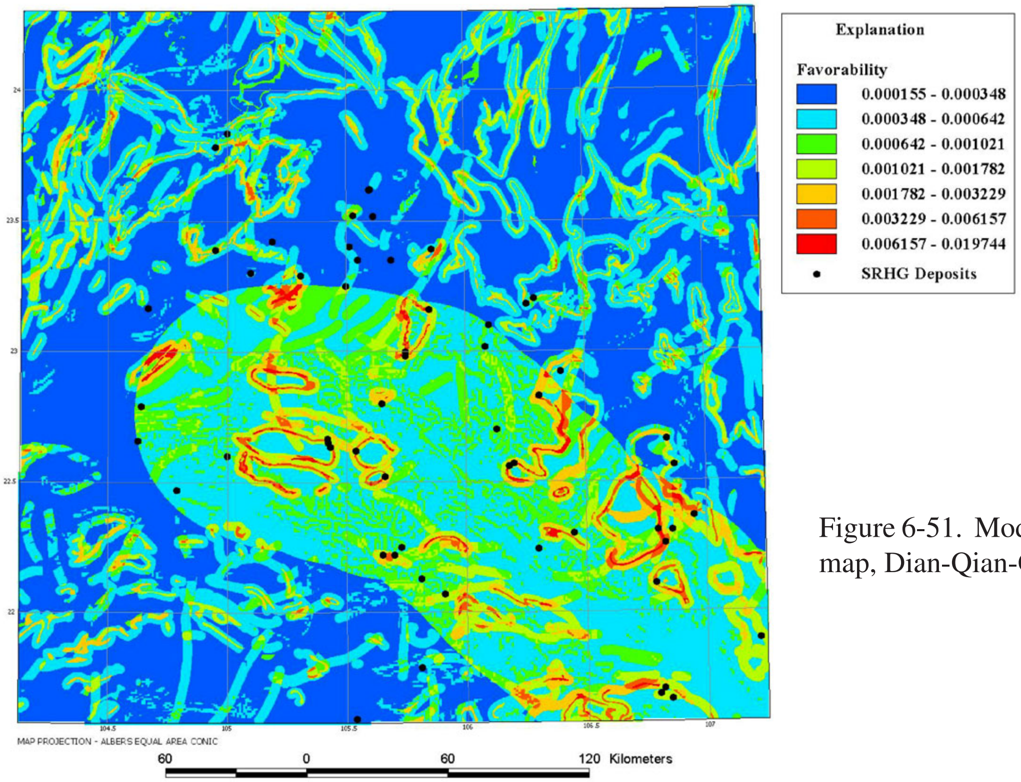

Figure 6-51. Model DA favorability map, Dian-Qian-Gui area.

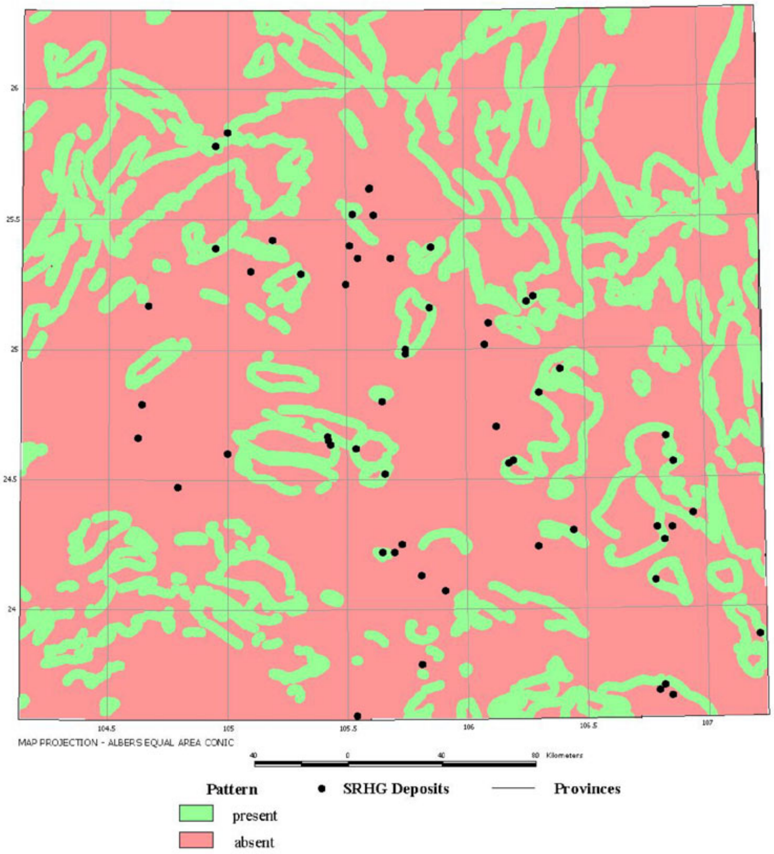

Figure 6-52: Predictor map of merged geological map units and proximity to Permian-Triassic geologic unit contacts, Dian-Qian-Gui area.

Predictor Layer	W+	W-	CONTRAST	CONFIDENCE
Geological Map Units	1.0322	-0.1754	1.2076	3.9632
Youjiang Fault System	0.6343	-0.5447	1.1791	4.4970
P-T Contact	0.5449	-0.3226	0.8675	3.3823
Anticline Traces	0.5933	-0.1144	0.7077	2.2624
Slope	0.2961	-0.1019	0.3980	1.4170
ENE-Trending Fault Traces	0.3131	-0.0840	0.3971	1.3352
10 km Lithodiversity	0.0321	-0.0785	0.1106	0.3872

TABLE 6-13. Weights of spatial association for Model DA, Dian-Qian-Gui area.

Predictor Layer	P-T Contact	Anticline Traces	ENE-Trending Fault Traces	Youjiang Fault System	Slope	Geological Map Units
10 km Lithodiversity	10.19	0.07	3.16	0.01	2.42	5.34
P-T Contact		2.82	1.99	0.00	1.34	17.41
Anticline Traces			0.90	0.06	2.56	1.22
ENE-Trending Fault Traces				2.50	0.08	2.12
Youjiang Fault System					4.24	1.54
Slope						1.19

TABLE 6-14. Chi-square values for pairwise conditional independence testing of Model DA, Dian-Qian-Gui area.

Predictor Layer	W+	W-	CONTRAST	CONFIDENCE
Youjiang Fault System	0.6343	-0.5447	1.1791	4.4970
Geological Map Units/P-T Contact	0.4755	-0.2949	0.7704	3.0038
Anticline Traces	0.5933	-0.1144	0.7077	2.2624
Slope	0.2961	-0.1019	0.3980	1.4170
ENE-Trending Fault Traces	0.3131	-0.0840	0.3971	1.3352

TABLE 6-15. Weights of spatial association for Model DB, Dian-Qian-Gui area.

Predictor Layer	Anticline Traces	ENE-Trending Fault Traces	Youjiang Fault System	Slope
Geological Map Units/P-T Contact	2.82	1.99	0.00	1.34
Anticline Traces		0.90	0.06	2.56
ENE-Trending Fault Traces			2.50	0.08
Youjiang Fault System				4.24

TABLE 6-16. Chi-square values for pairwise conditional independence testing of Model DB, Dian-Qian-Gui area.

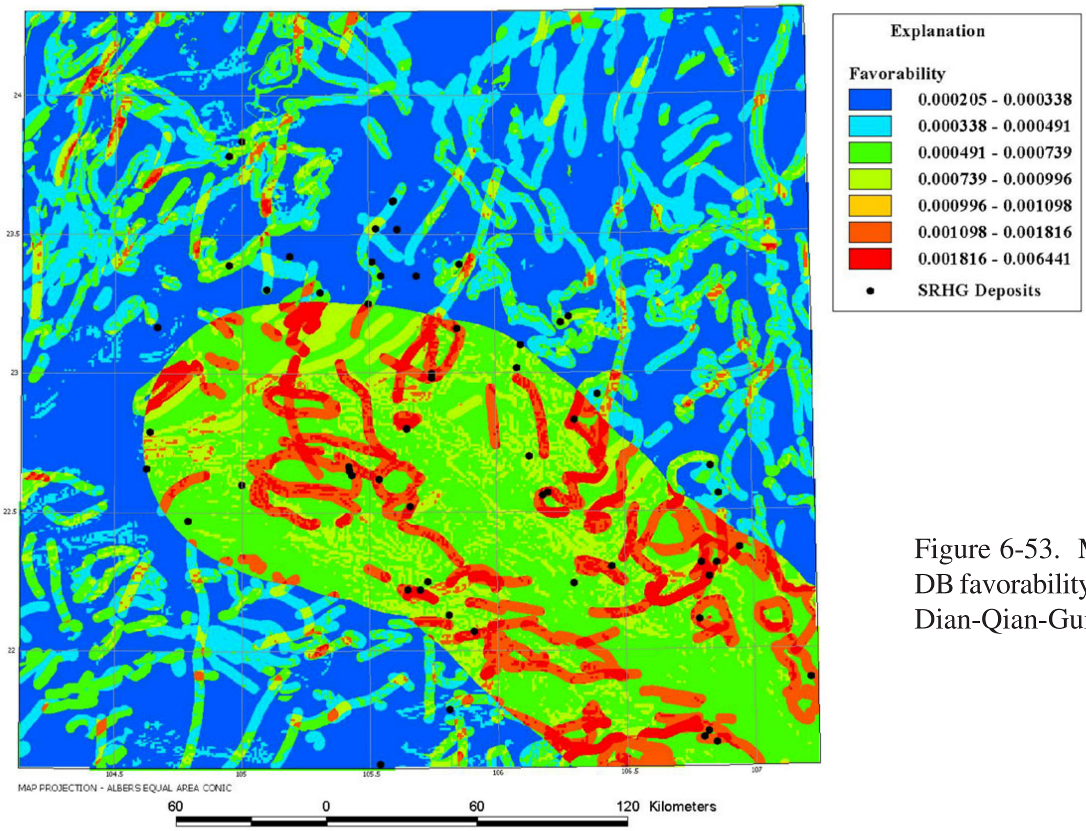

Figure 6-53. Model DB favorability map, Dian-Qian-Gui area.

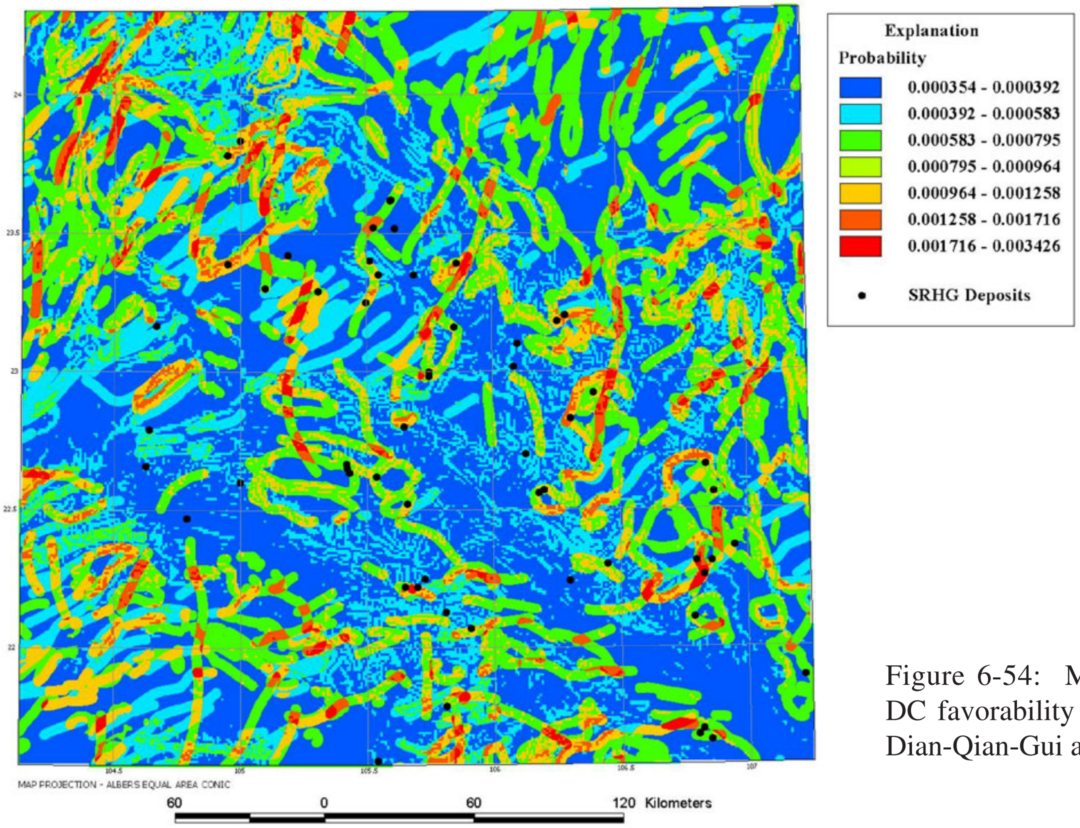

Figure 6-54: Model DC favorability map, Dian-Qian-Gui area.

Predictor Layer	W+	W-	CONTRAST	CONFIDENCE
Geological Map Units/P-T Contact	0.4755	-0.2949	0.7704	3.0038
Anticline Traces	0.5933	-0.1144	0.7077	2.2624
Slope	0.2961	-0.1019	0.3980	1.4170
ENE- Trending Fault Traces	0.3131	-0.0840	0.3971	1.3352

TABLE 6-17. Weights of spatial association for Model DC, Dian-Qian-Gui area.

Predictor Layer	Anticline Traces	ENE- Trending Fault Traces	Slope
Geological Map Units/P-T Contact	2.82	1.99	1.34
Anticline Traces		0.90	2.56
ENE- Trending Fault Traces			0.08

TABLE 6-18. Chi-square values for pairwise conditional independence testing of Model DC, Dian-Qian-Gui area.

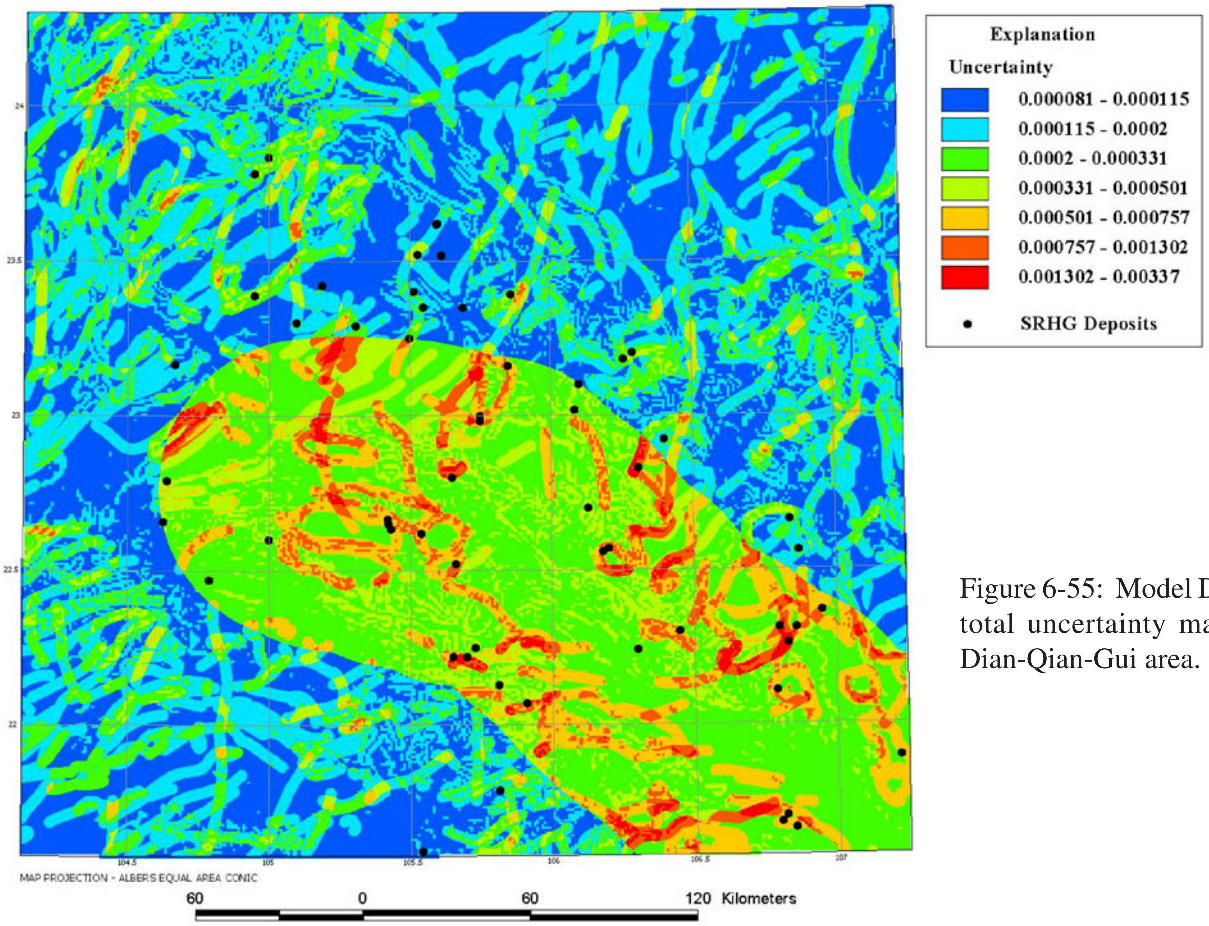

Figure 6-55: Model DB total uncertainty map, Dian-Qian-Gui area.

Analysis of Dian-Qian-Gui Study Area Models

Models DB and DC are considered most suitable for analysis and interpretation. Once again, due to the presence of conditional dependency, probabilities should be viewed as favorabilities for the same reasons as discussed previously. Maps of total uncertainty were constructed for both models (figs. 6-55 and 6-56). As expected, the patterns reflect those of the favorability maps due to the fact that the majority of error is from the variance in weight estimates.

From tables 6-15 and 6-17, it can be seen that the confidence of the predictor maps is relatively high; consequently, the favorabilities can be evaluated with relatively high degree of confidence.

Interpretation of Dian-Qian-Gui Study Area Models

Model DB predictor maps in order of influence are as follows: proximity to Youjiang fault system, lithoPT, proximity to anticlines, slope, and proximity to east-northeast-trending faults (table 6-15). Note that for the Youjiang fault system, the magnitude of W^- is just slightly less than W^+. The reason for this is that both patterns occupy a large area and encompass many training sites. To aid in interpretation of the model, areas with posterior favorabilities less than

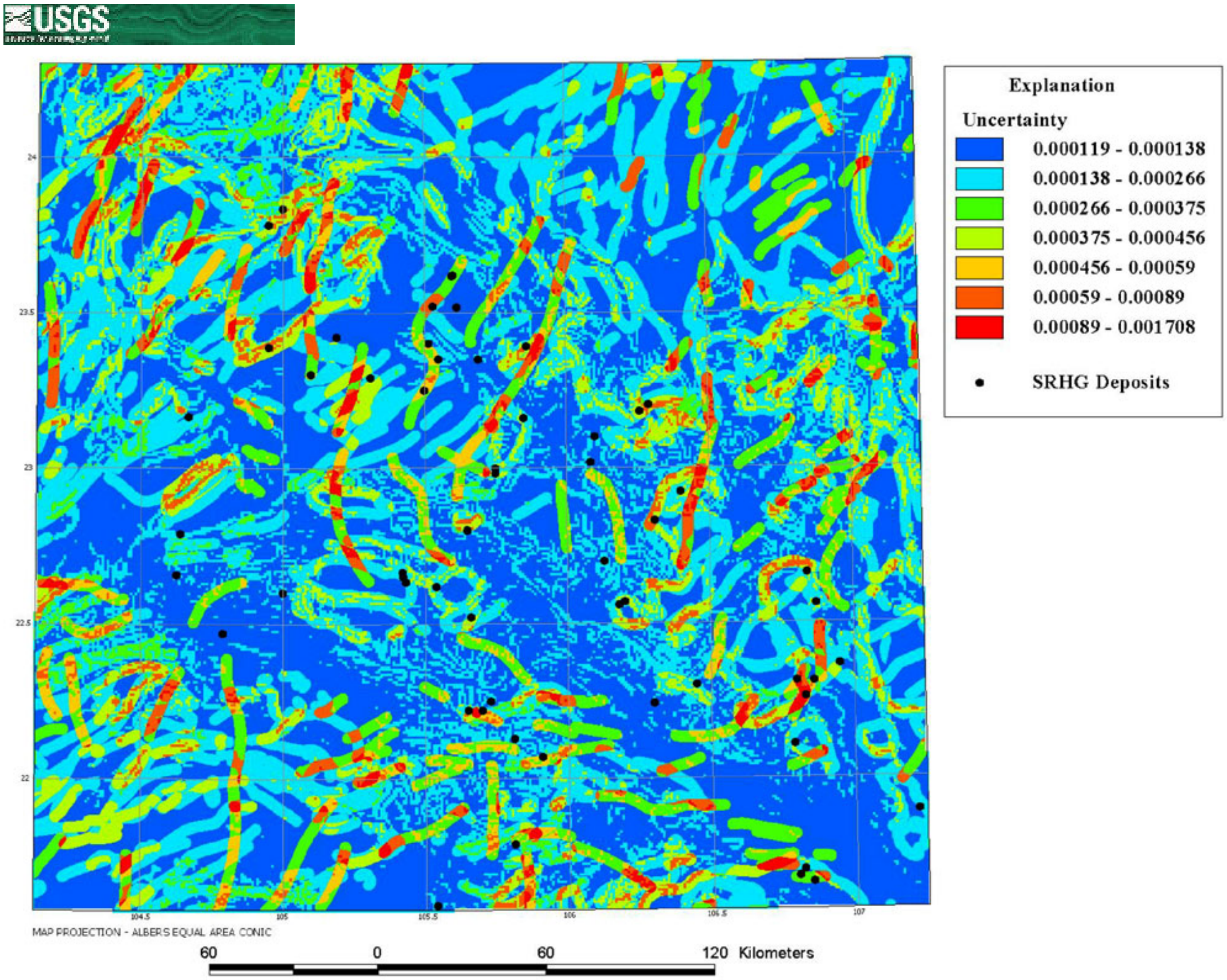

Figure 6-56: Model DC total uncertainty map, Dian-Qian-Gui area.

or equal to the prior (0.0006), have been masked out (fig. 6-57). Again, a 5 km buffer is placed around training sites with the assumption that these areas have been previously explored. The DB favorability map indicates that all areas within the 54 km Youjiang fault system distance buffer have posterior favorability values above the prior. Obvious areas of exploration would be within this area along the segments of high favorability (red). A few areas outside of the Youjiang fault system have high favorabilities as well, and should draw some attention. Examination of the DB favorability map suggests that the regional scale control over mineral sites distribution may be related to the upward movement of ore forming fluids along the Youjiang fault system where they then migrated laterally along anticlines and east-northeast-trending faults and encountered carbonate units of Permian to Triassic age in which ore bodies formed..

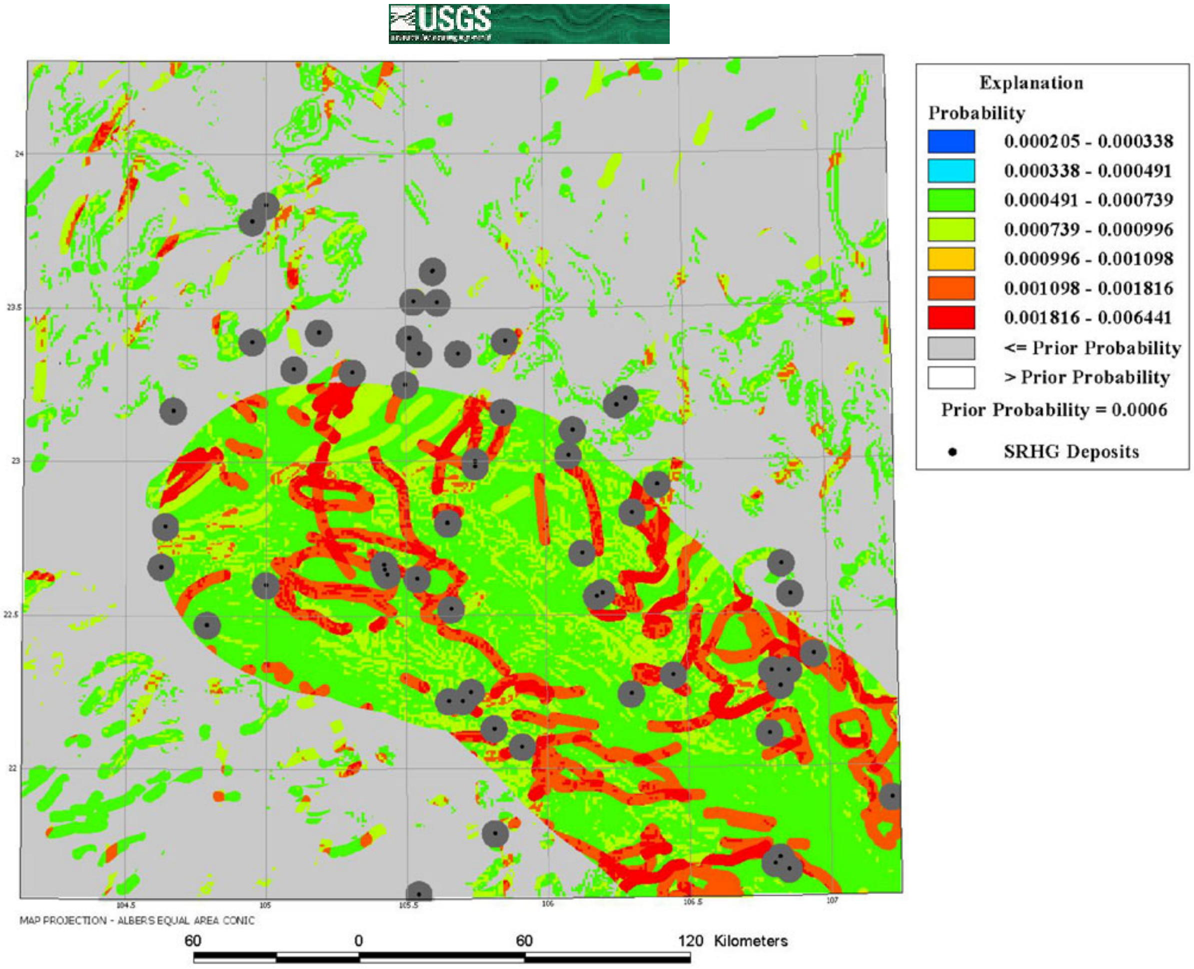

Figure 6-57: Favorability map of Model DB used for interpretation, Dian-Qian-Gui area. Note that areas with favorabilities less than or equal to the prior have been masked out (light gray). Five km buffers have been placed around all training sites (dark gray around sites.

Model DC, which excludes the Youjiang fault system proximity predictor map, is very different than that of DB favorability map. The predictor maps in order of influence are as follows: lithoPT, proximity to anticlines, slope, and proximity to east-northeast-trending faults. Figure 6-58 shows the DC favorability map after areas with posterior favorabilities less than or equal to the prior (0.0006) have been masked out, as well as 5 km buffers placed around the training sites. Visual inspection reveals that by eliminating the Youjiang fault system proximity predictor map the number and extent of exploration targets increases dramatically. Higher favorability values are more widespread throughout the area, especially along the northwestern and southwestern margins of the study area. It is also significant that in both of these regions, few known mineral sites occur. This, of course, may be proof that the Youjiang fault system is indeed a fundamental or first-order control over the distribution of SRHG mineral sites in the area.

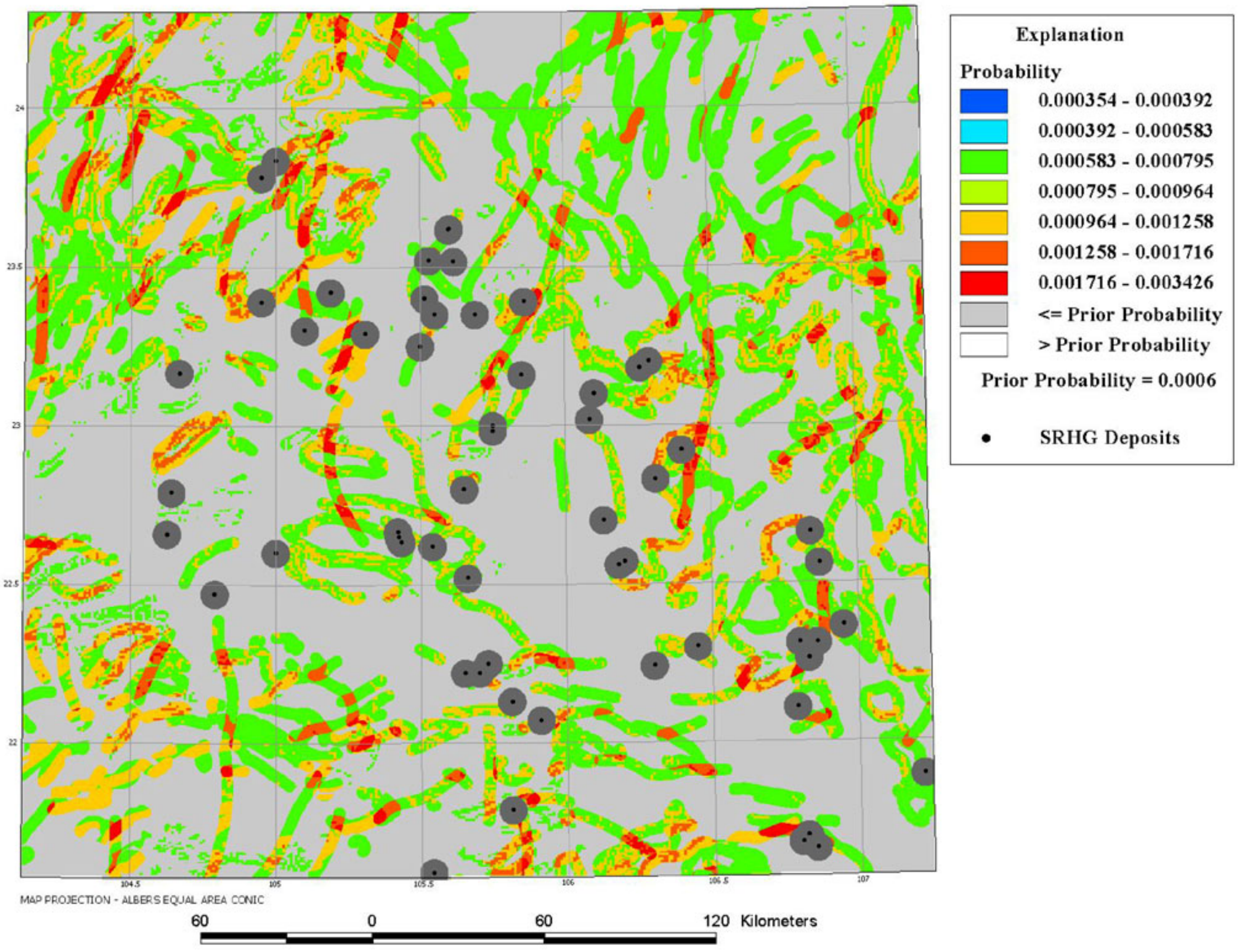

Figure 6-58. Favorability map of Model DC used for interpretation, Dian-Qian-Gui area. Note that areas with favorabilities less than or equal to the prior have been masked out (light gray). Five km buffers have been placed around all training sites (dark gray around sites).

CONCLUSIONS

Weights-of-evidence was used to model the distribution of SRHG mineral sites in two study areas, Qinling and Dian-Qian-Gui, in the People's Republic of China. Despite major differences in study area size, tectonic setting, and evidence layers, WofE modeling proved to be successful in both Qinling and Dian-Qian-Gui, providing numerous regional-scale targets for future exploration. In general, the Dian-Qian-Gui favorability maps have fewer CI problems, but the Qinling favorability maps provide better defined and focused target areas.

In the

Qinling study area, four models were built and their validity tested. All passed the chi-square test for CI, but also failed to reach the goal of >85 percent for the overall test of CI. One model, QC, was chosen as the most acceptable of these models.

From this model, three areas in particular were selected as the promising locations of exploration, while numerous other areas should also be considered.

In the Dian-Qian-Gui area, three models were built, all of which passed the overall test for CI. Models DB and DC were chosen as the most acceptable of these and both passed the tests for chi-square CI, as well as overall CI. According to Model DB, which used the Youjiang fault zone as one of the predictor maps, target areas for exploration are all within a 54 km zone surrounding the fault. The underlying metallogenic assumption which is built into this model is that the Youjiang fault system is a major control over the regional-scale distribution of the mineral sites. By not including the Youjiang fault system this assumption is removed, and as is shown in Model DC, numerous other areas throughout the region are highlighted as potential exploration targets. One model should not be considered better or worse than the other, but they should interpreted with regard to predictive evidence provided by the Youjiang fault system.

This study demonstrates that WofE modeling can be utilized to highlight regional-scale targets where more detailed exploration may be warranted, as well as provide for regional-scale interpretations of mineralization controls. Furthermore, this study has demonstrated that WofE modeling can be successfully carried out using evidence layers derived largely, and in some cases exclusively, from geological map data.

ACKNOWLEDGEMENTS

This chapter resulted from graduate studies by the senior author at the Mackay School of Mines, University of Nevada-Reno in collaboration with the U.S. Geological Survey, Reno Field Office. Jim Carr provided guidance as thesis advisor. Huang Jiazhan was helpful in providing accurate locations of the training sites. The manuscript benefited from a review by Stephen Ludington.

REFERENCES

Agterberg, F. P., 1989a, LOGDIA—FORTRAN 77 program for logistic regression with diagnostics: Computers and Geosciences, v. 15, p. 599–614.

———1989b, Systematic approach to dealing with uncertainty of geoscience information in mineral exploration, *in* Weiss, A., ed., Proceedings of the 21st Symposium on "Application of Computers and Operations Research in the Mineral Industry", Society of Mining engineers, Inc., Littleton, Colorado, 1989, p. 165–178.

Agterberg, F.P., Bonham-Carter, G.F., Wright, D.F., 1990, Statistical pattern integration for mineral exploration, *in* Gaal, G., and Merriam, D.F., eds., Computer Applications in Resource Estimation Prediction and Assessment of Metals and Petroleum: Pergamon Press, Oxford-New York, 19 p.

Agterberg, F. P., Bonham-Carter, G. F., Cheng, Q., and Wright, D. F., 1993, Weights of evidence modeling and weighted logistic regression for mineral potential mapping, *in* Davis, J. C., and Herzfeld, U. C., eds., Computers in Geology, 25 Years of Progress: Oxford University Press, Oxford, England, p. 13–32.

Arehart, G.B., 1996, Characteristics and origin of sedimentary rock-hosted Au deposits: a review: Ore Geology Reviews, v.11, p. 383–403.

Barto, K.P., 2000, Model GTOPO30 Data in ArcView GIS: ArcUser, p. 48–51.

Bonham-Carter, G.F., 1994, Geographic Information Systems for Geoscientists: Modelling with GIS (Computer Methods in the Geosciences Volume 13): Pergamon Press/Elsevier Science Publications, Tarrytown, New York, 398 p.

Bonham-Carter, G.F., Agterberg, F.P., and Wright, D.F., 1988, Integration of geological datasets for Au exploration in Nova Scotia: Photogrammetric Engineering and Remote Sensing (PE&RS), v. 54, p. 1,585–1,592.

———1989, Weights of evidence modeling: A new approach to mapping mineral potential, *in*, Agterberg, F.P., and Bonham-Carter, G.F., eds., Statistical Applications in the Earth Science: Geological Survey of Canada, Paper 89-9, p. 171–183.

Cheng, Yuqi, ed., 1990, Geological Map of China: Geological Publishing House, Beijing, scale 1:5,000,000, 2 sheets.

Cox, D.P., Barton, P.B., and Singer, D.E., 1986, Introduction, in Cox, D.P., and Singer, D.A., eds., Mineral Deposit Models: U. S. Geological Survey Bulletin 1693, p. 1–6.

Kemp, L.D., Bonham-Carter, G.F., Raines, G.L. and Looney, C.G., 2001, Arc-SDM: Arcview extension for spatial data modelling using weights of evidence, logistic regression, fuzzy logic and neural network analysis, http://ntserv.gis.nrcan.gc.ca/sdm/.

Li, Zhiping, and Peters, Stephen G., 1998, Comparative Geology and Geochemistry of Sedimentary Rock-Hosted (Carlin-Type) Gold Deposits in the People's Republic of China and in Nevada, USA: U.S. Geological Survey Open-File Report 98-466, p.1–86. [http://geopubs.wr.usgs.gov/open-file/of98-466/]. V. 1.2 updated May, 2000, March, 2001.

Lu, Huanzhang, 1988, Fluid inclusion studies on different types of Chinese gold deposits: Gold 88, Abstracts Geological Society of Australia. No. 23, (1-2), p. 442–444.

Mendenhall, W., and Reinmuth, J. E., 1974, Statistics for management and–economics, 2nd Ed.: Duxbury Press, North Scituate, Massachusetts, 596 p.

Mihalasky, M.J., 1999, Mineral Potential Modelling of Gold and Silver Mineralization in the Nevada Great Basin, A GIS-based Analysis Using *Weights of Evidence*: Ph.D. Thesis, University of Ottawa, 361 p.

Mihalasky, M. J., and Bonham Carter, G. F., 1999, The spatial relationship between mineral deposits and lithologic diversity in the Nevada Great Basin, *in* Lippard, S.J., Naess, A., and Sinding Larsen, R., eds., Proceedings of IAMG'99, Trondheim, Norway, 6–11 August 1999, pp. 369–374.

Mihalasky, M. J., and Bonham Carter, G. F., 2001 (in press), Lithodiversity and its spatial association with metallic mineral sites, Nevada Great Basin: Natural Resources Research.

Mihalasky, M. J., and Raines, G. L., 2001 (in internal revision), A reconnaissance method for regional-scale mineral-resource assessment, based exclusively on geologic-map data: Natural Resources Research.

Raines, G. L., 1999, Evaluation of weights of evidence to predict epithermal-gold deposits in the Great Basin of the western United States: Natural Resources Research, v. 8, p. 257–276.

Seedorf, E., 1991, Magmatism, extension, and ore deposits of Eocene to Holocene age in the Great Basin – mutual effects and preliminary proposed genetic relationships, *in* Raines, G.L., Lisle, R.E., Schafer, R.W., and Wilkinson, W.H., eds., Geology and ore deposits of the Great Basin, Symposium Proceedings: Reno, Nevada, Geological Society of Nevada, p. 133–178.

Speigelhalter, D.J., and Knill-Jones, R.P., 1984, Statistical and knowledge-based approaches to clinical decision-support systems, with an application in gastroenterology: Journal of the Royal Statistical Society, A, Part 1, p. 35–77.

Wang, Xichuan, ed., 1990, Geological Map of China, Explanatory Notes: Geological Publishing House, Beijing, 82 p.

Wang, Xiao-Chun, and Zhang, Zhe-Ru, 1999, Geology of Sediment-Hosted Disseminated Gold Deposits in Northern Sichuan, China: Manuscript for Economic Geology, 37p.

Wright, D. F., Bonham-Carter, G. F., 1996, VHMS favorability mapping with GIS-based integration models, Chisel Lake-Anderson Lake area, *in* Bonham-Carter, G. F., Galley, A. G., and Hall, G. E. M., editors, EXTECH I: A Multidisciplinary Approach to Massive Sulphide Research in the Rusty Lake-Snow Lake Greenstone Belts, Manitoba: Geological Survey of Canada, Bulletin 426, p. 339–376, 387–401.

Zhou, J., Flood, P.G., Li, W., 2000, Gold Grade and Tonnage Models of the Gold Deposits, China: Resource Geology, v. 50, no. 1, p. 53–64.